

Rochester Institute of Technology

RIT Digital Institutional Repository

Theses

5-22-2006

Low temperature dopant activation for applications in thin film silicon devices

Eric Woodard

Follow this and additional works at: <https://repository.rit.edu/theses>

Recommended Citation

Woodard, Eric, "Low temperature dopant activation for applications in thin film silicon devices" (2006). Thesis. Rochester Institute of Technology. Accessed from

This Thesis is brought to you for free and open access by the RIT Libraries. For more information, please contact repository@rit.edu.

Low Temperature Dopant Activation for Applications in Thin Film Silicon Devices

By

Eric M. Woodard

A Thesis Submitted

In Partial Fulfillment

of the Requirements for the Degree of

Master of Science

in

Material Science and Engineering

Approved by:

Prof. _____
Dr. Karl D. Hirschman (Thesis Advisor)

Prof. _____
Dr. Santosh Kurinec (Committee)

Prof. _____
Dr. Surendra K. Gupta (Committee)

Prof. _____
Dr. Robert Pearson (Committee)

Prof. _____
Dr. Kalathur Santhanam (Department Head)

DEPARTMENT OF MATERIAL SCIENCE AND ENGINEERING

COLLEGE OF SCIENCE

ROCHESTER INSTITUTE OF TECHNOLOGY

ROCHESTER, NEW YORK

MAY 2006

Low Temperature Dopant Activation for Applications in Thin Film Silicon Devices

By

Eric M. Woodard

I, Eric M. Woodard, hereby grant permission to the Wallace Memorial Library of the Rochester Institute of Technology to reproduce this document in whole or in part that any reproduction will not be for commercial use or profit.

Eric M. Woodard

May 19, 2006

Acknowledgments

There are many people I would like to acknowledge for their contribution to this work and to my education.

First, my thesis advisor **Dr. Karl Hirschman** and my committee, **Dr. Santosh Kurinec**, **Dr. Surendra Gupta**, and **Dr. Robert Pearson**; you have all assisted me with this thesis in various ways and it could not have been done without any of you.

To the people at **Corning Inc.** especially **Dave Dawson-Elli** and **Greg J. Couillard** for supporting this project and providing some valuable assisting in SIMS and TEM metrology.

I would like to thank **Implant Sciences** and **Chuck Hudak** for providing implant services and fast processing time that allowed further exploration than I originally planned.

Roger Brennen at **Solecon Laboratories** for the spreading resistance profiling and discussions on the unusual results.

Bruker AXS for providing x-ray diffraction analysis.

To the folks at the Semiconductor Manufacturing Fabrication Laboratories here at RIT; **Rich Battaglia**, **Scott Blondell**, **Tom Grimsley**, **John Nash**, **Sean O'Brien**, **Bruce Tolleson**, and **Dave Yackoff** a special thanks for all the support and assistance during this work.

And finally, to all my fellow graduate students; **Mike Aquilino**, **Germain Fenger**, **Vee Chee Hwang**, **Dan Jaeger**, **Robert Manley**, **Bob Mulfinger**, **Dave Pawlik**, and **Reinaldo Vega** this work could not have been completed without you.

Abstract

One of the major areas of research for integrated electronic systems is the development of systems on glass or plastic to optimize the performance/cost tradeoff. These new substrate materials impose stringent constraints on electronic device fabrication, including limitations on chemical and thermal processes. Processes that do not use temperatures greater than 900°C have the increased flexibility for application involving new substrate materials.

Silicon is a semiconductor material that can have very different conductive properties based on the levels of impurities. A conventional method of adding impurities is ion implantation. When a substrate is implanted, the ions will break up the ordered crystal lattice and induce damage in the substrate. Interstitial impurities cannot contribute to conductivity; therefore thermal activation is critical for device operation. Annealing is a thermal process that serves two purposes; to re-crystallize the substrate, and to electrically activate the dopant ions.

The mechanism of dopant activation in silicon under low-temperature (600°C) annealing conditions is re-crystallization. By exploring rapid thermal annealing (RTA) and furnace processing, a physical model of activation is presented for three dopant ions (boron, phosphorus, and arsenic) over a wide dose range. Sheet resistance and spreading resistance profiling (SRP) have been used to characterize the electrical activation of dopants. Secondary ion mass spectroscopy (SIMS) and x-ray diffraction analysis have been used to determine the distribution of the implanted impurities. Results indicate that eighty to ninety percent of the dopant can be activated at the reduced temperature of 600°C; dependent on the dose implanted.

Table of Contents

| | |
|--|------|
| Title Page | i |
| Library Release | ii |
| Acknowledgments | iii |
| Abstract | iv |
| Table of Contents | v |
| List of Figures | viii |
| List of Tables | xi |
| List of Abbreviations | xii |
| CHAPTER 1 INTRODUCTION | 1 |
| 1.1 THIN FILM TRANSISTOR FABRICATION | 1 |
| 1.2 PROCESS CONSTRAINTS AND CHALLENGES | 3 |
| 1.3 METHODS OF MEASURING ACTIVATION | 4 |
| 1.4 OUTLINE OF THESIS | 6 |
| CHAPTER 2 ELECTRICAL ACTIVATION | 8 |
| 2.1 DOPANT ATOM ACTIVATION | 8 |
| 2.2 LATTICE DEFECTS | 11 |
| 2.3 DIFFUSION | 15 |
| 2.4 CARRIER MOBILITY | 18 |
| 2.5 AMORPHIZATION AND RE-CRYSTALLIZATION | 20 |
| CHAPTER 3 ION IMPLANTATION | 23 |
| 3.1 ION IMPLANTER TECHNOLOGY | 23 |
| 3.2 IMPLANTATION PROFILE | 25 |
| 3.3 ION-INDUCED LATTICE DAMAGE | 28 |
| 3.4 PRE-AMORPHIZATION | 30 |

| | | |
|-------------------------------------|--|----|
| 3.5 | IMPLANT AND ACTIVATION MODELING | 32 |
| CHAPTER 4 ANALYSIS TECHNIQUES | | 39 |
| 4.1 | FOUR POINT PROBE..... | 39 |
| 4.2 | SPREADING RESISTANCE PROFILING | 41 |
| 4.3 | HALL EFFECT | 43 |
| 4.4 | CAPACITANCE ANALYSIS..... | 45 |
| 4.5 | X-RAY DIFFRACTION | 46 |
| 4.6 | TRANSMISSION ELECTRON MICROSCOPY..... | 48 |
| 4.7 | SECONDARY ION MASS SPECTROSCOPY..... | 48 |
| CHAPTER 5 DONOR ACTIVATION..... | | 50 |
| 5.1 | PHOSPHORUS ACTIVATION..... | 50 |
| 5.2 | ANNEALING PHOSPHORUS | 52 |
| 5.3 | X-RAY DIFFRACTION ANALYSIS | 55 |
| 5.4 | PHOSPHORUS PROFILING..... | 56 |
| 5.5 | ARSENIC ACTIVATION..... | 59 |
| 5.6 | PRE-AMORPHIZATION OF PHOSPHORUS..... | 62 |
| 5.7 | SUMMARY OF PHOSPHORUS AND ARSENIC | 65 |
| CHAPTER 6 ACCEPTOR ACTIVATION | | 67 |
| 6.1 | BORON ACTIVATION | 67 |
| 6.2 | PRE-AMORPHIZATION..... | 68 |
| 6.3 | X-RAY DIFFRACTION ANALYSIS | 71 |
| 6.4 | ADDITIONAL STUDY ON FLUORINE AND BORON | 72 |
| 6.5 | TEM ANALYSIS | 86 |
| 6.6 | LOW DOSE BORON ACTIVATION | 87 |
| 6.7 | FLUORINE AND ARGON PROFILING | 89 |
| 6.8 | SUMMARY OF ACCEPTOR EXPERIMENTS..... | 92 |

| | |
|---|-----|
| CHAPTER 7 CONCLUSION | 93 |
| REFERENCES..... | 97 |
| APPENDIX A FABRICATION PROCESSES..... | A-1 |
| A.1 FURNACE ANNEALING | A-1 |
| A.2 RAPID THERMAL ANNEALING | A-2 |
| A.3 TEOS DEPOSITION..... | A-6 |
| APPENDIX B TABLE OF EXPERIMENTS | B-1 |
| APPENDIX C SHEET RESISTANCE DATA..... | C-1 |
| APPENDIX D SPREADING RESISTANCE DATA..... | D-1 |
| APPENDIX E MODEL EQUATIONS..... | E-1 |

List of Figures

| | |
|---|----|
| Fig. 1.1 – Thin film, amorphous silicon transistor with bottom gate design. | 1 |
| Fig. 2.1 – Atom substitution as an activation mechanism. | 9 |
| Fig. 2.2 – Low Temperature activation effects, for non-amorphized silicon [2]. P_{Hall} refers to the measured Hall dose; refer to section 4.3 for more details. | 10 |
| Fig. 2.3 – The diamond lattice, picture courtesy of [6]. | 12 |
| Fig. 2.4 – Arrhenius Relationship for vacancy concentration versus temperature. | 14 |
| Fig. 2.5 – Diffusivity for boron and phosphorus as a function of $1000/T$ [9]. The worst- case senario for the enhancement due to TED gives increase of five magnitudes in diffusivity at 600°C , equivalent to 875°C under equilibrium conditions. | 15 |
| Fig. 2.6 – Boron implants annealed at 600°C | 17 |
| Fig. 2.7 – Mobility as a function of carrier concentration and dopant type, generated from experimental measurements, from [11]. | 19 |
| Fig. 2.8 – Literature dopant activation for phosphorus, showing the self-amorphization effect on activation [5]. Sub Amorphous refers to the implanted dose that is not sufficient to create an amorphous region in the silicon. | 21 |
| Fig. 3.1 – The boron trifluoride implant mass spectrum. Spectrum done on a Varian 350D Ion Implanter. | 24 |
| Fig. 3.2 – Ion energy loss as separated by components, from [2]. | 27 |
| Fig. 3.3 – Degree of implant damage as a function of ion mass and dose. (a) individual amorphous regions created by a low implant dose. (b) Variation between light and heavy ions. (c) A high dose continuous amorphous layer. | 28 |
| Fig. 3.4 – SRIM simulation of phosphorus implant into silicon showing, (lower curve) the ion penetration, (upper curve) the damage events, and the self-amorphized region. The region between the continuous amorphous region and the primary crystal damaged region represents the uncertainty in this boundary. Damage events are a summation of ion displacements and vacancies. The implant simulated was for a $4 \times 10^{15} \text{cm}^{-2}$ phosphorus implant. | 31 |
| Fig. 3.5 – SRIM simulation of ion displacement for phosphorus (92 keV), normalized damage events for implant doses of 5×10^{13} to $8 \times 10^{15} \text{cm}^{-2}$. Damage normalized to $5 \times 10^{22} \text{cm}^{-3}$ silicon atoms. | 34 |
| Fig. 3.6 – SRIM simulation for boron (34 keV) normalized damage events for implant doses of 1×10^{14} to $8 \times 10^{15} \text{cm}^{-2}$. Damage normalized to $5 \times 10^{22} \text{cm}^{-3}$ silicon atoms. . | 35 |
| Fig. 3.7 – Normalized Fluorine Damage events for a 75 keV implant. | 36 |
| Fig. 3.8 – Argon normalized damage density for an energy of 170 keV. | 37 |
| Fig. 3.9 – Activation profile possibilities, where the dotted line represents the implanted profile. | 38 |
| Fig. 4.1 – A sample sheet resistance map taken from a CDE Resmap system. | 40 |
| Fig. 4.2 – SRP measurement setup, from [16]. | 41 |
| Fig. 4.3 – The Hall Effect. | 44 |
| Fig. 4.4 – MOS capacitor under bias. | 46 |

| | |
|---|----|
| Fig. 4.5 – X-ray diffraction pattern for a silicon wafer. Only a single peak should be present due to the crystalline nature of the sample. The labeled peaks refer to the different wavelengths in the copper x-ray source. | 47 |
| Fig. 4.6 – Sample SIMS scan for a boron implant. Notice that below $1 \times 10^{16} \text{cm}^{-3}$ concentration, the noise in the signal begins to increase. | 48 |
| Fig. 5.1 – Percentage of phosphorus activation for a range of implanted doses. The x-axis is the amount of dose that is within the silicon. This axis is not scaled. | 50 |
| Fig. 5.2 – Phosphorus annealing experiment. Two anneal times per anneal type and 3 temperatures: 550, 600, and 650°C. | 52 |
| Fig. 5.3– The effect of a second furnace anneal on rapid thermal samples. The phosphorus dose is $4 \times 10^{15} \text{cm}^{-2}$ | 53 |
| Fig. 5.4– Phosphorus activation for different anneal conditions: 1 hour furnace annealing, 2 minute RTA followed by a 1 hour furnace anneal. | 54 |
| Fig. 5.5 – XRD for 1×10^{14} and $4 \times 10^{15} \text{cm}^{-2}$ implanted phosphorus doses annealed for one hour at 600°C. A phosphorus implant of $5 \times 10^{14} \text{cm}^{-2}$ was done without an anneal. | 55 |
| Fig. 5.6 – SRP for phosphorus implant doses of 1×10^{14} , 1×10^{15} , and $4 \times 10^{15} \text{cm}^{-2}$ superimposed with SUPREM implant models (dotted lines). | 57 |
| Fig. 5.7 – SIMS and spreading resistance profiles for $1 \times 10^{14} \text{cm}^{-2}$ phosphorus implant, annealed at 600°C for 1 hour. SUPREM model included for reference. | 58 |
| Fig. 5.8 – SIMS, model and spreading resistance profiles for $4 \times 10^{15} \text{cm}^{-2}$ phosphorus implant, annealed at 600°C for 1 hour. | 59 |
| Fig. 5.9 – Arsenic percent activation as compared with relevant phosphorus data. | 60 |
| Fig. 5.10 – Arsenic active dose compared with phosphorus active dose for both furnace and RTA. | 61 |
| Fig. 5.11– Pre-amorphization implant for phosphorus, all samples furnace annealed for one hour. | 62 |
| Fig. 5.12 – SRP of $1 \times 10^{14} \text{cm}^{-2}$ phosphorus with and without a silicon pre-amorphization. | 62 |
| Fig. 5.13 – TEM micrograph of a phosphorus implant pre-amorphized by a silicon implant. Sample was annealed at 600°C for one hour. | 64 |
| Fig. 5.14 – Phosphorus SIMS and SRP with and without a silicon pre-amorphization. .. | 65 |
| Fig. 6.1 – Boron percent activation for furnace annealing at 600°C for one hour. | 67 |
| Fig. 6.2 – Pre-amorphization with silicon, argon, and fluorine for five boron doses. Samples were annealed at 600°C for one hour. | 68 |
| Fig. 6.3 – Fluorine pre-amorphization experiment for a constant boron dose of $4 \times 10^{15} \text{cm}^{-2}$. Samples were annealed at 600°C for one hour. | 69 |
| Fig. 6.4 – Percentage of Boron activation with varying argon doses. The boron dose tested was $1 \times 10^{15} \text{cm}^{-2}$. The samples were annealed at 600°C for one hour. | 70 |
| Fig. 6.5 – XRD scans for fluorine and boron with fluorine implants. The boron sample was annealed at 600°C for one hour. | 72 |
| Fig. 6.6 – Boron active dose compared with active dose for BF_2 and fluorine pre-amorphization at both anneal conditions. The fluorine was implanted at 75 keV and a dose of $3 \times 10^{15} \text{cm}^{-2}$ was used to provide adequate amorphization. The anneal was done at 600°C for one hour. | 73 |
| Fig. 6.7 – Anneal experiment for fluorine amorphized boron. | 74 |

| | |
|---|-----|
| Fig. 6.8 – Active dose versus anneal time for fluorine pre-amorphized boron implants. The horizontal lines indicate 100% activation levels for each implant dose. | 76 |
| Fig. 6.9 – Adjusted Boron and Fluorine SIMS profiles before and after an anneal. | 77 |
| Fig. 6.10 – Boron SIMS profiles for $1 \times 10^{14} \text{ cm}^{-2}$, $1 \times 10^{15} \text{ cm}^{-2}$, and $4 \times 10^{15} \text{ cm}^{-2}$ doses. The $1 \times 10^{15} \text{ cm}^{-2}$ dose includes all three methods of pre-amorphization, fluorine, argon and silicon. All anneals were done at 600°C for 1 hour. | 79 |
| Fig. 6.11 – Boron SRP for 1×10^{14} , 1×10^{15} , and $4 \times 10^{15} \text{ cm}^{-2}$ doses, overlaid with SUPREM SRP models. | 81 |
| Fig. 6.12 – Boron SRP for three anneal times. The boron dose is $1 \times 10^{14} \text{ cm}^{-2}$ and annealed at 600°C | 82 |
| Fig. 6.13 – SRP and SIMS profiles for $1 \times 10^{15} \text{ cm}^{-2}$ boron with fluorine, argon and silicon pre-amorphization implants. | 83 |
| Fig. 6.14 – SRP, SIMS, and model profiles for $4 \times 10^{15} \text{ cm}^{-2}$ boron with fluorine implants. | 85 |
| Fig. 6.15 – $1 \times 10^{14} \text{ cm}^{-2}$ boron implant – SRP and SIMS comparing silicon and fluorine pre-amorphizations profiles. | 86 |
| Fig. 6.16 – TEM of Boron implant with a fluorine implant used for a pre-amorphization. Anneal was done at 600°C for one hour. | 87 |
| Fig. 6.17 – Capacitor-voltage measurements with and without a boron implant. | 88 |
| Fig. 6.18 – Fluorine and Argon SIMS profiles for no boron implant, and for boron doses of 1×10^{14} , 1×10^{15} , and $4 \times 10^{15} \text{ cm}^{-2}$. All samples annealed at 600°C for 1 hour. | 90 |
| Fig. 6.19 – Experimental data from [24] showing SIMS measurements of boron and fluorine after a 950°C , 30 second anneal. | 91 |
| Fig. A.1 – Wafer annealed for 3 minutes at 600°C . Points indicate where SRP was done. | A-3 |
| Fig. A.2 – Wafer annealed at 600°C for 5.5 minutes. Implant is $5 \times 10^{13} \text{ cm}^{-2}$ of boron. | A-4 |
| Fig. A.3 – Wafer Annealed at 600°C for 3 minutes. Implant is boron at $5 \times 10^{14} \text{ cm}^{-2}$ dose. | A-5 |
| Fig. A.4 – SRP from two points on an incomplete anneal. The sample was implanted with $1 \times 10^{15} \text{ cm}^{-2}$ boron and annealed for three minutes. | A-6 |

List of Tables

| | |
|--|-----|
| Table 2-1 Atomic Radii and Volumes | 11 |
| Table 6-1 SRP and SIMS integrations and 4-pt. probe Results..... | 80 |
| Table A-1 Furnace recipe details | A-1 |
| Table A-2 RTA recipe calibration parameters..... | A-3 |
| Table B-1 Phosphorus Experiments..... | B-1 |
| Table B-2 Arsenic Experiments..... | B-2 |
| Table B-3 Boron Experiments | B-2 |
| Table C-1 P-type wafers | C-1 |
| Table C-2 N-type wafers..... | C-2 |
| Table E-1 Fitting parameters for mobility equations [11] | E-1 |

List of Abbreviations

| | |
|-------|---|
| 4PP | Four-Point Probe |
| CMOS | Complementary Metal-Oxide Semiconductor |
| CVD | Chemical-Vapor Deposition |
| FWHM | Full-Width Half-Max |
| IC | Integrated Circuit |
| IR | Infrared |
| MOS | Metal-Oxide Semiconductor |
| PECVD | Plasma-Enhanced Chemical Vapor Deposition |
| RTA | Rapid Thermal Annealing |
| RTP | Rapid Thermal Processing |
| S/D | Source and Drain |
| SIMS | Secondary Ion Mass Spectrometry |
| SPE | Solid-Phase Epitaxy |
| SRIM | Stopping Range of Ions in Matter |
| SRP | Spreading Resistance Profiling |
| TED | Transient-Enhanced Diffusion |
| TEM | Transmission Electron Microscopy |
| TFT | Thin Film Transistor |
| XRD | X-Ray Diffraction |

Chapter 1

Introduction

1.1 THIN FILM TRANSISTOR FABRICATION

Thin film transistors (TFTs) are a specialized branch of integrated circuit (IC) that fabricates transistors in a thin layer of silicon supported by a glass substrate. The purpose of these devices is to integrate and control electronics without an external chip. There are several variations of this technology, depending on the morphology of the silicon layer. Amorphous silicon is the first type used for this application. The silicon can be deposited on the glass substrate at temperatures below 400°C, which makes it ideal, since the melting point of the glass is approximately 600°C. More recently, poly-crystalline [1] and single-crystalline silicon [1] have been explored as an alternative to amorphous silicon.

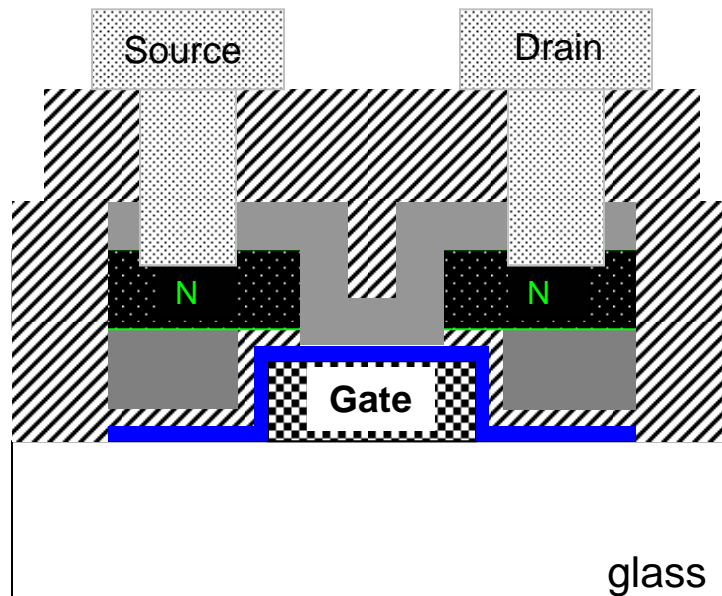


Fig. 1.1 – Thin film, amorphous silicon transistor with bottom gate design.

The advantage is an increase in the device speed; the more order within the silicon lattice, the faster carriers can move through the device. Depositing poly-crystalline silicon, or Polysilicon (poly-Si), can be done by direct deposition through chemical-vapor-deposition (CVD), or by depositing amorphous silicon and annealing the silicon to create crystals grains [1]. Polysilicon can have higher carrier mobility, depending on the grain size and orientation. The orientation of the crystal grains is difficult to control, which means a great deal of process characterization is required to direct the grain formation. Single-crystalline silicon has the most desirable characteristics for transistors, and much the same processing technology can be used. The difficulty with using single-crystal silicon is that it can not be directly deposited on the glass, an indirect method is required. In all cases of silicon morphology, temperature constraints must be imposed, due to the glass substrate.

Doping is used to modify conductance of silicon. The introduction of these impurities changes the conductance through the process of electrical activation. Activation of dopant ions requires energy, which is usually provided by heat. Typical CMOS processing uses many process steps above 1000°C; more than enough energy to activate most dopant atoms. The challenge to dopant activation comes into play when thermal constraints are imposed. By reducing the allowed temperature to 600°C, dopant activation becomes an important consideration. With amorphous or poly-silicon, dopant activation is not an issue, since the dopant can be introduced in a gaseous phase when the material is deposited. This process is known as in-situ doping. However, this method cannot provide low doping concentrations. It is only when the switch is made from polysilicon to single-crystalline silicon that dopant activation becomes an important

consideration. This is because the dopants must be introduced separately, since even basic transistor processes can use several doped regions at various concentrations. If less ions become electrically active than anticipated, then the device will not work as intended. The research presented here outlines a method to activate dopants, at reasonable levels, within the thermal constraints. Without the additional thermal energy, 100% activation may not be possible; however there are several techniques that can be employed to achieve acceptable levels of activation. So long as the levels of activation are acceptable and predictable, a process can be designed to fabricate transistors. When characterizing the activation, it is important to consider both the doping concentration, and how this changes with depth.

1.2 PROCESS CONSTRAINTS AND CHALLENGES

There are a variety of techniques available to introduce dopants into silicon, such as ion implantation [2], spin-on dopant [2], gas-immersion [2], and proximity doping [2]. Spin-on dopant and proximity doping both rely on high temperature diffusion to dope the silicon. Due to the thermal constraints, these methods cannot be used. Gas-immersion uses a high powered laser to melt the surface of the silicon, while the dopant comes from a gaseous source. This method has a limited use, since once again it uses a gaseous source for the dopants and controlling the concentration that enters the silicon can be difficult. Ion implantation uses a high energy, focused ion beam and due to their acceleration, the ions can penetrate the silicon layer. Implantation is the preferred method due to its accuracy and ability to dope small concentrations, and is the method of doping used in this investigation.

Only introducing dopants into the silicon is not sufficient; in order to change the silicon conductivity, the dopants must be activated, through a thermal anneal process. With constraints on high temperature processing limited to 600°C, the electrical activation becomes challenging. In order to anneal silicon, two main techniques are used, furnace annealing and rapid thermal annealing. Furnace annealing is the standard process used when diffusion is required, since it takes a relatively long time to perform. Rapid thermal annealing, as the name suggests, operates on a much faster time scale. The time regimes for these two processes are on different scales, rapid thermal being on the order of seconds, while furnace is on the order of minutes and hours. The method used to anneal the samples is an independent factor from the anneal time due to the temperature ramp rates of the systems. This can confound time experiments, since only certain orders of time units can be used for each anneal system.

Another method of annealing is laser annealing. This technique uses a high powered laser similar to that of gas-immersion. However, this requires one of the methods of introducing dopants mentioned above, such as implantation. Laser annealing has several advantages; due to melting, the diffusivity of the dopants is greatly enhanced [3]; the thermal constraints are removed, since the laser can be controlled such that it heats only the surface of the silicon. However, the melting process can cause much of the dopant atoms to be lost due to diffusion out of the silicon [3].

1.3 METHODS OF MEASURING ACTIVATION

Quantifying dopant activation is also a challenge. There is no direct way to count of the number of dopants in silicon, or determining which dopant atoms are active, without destroying that which is to be measured. This is made even more difficult due to

the relatively low amounts of dopant within the silicon. Unlike an alloy, concentrations of dopant rarely approach even one percent of the structure. This means that even if it were possible to count the atoms, it would require a large sample space since less than one atom out of one hundred would actually be something other than silicon. The fastest, non-destructive, method of quantifying activation is by measuring the sheet resistance of the implanted sample. Sheet resistance (R_s) is a measurement of the resistance of a material, normalized by the thickness (t) of the layer [4]. It has units of Ω/\square , which is defined as the resistance of one “square” of material. This is a convention that allows circuit designers to design devices without considering the processing of the material. The difficulty of this method is that the effect of carrier concentration (n) is inseparable from the effect of the carrier mobility of the silicon. The mobility (μ) could possibly change due to residual damage induced by the implant process. Equation 1.1 shows the simplified equation for sheet resistance, both the concentration and mobility are taken to be average values throughout the depth of the resistive region.

$$R_s = \frac{1}{qn\mu \cdot t} \Omega/\square \quad 1.1$$

The active dopant concentration can be modeled through sheet resistance by simulation. Simulations make several assumptions, such as the shape of the dopant profile and the mobility of the silicon. It is important to have independent measurements of doping concentration. Another method for determining doping concentration is by fabricating a metal-oxide-semiconductor (MOS) capacitor. The capacitance of this structure is partially based on the doping concentration; therefore the concentration can be obtained from the measurement. This technique only works for lower concentrations of doping, making its use somewhat limited.

Some destructive techniques can be used as well. Spreading Resistance Profiling (SRP) is used to determine the shape of the active doping profile. This technique allows for concentration measurements versus depth into silicon. It has its own share of inaccuracies, mostly with very high or very low concentrations of dopant. Secondary Ion Mass Spectrometry (SIMS) will be used to confirm the implant profile, as well as determine any changes due to annealing. By combining SIMS and SRP, it is possible to simulate and predict activation for a variety of implant and anneal conditions.

Techniques for measuring crystallinity and defects in the silicon have been employed. These are x-ray diffraction (XRD) and transmission electron spectroscopy (TEM). TEM and XRD are used to measure defects in the silicon to determine whether there is an increase in defects due to inactivated dopant ions.

1.4 OUTLINE OF THESIS

Chapter 2 begins by examining the theory of electrical activation. The topics included are: an explanation of defects within silicon, how atoms diffuse through the lattice, charge carrier mobility, and phase changes of silicon. Chapter 3 explains ion implantation, as it is the dominant method of doping silicon, and is the technique used here. In order to fully understand the impact of ion implantation on dopant activation; explanations are given on profile formation, ion damage to the lattice, and modeling of both implantation and activation. Chapter 4 discusses the analysis techniques used to measure activation and defects within the silicon. The dominant method is the four-point-probe, however, SRP, SIMS, TEM, capacitance, XRD and Hall measurements will also be discussed in detail. Chapters 5 and 6 present the data from the experiments.

Chapter 5 will cover donor activation, while chapter 6 discusses acceptor activation. Chapter 7 lists the conclusions that are drawn from the experiments.

Appendix A cover the non-critical process technology used in the experiments. Appendix B gives a detailed overview of the experimental setup, included sample identification. Appendix C lists the sheet resistance data for each sample. This list of data is given by order of sample ID numbers and must be correlated to appendix B to determine which sample is part of which experiment. Appendix D gives the raw data for the SRP data that was collected by Solecon Labs.

Chapter 2

Electrical Activation

2.1 DOPANT ATOM ACTIVATION

A semiconductor is a material that can be tailored such that it will conduct current in specified areas. The conductive properties are controlled by small concentrations of impurities, known as dopants. Silicon, the most common semiconductor, has four valence electrons; therefore it must either gain or lose four electrons to reach a stable state. The result is that silicon bonds with four other silicon atoms to create a stable structure. Dopant atoms change the conduction of the silicon by replacing one of the silicon atoms in the bonding arrangement. There are two types of impurities that can be used to change the conductive properties of a semiconductor; donors or acceptors. Donors are atoms that have five electrons in their outer orbital, and once inserted into the lattice, give this extra electron up to maintain a stable bonding configuration. This is illustrated in Fig. 2.1. This extra electron is then free to move about the crystal structure and can contribute to conduction. Since an electron is added to the system, this creates more negative charge carriers, therefore a region with a majority of donor atoms is known as n-type. It should be noted that the donor atom itself then has a positive charge, due to the missing electron. This maintains charge neutrality throughout the silicon. Atoms used to create n-type regions are phosphorus, antimony, and arsenic; all group five elements on the periodic table.

Similarly, acceptors are atoms that contain only three valence electrons. When these atoms replace silicon, they require an extra electron to achieve a stable bonding

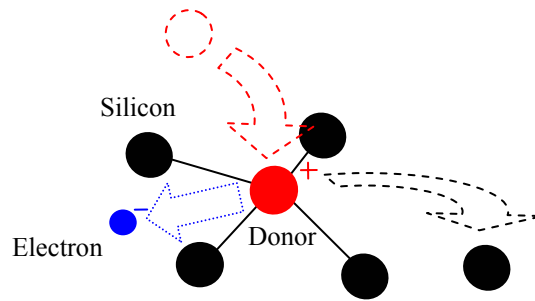


Fig. 2.1 – Atom substitution as an activation mechanism.

arrangement. This results in the contribution of a hole, or the absence of an electron, to the electrical conduction within the silicon. The hole is a positive charge carrier, therefore the region with mostly acceptor atoms is known as p-type. The acceptor left behind then has a negative charge. The atoms that can be used to create p-type regions are boron and indium.

There are several different choices for atoms to create either n-type or p-type regions in silicon. These atoms have different sizes, masses and bonding properties. Some atoms fit better in the silicon lattice. Arsenic fits in the silicon lattice best of all dopant atoms, therefore a higher concentration of arsenic atoms can be placed into the silicon crystal without having them form precipitates. This is referred to as solid solubility limit, and in the case of dopants, there are two types of solubility, the total solid solubility and that which can electrically activate. There is a physical limitation to the number of ions that can substitutionally exist in silicon (active solubility), as well as the number of ions that can remain within the crystal in either substitutional or interstitial sites (total solubility). In addition, the greater the mismatch between the dopant and the lattice, the more strain will be induced on the crystal structure, causing the formation of defects (stacking faults and dislocations) as the doping concentration is increased.

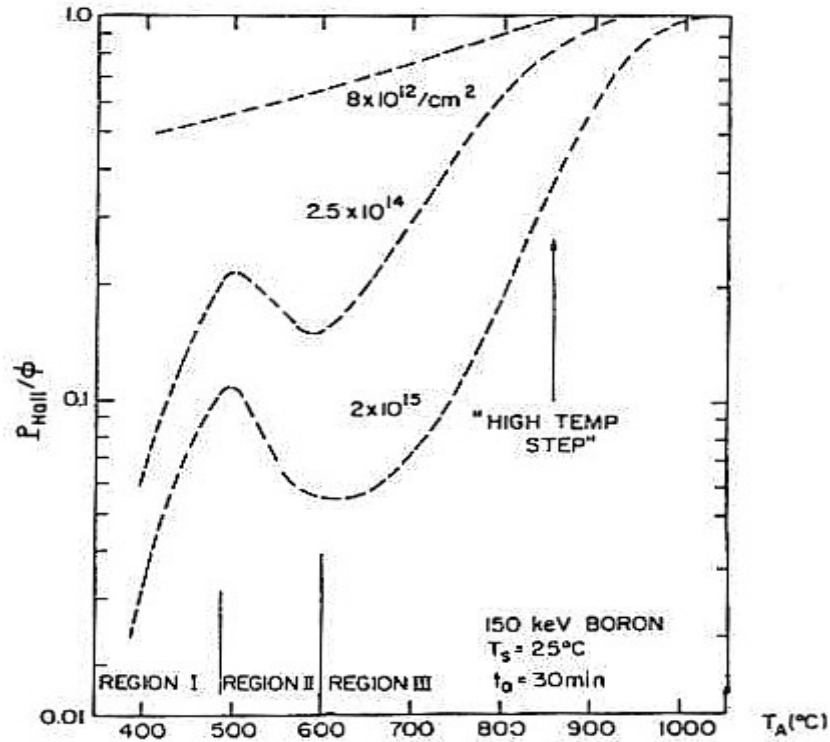


Fig. 2.2 – Low Temperature activation effects, for non-amorphized silicon [2]. P_{Hall} refers to the measured Hall dose; refer to section 4.3 for more details.

The method of activating dopant atoms is a process referred to as annealing. Energy in the form of heat is applied to the semiconductor. This energy must be sufficient to allow the dopant atoms to displace the silicon and form bonds with its neighbors. The temperature of the anneal process is a primary factor in determining how many of the dopants activate. In general, as the temperature increases, the amount of activation also increases. However, there are several factors that complicate this process. The amount of dopant in the silicon, referred to as the dose, actually affects the amount of dopants that activate. Fig. 2.2 shows literature data for activation of boron at isochronal or constant time, annealing conditions. Note the decrease in activation around 600°C; this de-activation is due to formation of dislocations in the lattice, at which dopants can segregate [2]. High temperature processing is required to remove these defects, as they

can only be removed by a re-ordering of the lattice. Therefore it is critical in investigating low temperature activation that these defects do not form, as they cannot be removed. Therefore, when considering a low temperature process, it is necessary to achieve the highest amount of activation, without creating an excess of defects in the silicon. However, induced crystal disorder can enhance the amount of activation, requiring a balance to be maintained.

2.2 LATTICE DEFECTS

Table 2-1
Atomic Radii and Volumes

| Element | Atomic Radius (Å) | Atomic Volume (Å ³) | Atomic diameter (Å) |
|------------|-------------------|---------------------------------|---------------------|
| Boron | 0.85 | 2.57 | 1.70 |
| Fluorine | 0.72 | 1.56 | 1.44 |
| Silicon | 1.18 | 6.81 | 2.35 |
| Phosphorus | 1.10 | 5.58 | 2.2 |
| Argon | 0.98 | 3.94 | 1.96 |
| Arsenic | 1.20 | 7.24 | 2.40 |

The silicon crystal has a diamond lattice structure. This structure is composed of two face-centered cubic structures, offset by $a/4$ [5] as shown in Fig. 2.3. The constant a is the length of one side of the cube and is referred to as the lattice constant. This structure is known as the unit cell, and contains eight atoms. The packing fraction, or amount of space filled within the unit cell can be calculated by finding the volume of the silicon atoms multiplied by the number of atoms and dividing by the volume of the unit cell.

$$pf = \frac{32\pi}{3} \left(\frac{r}{a} \right)^3 \quad 2.1$$

where r is the atomic radius and a is the length of the cubic unit cell. The atomic radius for atoms of interest in this investigation is shown in Table 2-1. The packing fraction for the silicon lattice is found to be 0.34, which indicates that the lattice contains a large amount of open space. This implies that there is some space for additional atoms that are not contained within the silicon. The minimum distance between two atoms is equal to the diameter of a silicon atom. This calculation assumes a hard-sphere model of atoms; with this model, the largest atom that can fit between the lattice is another silicon atom. According to Table 2-1 only arsenic atoms are larger than silicon; therefore all other atoms relevant for this experiment can exist interstitially within the silicon lattice. In actuality there could be some deformation of the electron cloud, allowing the larger arsenic atom between two silicon.

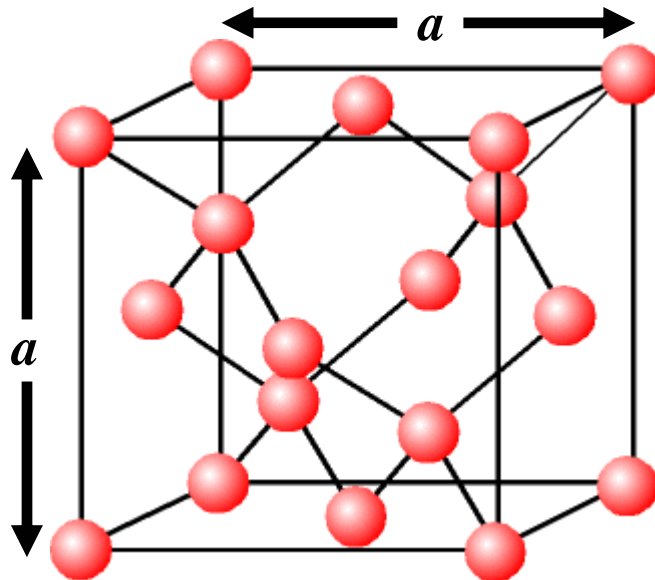


Fig. 2.3 – The diamond lattice, picture courtesy of [6].

Defects within silicon are classified by the dimensions of the defect; point, line, plane, and volume defects [7]. Line defects are one dimensional in size and are shifts in a crystal plane, relative to another. Planar defects include grain boundaries and stacking

faults. These defects are caused by thermal processing and consist of a series of dislocations that bound the plane. They are generally associated with mismatch between lattice planes [7]. Point defects in silicon can be categorized into interstitials and vacancies. Interstitials are atoms that occupy spaces within the crystal structure. When a silicon atom leaves the crystal structure to form an interstitial it leaves behind a vacancy. This creation of a vacancy-interstitial pair is known as a Frenkel defect [8]. A simpler type of defect is known as a Schottky defect, and is a cation and anion vacancy pair [8]. Under equilibrium conditions both interstitials and vacancies exist due to the vibrational energy of the lattice. The concentration of vacancies at thermal equilibrium is given by:

$$N_v = N_0 e^{\frac{-E_{av}}{kT}} \quad 2.2$$

Where N_v is the number of vacancies, N_0 is the number of silicon atoms and is equal to $5 \times 10^{22} \text{ cm}^{-3}$, k is Boltzman's constant, and T is temperature. E_{av} is the activation energy required to create a vacancy and is 2.6eV for silicon [2]. This expression comes from Boltzman statistics and assumes N_v is much less than the value for N_0 . At room temperature the concentration of vacancies is $1 \times 10^{-21} \text{ cm}^{-3}$, which is basically zero. At 600°C the number rises to 7.2 cm^{-3} , while at 1000°C it is $4 \times 10^9 \text{ cm}^{-3}$. Fig. 2.4 shows the temperature dependence of vacancies, while the number remains small on an absolute scale, the vacancies increase dramatically as the temperature is increased.

If the heat is lowered fast enough, the silicon can be quenched, giving no time for the vacancies and interstitials to recombine, allowing these defects to exist at lower temperatures. A similar expression exists for interstitial defects with activation energy for silicon of 1.1 eV [2]. Vacancies and silicon interstitials are known as intrinsic point defects. Extrinsic defects include interstitial impurity atoms that are intentional or

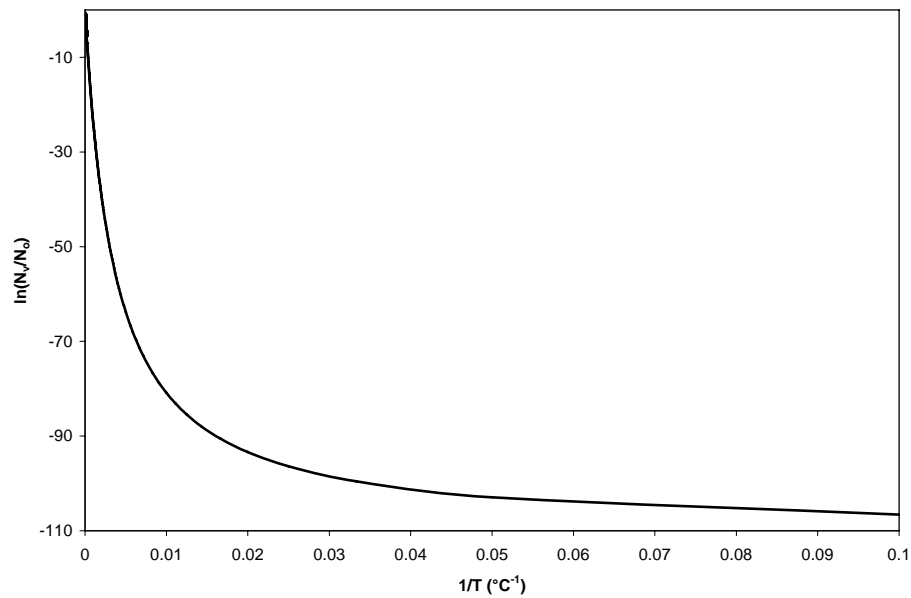


Fig. 2.4 – Arrhenius Relationship for vacancy concentration versus temperature.

unintentional. This category includes inactive dopant atoms that can exist interstitially in the silicon lattice. In fact, the presence of any dopant atom can increase the interstitial concentration, as the displaced silicon must then exist interstitially if the dopant concentration exceeds the concentration of vacancies. Interstitial-vacancy pairs can annihilate each other in a similar fashion; therefore defects are constantly being created and destroyed whenever there is enough energy. The number of vacancies is important from an activation standpoint, since during the anneal process the dopant atoms must be able to find a vacant site in order to activate. If more vacancies are present, a higher level of activation will be possible. From a probability standpoint, a high concentration of vacancies combined with a low concentration of interstitials will give the highest chance of impurity activation.

2.3 DIFFUSION

Diffusion, in general, is the process of net movement from an area of high concentration to one of low concentration. In this particular case, the process of diffusion refers to dopant diffusion throughout the silicon crystal. Since the dopant atoms must migrate to a vacant lattice site in the crystal in order to activate, diffusion can be used to assist this process. The more the atoms move within the silicon, the greater chance they have of locating a vacant site for activation. There are two primary types of diffusion within silicon; substitutional diffusion and interstitial diffusion [2].

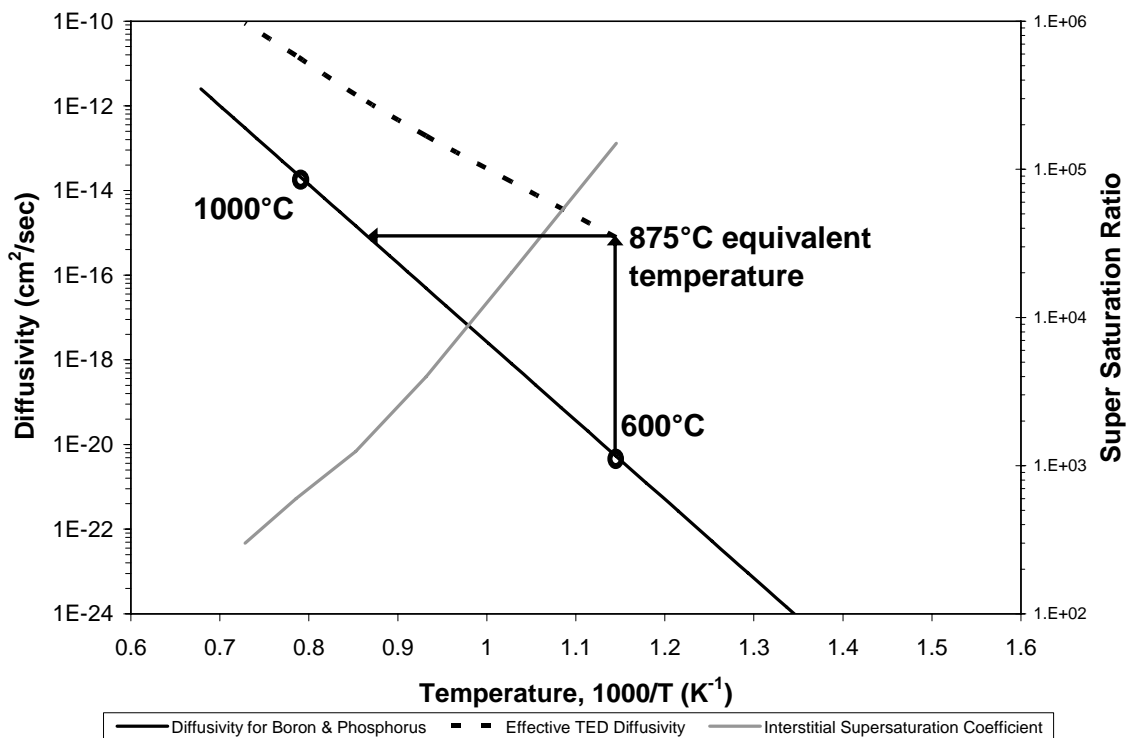


Fig. 2.5 – Diffusivity for boron and phosphorus as a function of $1000/T$ [9]. The worst-case scenario for the enhancement due to TED gives increase of five magnitudes in diffusivity at $600^\circ C$, equivalent to $875^\circ C$ under equilibrium conditions.

Substitutional diffusion is where the atoms diffuse through the crystal structure by moving from one lattice site to the next, following the formation and/or movement of

vacancies. This diffusion does not necessarily enhance the activation of the system, since the atom is already within the lattice and providing a charge carrier for conduction. However, as diffusion inherently spreads atoms, the concentration of dopants within a region is decreased.

Interstitial diffusion is a method of diffusion that does not rely on the crystal structure, rather the spacing between the atoms. The atoms can move throughout the lattice without forming bonds at a lattice site. This process, from an activation standpoint, is more desired, since it allows the atoms to move within the silicon until they find suitable bonding sites. Both types of diffusion have different mechanisms and activation energies.

The amount of diffusion that can occur is based on the energy of the system. Thermal diffusion in silicon is a well understood process. The amount of time that the energy is applied to the semiconductor is another important factor controlling the amount of diffusion that takes place. The temperature and the time are the two main components of diffusion, and are collectively referred to as the thermal budget. In other words, the same amount of diffusion can take place at a lower temperature if given enough time. The rate of diffusion as a function of temperature is controlled by the diffusivity coefficient, which is related to the flux of motion through an area.

$$D = D_0 \exp\left(\frac{-E_a}{kT}\right) \quad 2.3$$

D_0 is the frequency factor related to the vibrational frequency of the crystal lattice, E_a is the activation energy for a specific dopant ion and lattice, usually in the range of 3-5 eV for silicon, k is Boltzman's constant, and T is the temperature [2]. Equation 2.2 shows the Arrhenius relationship of diffusion and temperature. The true thermal budget of the

system is the product of the time and the diffusivity coefficient. This experiment is limited to 600°C, a temperature, at which diffusion should be negligible. The diffusivity coefficient for boron and phosphorus through silicon is near $5 \times 10^{-21} \text{cm}^2/\text{s}$ at 600°C while at 1000°C, the diffusivity is $2 \times 10^{-14} \text{cm}^2/\text{s}$; seven magnitudes larger. Therefore, conventional diffusion cannot provide any enhancement to the activation of the dopant atoms. Fig. 2.6 illustrates the effect of a 600°C rapid thermal anneal on boron. The position of the boron atoms remain unchanged by the anneal process.

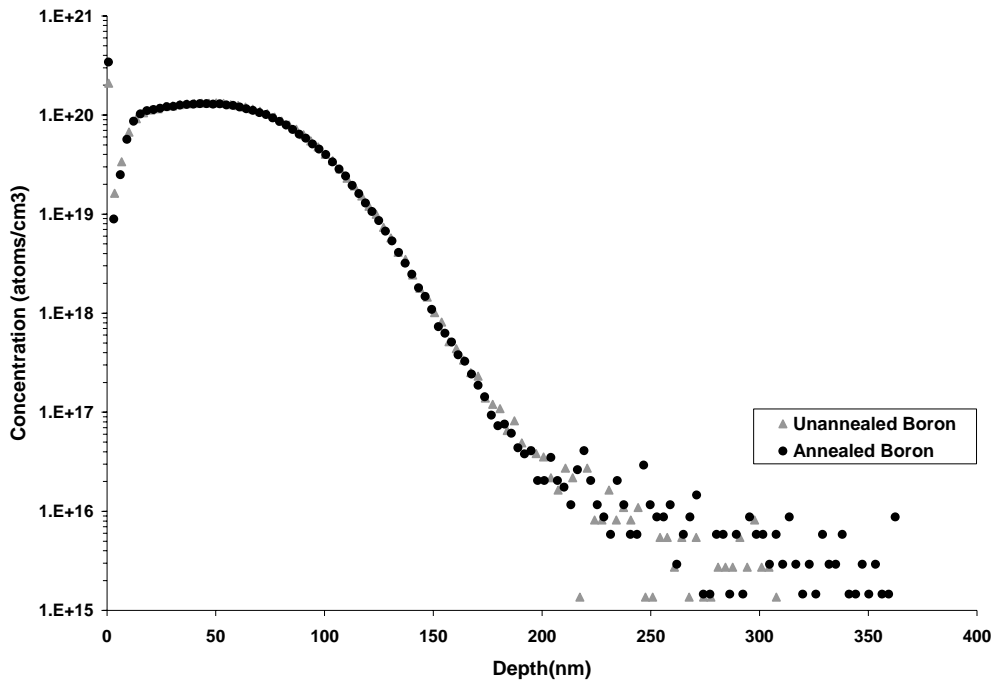


Fig. 2.6 – Boron implants annealed at 600°C.

Transient enhanced diffusion (TED) is an important phenomenon for low temperature annealing. It occurs significantly with boron atoms that are annealed at lower temperatures (670-900°C) [2]. This effect is caused by dissolving of large clusters of defects adding interstitial silicon atoms into the lattice during the annealing process and enhancing the diffusion of the boron atoms. Below this temperature range, the

diffusivity coefficient is low enough to counteract any TED; the defects that promote the effect cannot dissolve at temperatures below 670°C. As Fig. 2.5 shows, the enhancement in diffusivity at 600°C is five magnitudes; however, this is still not enough diffusion to be considered significant. As the name suggests, this effect is transient, it only occurs at the beginning of a thermal process, typically during the ramp-up to a steady-state temperature. For high-end transistor processing, with the goal of creating a shallow, highly concentrated region, this effect is very detrimental. The temperature of the diffusion is reduced to limit the amount of diffusion; however, TED causes an enhancement at these low temperatures that may be significant enough to make up for the difference in diffusion rates. There are several methods known to counter this effect. The first being a spike anneal process, where the time of annealing is kept as short as possible, allowing for very little diffusion to take place, yet providing enough thermal energy for the activation to occur. Some research has been done to demonstrate that the use of fluorine ions introduced into the silicon; has been shown to reduce TED by bonding with the silicon interstitials that promote this diffusion [10].

2.4 CARRIER MOBILITY

In order for carriers to contribute to conduction, they must be free to move throughout the silicon crystal. Carrier mobility, given by the symbol μ , is the measure of how well the holes and electrons can move throughout the silicon; it is the proportionality constant between carrier velocity (v) and electric field (E).

$$v = \mu E \quad 2.4$$

The value of the mobility depends on the type of carrier; holes are not as mobile as electrons, since effectively the motion of a hole requires many electrons to move all at

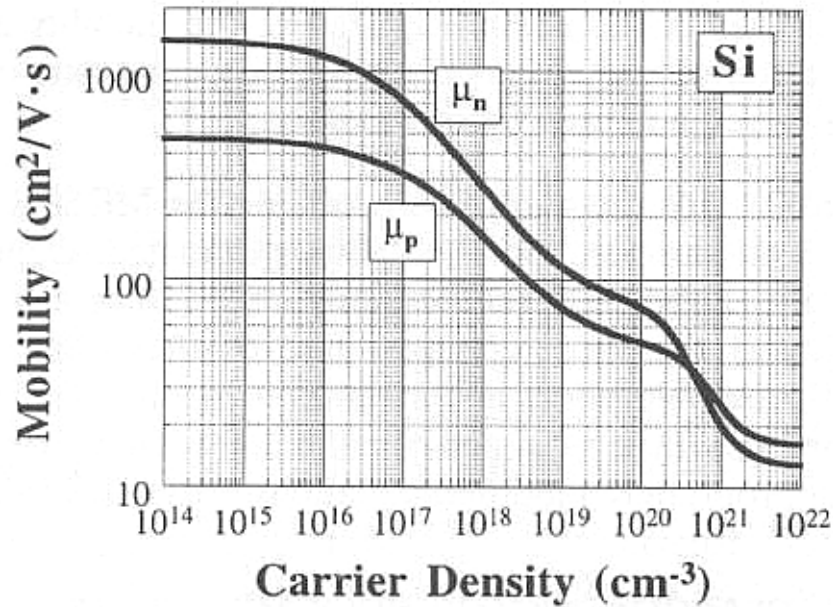


Fig. 2.7 – Mobility as a function of carrier concentration and dopant type, generated from experimental measurements, from [11].

once. Mobility is degraded by carrier scattering; the more carriers scatter randomly, the longer it takes to travel when influenced by an electric field. There are four factors that have a major influence on mobility: doping concentration, temperature, crystal defects, and lattice structure. The crystal lattice spacing influences mobility as it is the measure of how much space exists between atoms in the lattice. This means that if the lattice is not cubic, the mobility will depend on the direction of the carrier motion. The temperature effects carrier mobility for a similar reason; since as the vibrational energy of the atoms increases, the more likely they will be to influence the path of the carriers. The doping concentration can influence the path of the carriers, since they are charged ions, the dopant atoms can attract or repel carriers, creating more scattering. Defects in the silicon can also influence mobility by creating additional carrier scattering due to both collisions and charge centers [4].

$$\sigma = q(n\mu_n + p\mu_p) \quad 2.5$$

Mobility is important since it has a direct relationship to the conductance (σ) of material, as shown by equation 2.5. Both the concentration of holes (p) and electrons (n) influence the conductance; however, these are weighted by their respective mobility values, μ_n and μ_p . In this study, when determining how much dopant becomes active, mobility comes into play. Both active and inactive dopants affect mobility, but in a different manner. Inactive dopant behaves similar to an interstitial defect in the lattice lowering the mobility by decreasing the mean-free path of the carriers. The total amount of dopant in the silicon will decrease the mobility; however, this is not a linear relationship and is shown in Fig. 2.7. The mobility will in turn affect the conductance of the silicon, which is also influenced by the active doping concentration.

2.5 AMORPHIZATION AND RE-CRYSTALLIZATION

Due to the lack of diffusion at the limited temperature regime, alternate methods of enhancing dopant activation must be used. Re-crystallization of the silicon lattice can be used to provide an enhancement to activation. Solid-phase epitaxy (SPE) is the process of rebuilding an amorphous region of silicon by using the underlying crystal as a base. Therefore, if the amorphous region encloses the doped region, but does not extend throughout the entire depth of the silicon, re-crystallization will occur. Fig. 2.8 shows the effect of amorphization on the activation of phosphorus. As the implanted dose increases, the temperature required to activate the same level of dopants increases, as more diffusion is required to give the dopant atoms the opportunity to find vacant lattice sites. Once the silicon becomes amorphous, the activation exceeds the low dose implant activation, as diffusion is no longer necessary since the dopants are swept into the lattice during SPE along with the silicon. Thermal energy is still required to crystallize the

silicon, however, the energy needed is much less than the amount required for full activation. Typical silicon re-crystallization is done at a temperature range of 500°C to 650°C. The range is ideal for the processing constraints, and provides an enhancement to the dopant activation. The boost to activation comes about in the transition from the amorphous to the crystalline state. As the lattice is rebuilt, the dopant atoms can be swept into the lattice in place of the silicon. Therefore, the dopants do not have to find a suitable bonding site, as one is created for them. According to prior research, the solid-phase regrowth rate of silicon at 550°C is 1.5 Å/s [3]. Due to the rate of re-crystallization, anneal time still plays a major factor, as the whole of the silicon may not be crystallized if the anneal is not long enough.

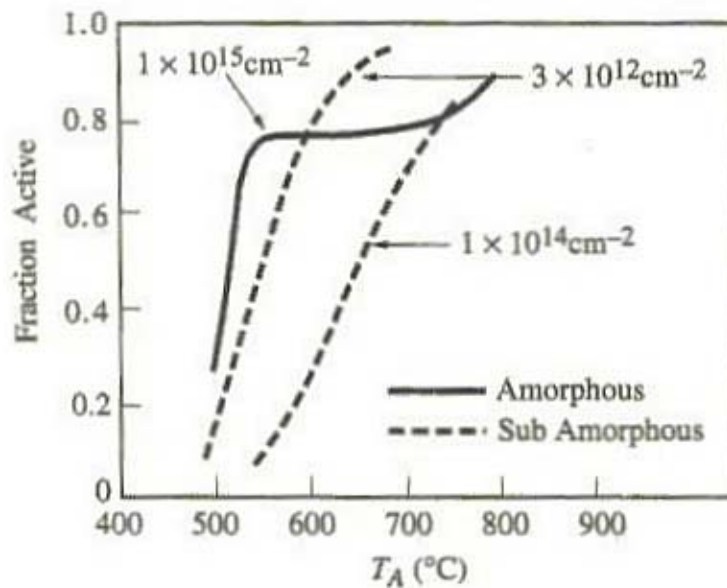


Fig. 2.8 – Literature dopant activation for phosphorus, showing the self-amorphization effect on activation [5]. Sub Amorphous refers to the implanted dose that is not sufficient to create an amorphous region in the silicon.

The danger to creating an amorphous region to enhance dopant activation is that the state of the silicon can affect the mobility of the charge carriers. If the long-range

order of the crystal is disrupted, it becomes more difficult for carriers to move within the lattice. An amorphous region is a complete lack of order, therefore, if the silicon is not completely re-crystallized, the mobility of the carriers can suffer. This loss in mobility can be enough to counteract any enhancement gained by amorphization; therefore this technique cannot be used if the silicon cannot be restored to a crystalline state.

Chapter 3

Ion Implantation

3.1 ION IMPLANTER TECHNOLOGY

Ion implantation is a process used to introduce impurities into a wafer. The process involves accelerating a beam of charged ions into the surface of the wafer. Implantation is the preferred method of doping silicon for most transistor fabrication. The advantage of ion implantation over other methods of doping silicon is due to the degree of control over the amount of ions introduced, or the dose, and the depth to which the ion distribution extends [2]. The amount of ions introduced can be controlled, uniformly across a wafer, to within one percent. The implanted dose is quantified as a number of ions per area (cm^{-2}) and is given the symbol ϕ . To determine the implanted dose for a given process, the ion beam current, (I) and implant time, (t) must be known. Using these parameters, the dose can be determined as shown in equation 3.1.

$$\phi = \frac{I \cdot t}{q_i A} \quad 3.1$$

Where A is the implanted area and q_i is the charge of the ion [2]. The ion implanter functions by passing a high current through a tungsten filament and ionizing a source gas to create plasma. The source gas must contain the ion of interest. Common source gases are phosphine (PH_3), boron trifluoride (BF_3), and arsine (AsH_3). These gases are dangerous, as phosphine and arsine are pyrophoric, meaning they ignite on contact with air, while all three gases are poisons. The ionized gas is then passed through a mass

spectrometer to select the appropriate ion. Various ion species are available. For phosphine, ^{31}P is the standard species used; however, PH^+ and PH_2^+ are also available.

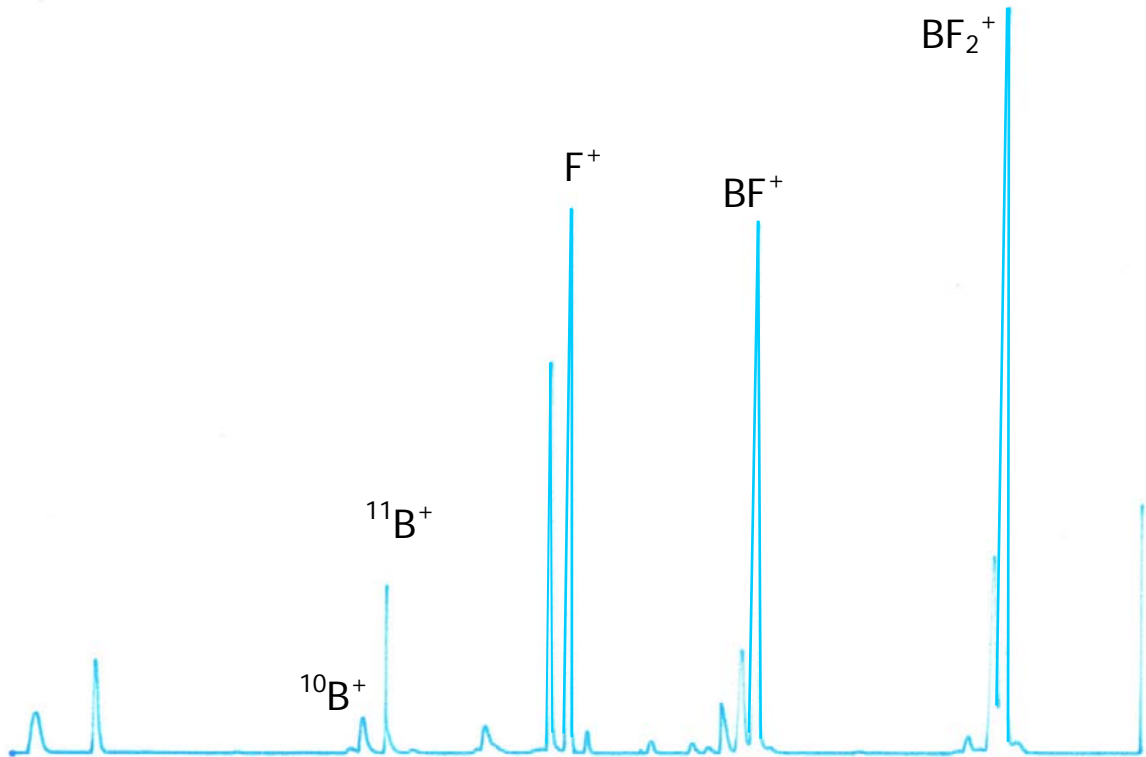


Fig. 3.1 – The boron trifluoride implant mass spectrum. Spectrum done on a Varian 350D Ion Implanter.

For boron trifluoride, ^{11}B is the common source for boron, though BF_2^+ is also a common implant molecule due to its greater mass. Other ions available for this source are: ^{10}B , F^+ , and BF^+ . The full mass spectrum for BF_3 is shown in Fig. 3.1; the height of the peaks shows the relative amount of each species within the plasma. After the appropriate ion is selected, the ions are accelerated to the desired energy by the acceleration voltage. This is the main factor that controls the depth of the implanted ions. The kinetic energy can range from several keV up to MeV depending on the required depth. In order to cover an entire wafer with the ion beam, scanners are used to sweep the beam in both the x- and y-directions.

3.2 IMPLANTATION PROFILE

Ion implantation places dopants within silicon, however, the distribution of the ions can influence the conductive properties of the region, and therefore, it is necessary to have a model that describes the profile. Implant profiles are given as a depth versus the concentration of ions. The simplest model for an implant profile is by a Gaussian distribution. The equation for this distribution is shown in eq. 3.2.

$$N(x) = \frac{\phi}{\sqrt{2\pi}\Delta R_p} \exp\left[-\frac{(x - R_p)^2}{2\Delta R_p^2}\right] \quad 3.2$$

where $N(x)$ is the concentration of ions per volume; x is the distance into the wafer; R_p is a parameter known as the range, which is the range of the ion in the x -direction and is the average penetration depth into the silicon as well as the location of the maximum concentration of dopants; and ΔR_p is a parameter known as the projected straggle, or the deviation from the average range. R_p and ΔR_p are statistical parameters used to fit the ion distribution to a Gaussian profile [2]. This model can be used to predict the desired junction depth of the profile. Junction depth is defined as the depth at which the concentration of the profile is equal to the background concentration of the wafer. By setting $N(x)$ equal to this concentration, x will be equal to the depth of the junction, referred to as x_j . A model of ion stopping is given by Lindhard, Scharff, and Schiott, or LSS theory of implantation [2]. It should be noted that this theory only applies for implanting into amorphous material; crystalline or semi-crystalline materials behave differently due to ion channeling. The theory comes about from examining how ions come to rest within the silicon material. There are two methods of energy loss for an implanted ion: nuclear and electronic.

Nuclear energy loss comes from physical collisions with lattice atoms, while electronic energy loss is the electric field interactions between the electrons in the lattice and the nuclear charge of the implanted atom that slows the velocity of the ion. Nuclear energy loss is dependant on the speed of the incoming ion; if the ion is traveling at high velocity, there will be fewer opportunities for a coulombic interaction, and therefore the ion will be slowed less by collisions. The mass of the ion will increase the amount of energy lost by collisions, since the ions cannot fit as easily in the spaces between lattice atoms. Also, for a given energy, the ion speed is governed by the mass, since kinetic energy is related to mass and velocity. Electronic energy loss is related to stopping a particle in a viscous medium [2] and can be modeled as a function of the square-root of the ion energy.

$$S_e(E) = k_e(E)^{1/2} \quad 3.3$$

Where $S_e(E)$ is the energy loss per unit length due to electronic stopping and k_e is a constant related to the ion and target atomic numbers and masses [2]. Fig. 3.2 shows the values of $S_n(E)$ and $S_e(E)$ for boron, phosphorus, and arsenic as they are the most common implanted ions. It should be noted the that the cross-over point between nuclear and electronic energy loss for each ion species is drastically different, which leads to very different stopping mechanisms, and therefore profiles, for each type of atom.

A major difference with implanting into a crystalline material is the phenomenon known as channeling. In a crystalline material, there is a regular arrangement of atoms. Due to this regularity, there exist relatively large open spaces where there are no atoms for the ions to encounter. This allows the implanted ions to penetrate much deeper into the crystal than they otherwise would be able. To prevent channeling, ion implantation

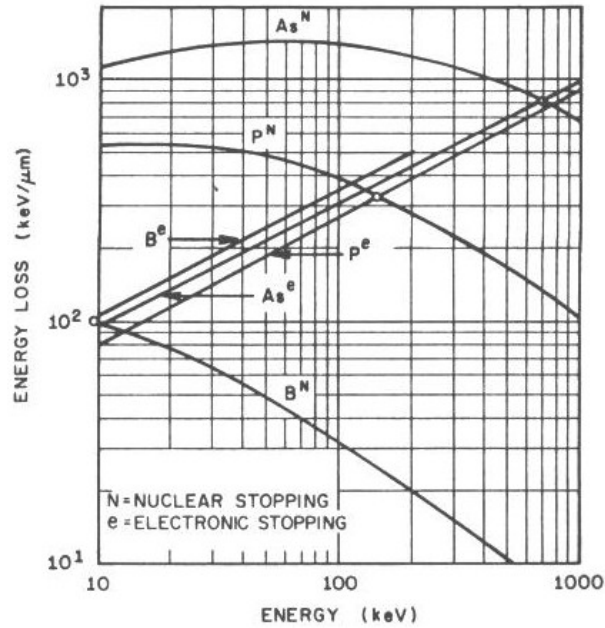


Fig. 3.2 – Ion energy loss as separated by components, from [2].

into silicon is typically done with the wafer at a favorable angle, or with an amorphous material on top of the crystal [2]. All implants involved with this experimentation were done at a 7° tilt. However, since the wafer must be clamped to a chuck during the implant, it can be bowed slightly, which will change the incident angle across the wafer. Therefore it is not wise to rely only on an angle correction, as the degree of channeling could then be different across the wafer. A pre-amorphization implant can also be performed to reduce the amount of channeling. This removes the lattice ordering at the surface of the silicon. A combination of all three techniques will effectively suppress ion channeling; however it cannot be eliminated due to possible scattering into open channels.

Due to the complexity of modeling ion implantation, simulation software is often used. The software used in this case is SRIM, or Stopping Range of Ions in Matter. This software can model any ion implanted into any substrate, however for the purposes of this experiment, the substrate is limited to silicon and silicon dioxide for screening.

SRIM does not simulate crystal structures, therefore ion channeling is not present. However, it does simulate ion displacement and collisions, which makes it effective for modeling lattice damage.

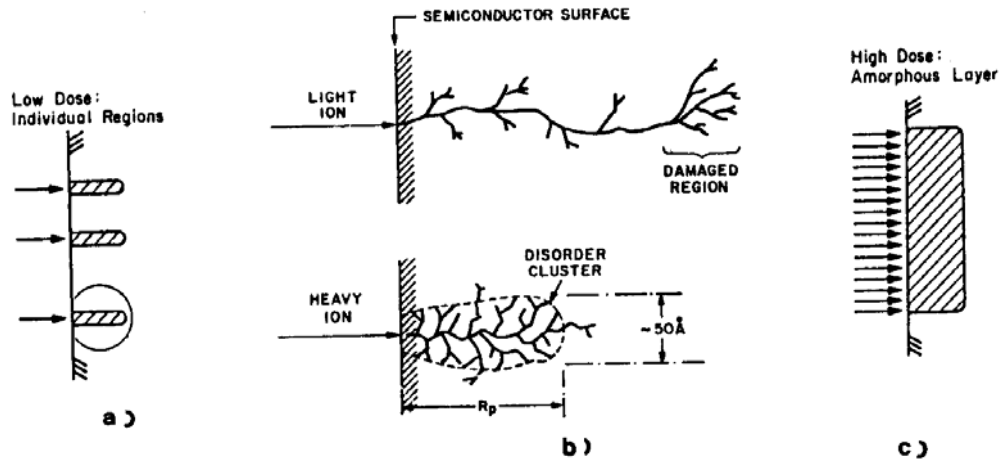


Fig. 3.3 – Degree of implant damage as a function of ion mass and dose. (a) individual amorphous regions created by a low implant dose. (b) Variation between light and heavy ions. (c) A high dose continuous amorphous layer.

3.3 ION-INDUCED LATTICE DAMAGE

Ion implantation is an excellent technique for introducing impurities into a silicon crystal; however, the process of accelerating ions into the crystal causes the silicon atoms to be displaced. The displaced silicon is now a defect in the silicon lattice, as is the vacant site it leaves behind. Defects created by the implant process are referred to as primary damage [2]. Following an anneal, remaining defects combined with the implanted ions that did not immediately join the lattice can create large clusters that inhibit conduction and ruin the devices if not removed. These defects are known as secondary defects, since they are created in a process step following the implant [2]. The mass of the implanted ion is also a significant factor that affects the amount of

damage. For some ions, the mass is great enough to create localized amorphous regions; however, ions such as boron are light enough that no single ion creates an amorphous region. Therefore, for a given ion, there is a threshold dose, or number of implanted ions, that is necessary to create a continuous amorphous region. If the dose is not high enough, or the ions too small to amorphize the layer, the collection of defects are known as primary crystal damage [2]. This damaged region can contain localized amorphous regions, however, since the whole layer is not continuous, the damage is removed in a different manner. These various implant conditions and the corresponding damage levels are illustrated in Fig. 3.3.

Defects occur where there are the most nuclear interactions. Therefore, the damage occurs once the ions have decelerated to a point where nuclear stopping can take over. Primary crystal damaged regions generally occur with low dose or light ion implants, and at the end of the ion range. Amorphization occurs when the ions are heavy enough to completely remove any order from the silicon crystal. A fully amorphous region is easier to repair than primary crystal damage; this is because the whole region is disordered. This process is known as solid-phase epitaxy (SPE). Amorphization is also desirable because it allows for more dopants to activate, for when the lattice rebuilds itself, the dopant atoms are swept in, achieving activation. On the other hand, primary crystal damage requires more thermal energy to repair, and therefore does not lend itself to activation enhancement. Fig. 3.4 shows SRIM simulations of a phosphorus implant. The important point to note from this simulation is the location of the ions as well as where the damage occurs. After the ions have lost much of their energy, they do not cause much damage to the silicon. Also note that the damage extends further than the

phosphorus. This is because the displaced silicon atoms can displace more of the silicon lattice if there is enough energy remaining.

3.4 PRE-AMORPHIZATION

A complete amorphous region is desirable for several reasons, outlined in chapter two. One strategy to create an amorphous region without relying on self-amorphization is to implant a non-reactive ion to create a damaged region before the dopant ions are implanted. This amorphous region is advantageous for a number of reasons. Since implantation is used, it allows for a controlled amorphous region to be created in specific locations, as well as providing a great deal of control for the depth of the amorphous region. It prevents ion channeling, although it is possible for the pre-amorphization ion to channel, allowing the formation of shallow implanted regions. It improves activation in ion species that cannot self-amorphize the silicon lattice due to size. Pre-amorphizations can also minimize transient enhanced diffusion (TED). There are several methods used to create an amorphous region. The first is to implant deep into the silicon, in order to amorphize the entire region where the dopant is desired. This prevents both channeling and TED. The second is to implant a shallow region, well above the depth required for the dopant implant. This method only prevents channeling, not TED [12]. It is similar to using a screen oxide without any additional film deposition. In both cases, the end of range of the pre-amorphization implant should not be near the edge of the dopant ion implant, since there will not be amorphization at the edge of the implant, only

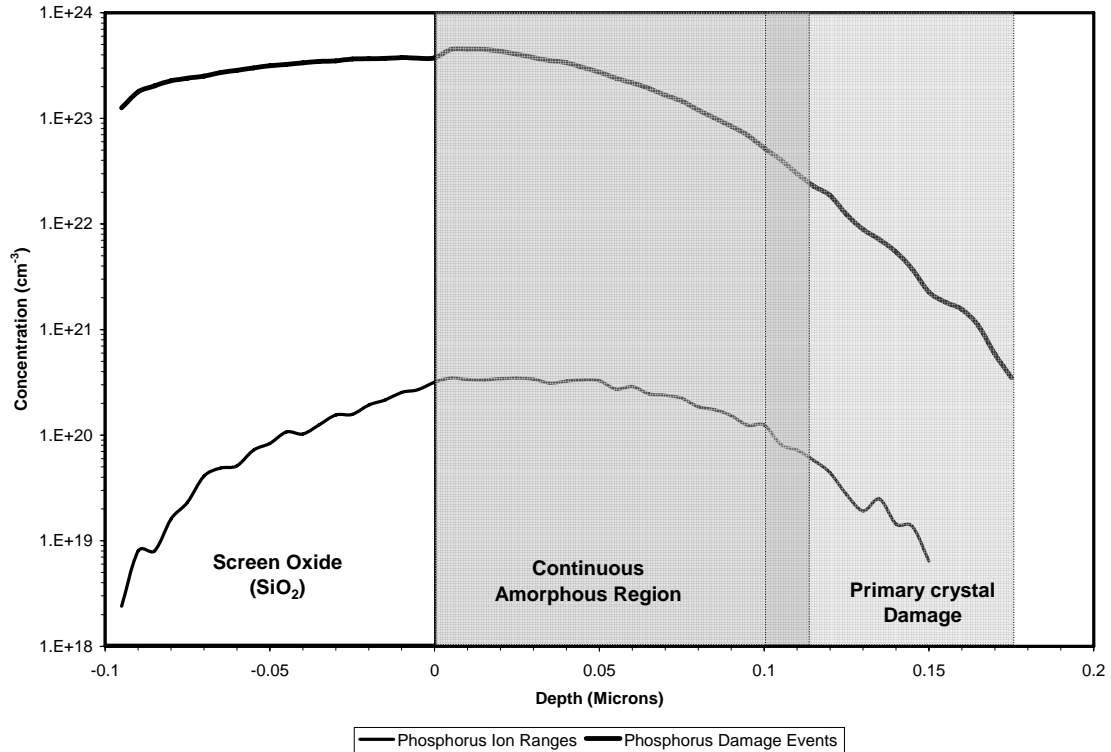


Fig. 3.4 – SRIM simulation of phosphorus implant into silicon showing, (lower curve) the ion penetration, (upper curve) the damage events, and the self-amorphized region. The region between the continuous amorphous region and the primary crystal damaged region represents the uncertainty in this boundary. Damage events are a summation of ion displacements and vacancies. The implant simulated was for a $4 \times 10^{15} \text{ cm}^{-2}$ phosphorus implant.

primary crystal damage. The defects on the edge of the implant will interfere with the dopant junction and activation. The concentration of atoms in the silicon from the pre-amorphization implant can influence the activation as well, since additional interstitial atoms are now present. These atoms can either remain interstitials, combine with other interstitials to form larger defect cluster, or enter the lattice, annihilating a vacancy. The probably of each of these is not equal, and is dependent on the atom used. There are several ions that can be used to create an amorphous region that will not interact with the crystal lattice. They include silicon and germanium, which are traditional pre-amorphization ions, as well as fluorine and argon, which were used for this study due to

availability. Silicon and germanium are the most commonly used for industry purposes [13], since the introduction of more silicon into a silicon wafer will have a minimal effect once the damage is removed. The only danger being the creation of silicon interstitials and defect clusters. This is not usually an issue if followed by a high temperature anneal, however this is not available due to the temperature constraints. Germanium is often used because of its high mass, similar to that of arsenic. However, germanium will not be used in any experimentation presented here, as silicon is the primary target material and implanting germanium is quite costly, making it infeasible for this study. Argon is an inert element that is used in most implanters in order to purge remaining gas from the plasma. Argon has a greater mass than silicon or phosphorus; therefore it can create more damage than either. Fluorine can be used, since there is already a source of fluorine ions from BF_3 , a typical source of boron in most implanters. Fluorine has a mass of 19 amu; therefore it requires a great deal more fluorine to create an amorphous region over that of argon or silicon. In addition, fluorine is a reactive element; therefore, it may react with dopant atoms and silicon interstitials, though it should not contribute to conduction. The BF_2^+ ion is commonly used for shallow junction boron implants, as the effective boron implant energy is lower. Therefore, the introduction of fluorine to the silicon lattice is not new, and should not interact in a detrimental manner with regards to activation.

3.5 IMPLANT AND ACTIVATION MODELING

One of the goals of this work is to develop a comprehensive model for electrical activation based on implantation profiles. Ion implantation modeling is quite well established and can be modeled a variety of ways. Ion distributions can be calculated by

hand using the Gaussian distribution model, or it can be simulated with either SUPREM or SRIM software. SUPREM is a semiconductor processing simulation package that includes ion implantation. It has several models available, however the software does not simulate activation; instead it assumes full electrical activation for extracting any material or electrical properties. SRIM software is an implant simulator; it simulates ion scattering, range, and damage from an implanted ion into a target material. The advantage of SRIM is that it can use any source ion and implant that into any type or combination of target materials. It is not concerned with electrical properties, only with ion penetration and collision events. SRIM software is used to predict the silicon lattice damage and determine the theoretical depth of amorphous regions created during an implant.

Fig. 3.5 and Fig. 3.6 show the threshold damage for phosphorus and boron implants due to increasing implant dose. These simulations are done at 92 keV for phosphorus and 34 keV for boron. Literature shows that the threshold amount of damage required to fully amorphize is $5 \times 10^{21} \text{cm}^{-3}$ or ten percent of the concentration of silicon atoms [14]; if this was true, a $5 \times 10^{14} \text{cm}^{-2}$ dose of boron would be sufficient to amorphize the surface of the silicon crystal. Therefore, for the purposes of this study, a higher level of damage will be necessary. Fifty percent of the silicon concentration, or $2.5 \times 10^{22} \text{atoms/cm}^3$ should be adequate.

As Fig. 3.5 shows the threshold phosphorus dose to completely amorphize is $5 \times 10^{14} \text{cm}^{-2}$ at 92 keV, and the depth of the amorphous region continues to grow as the dose increases. For lower doses, there is no amorphization present, and this damage exists as primary crystal damage. The threshold for Boron begins at $1 \times 10^{15} \text{cm}^{-2}$ as boron

has a smaller mass than phosphorus, it requires more ions to amorphize the surface. However, this dose only amorphizes the very surface and the range of boron ions extend far beyond

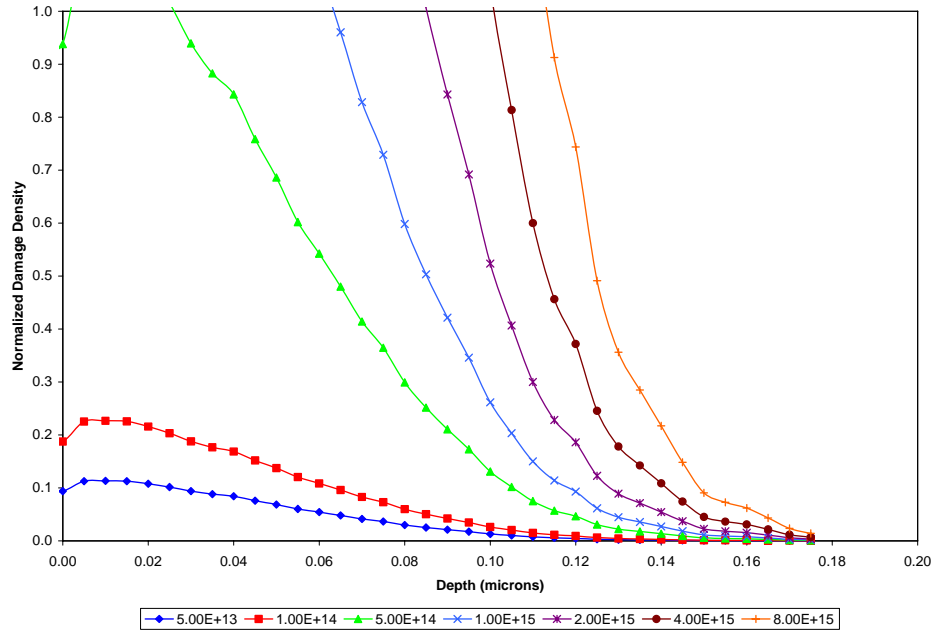


Fig. 3.5 – SRIM simulation of ion displacement for phosphorus (92 keV), normalized damage events for implant doses of 5×10^{13} to $8 \times 10^{15} \text{ cm}^{-2}$. Damage normalized to $5 \times 10^{22} \text{ cm}^{-3}$ silicon atoms.

this region. It should be noted that higher energies of boron will create a buried amorphous region.

A similar simulation was done to determine the optimal pre-amorphization dose. Fig. 3.7 shows the amorphization of fluorine. The amorphization threshold is once again chosen to be 50% of the total number of silicon atoms. At the chosen energy of 75 keV, even $5 \times 10^{14} \text{ cm}^{-2}$ is sufficient to create a small amorphous region at the surface. However this dose does not have a deep amorphous region, therefore will not encompass the entire active dose implant. Screening experiments are performed to determine the most effective fluorine dose in terms of maximum activation with the lowest dose possible.

This experiment varies the fluorine dose between 1×10^{15} , 3×10^{15} , and $5 \times 10^{15} \text{ cm}^{-2}$ as any other doses are shown here to be ineffective. The results of this experiment are shown in section 6.2, where the pre-amorphization results are shown.

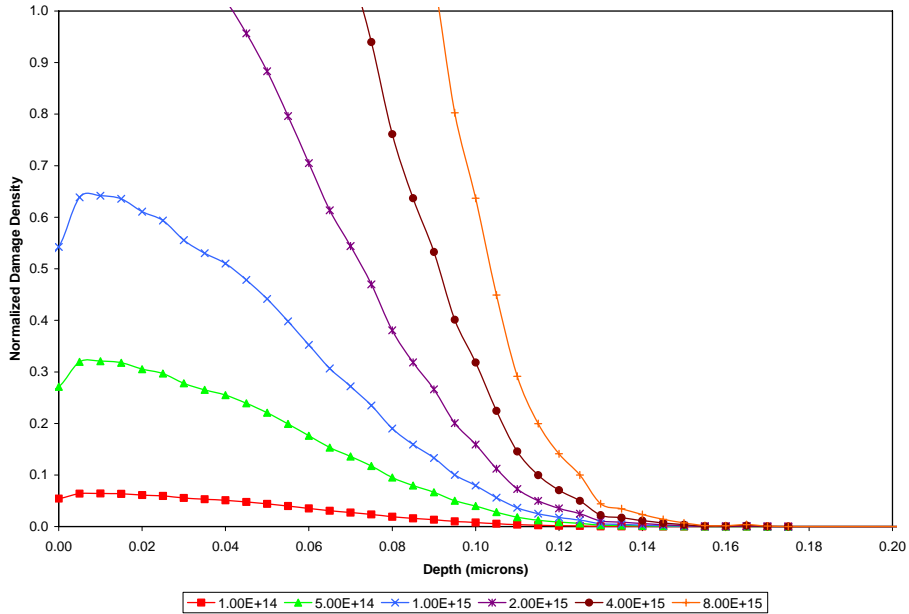


Fig. 3.6 – SRIM simulation for boron (34 keV) normalized damage events for implant doses of 1×10^{14} to $8 \times 10^{15} \text{ cm}^{-2}$. Damage normalized to $5 \times 10^{22} \text{ cm}^{-3}$ silicon atoms.

Argon and silicon are also candidates for a pre-amorphization process. Silicon is very similar to phosphorus in terms of damage, having a mass of 28amu. It was not possible to experimentally vary the implant dose of the silicon, due to the cost of the implant; therefore the pre-amorphization dose was chosen to be $1 \times 10^{15} \text{ cm}^{-2}$. Argon was simulated with SRIM and the normalized damage density is shown in Fig. 3.8. In this case, $2.5 \times 10^{14} \text{ cm}^{-2}$ is the minimal dose to create an amorphous region for the given implant conditions. Experimentally, all the doses shown are attempted and the optimal dose used for further processing. Section 6.2 discusses the results of this experiment.

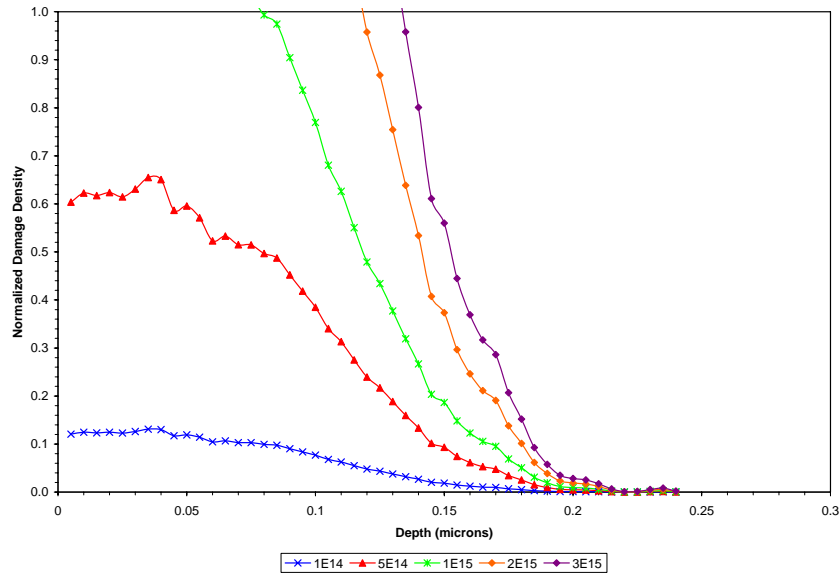


Fig. 3.7 – Normalized Fluorine Damage events for a 75 keV implant.

Electrical activation profiles can vary from the implanted profiles due to annealing processes or re-crystallization of the silicon. There are several basic types of profiles that illustrate the fundamental differences of the nature of activation. The first profile is a scaled activation profile. This assumes the activated dopant is exactly the same shape as the implanted profile, except scaled by some factor in both depth and concentration. This profile is what is assumed for any SUPREM modeling as it does not account for activation. The second type of profile is a depth dependant profile. This assumes there is some limit to the maximum depth of the activation region. This profile is likely for a self-amorphizing implant, such as phosphorus, as the bulk of the ion damage is linked to the highly concentrated regions. However, that does not mean it could not occur when a pre-amorphization is done.

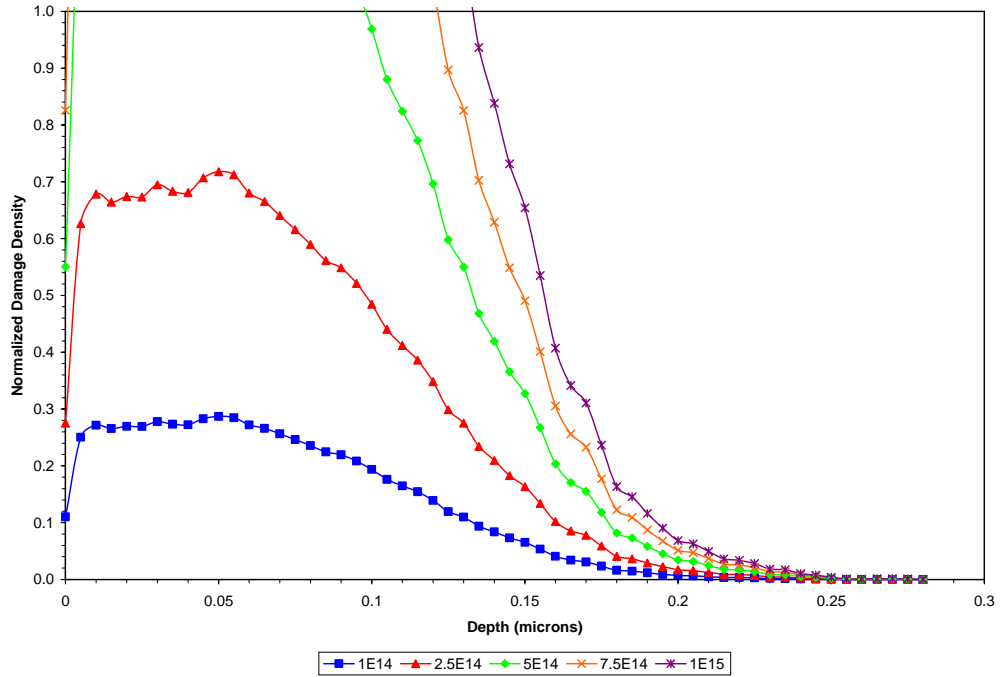


Fig. 3.8 – Argon normalized damage density for an energy of 170 keV.

Depending on the ion used in the pre-amorphization, due to competition for vacant lattice sites the activation could be limited to where the concentration of the other ion is lower, in this case, closer to the surface. The third activation profile is a clipped or concentration dependant profile. This assumes there is some saturation limit to the amount of dopant that can activate. There is evidence of all three types of profiles, and the true profile is most-likely a combination of concentration and depth dependence.

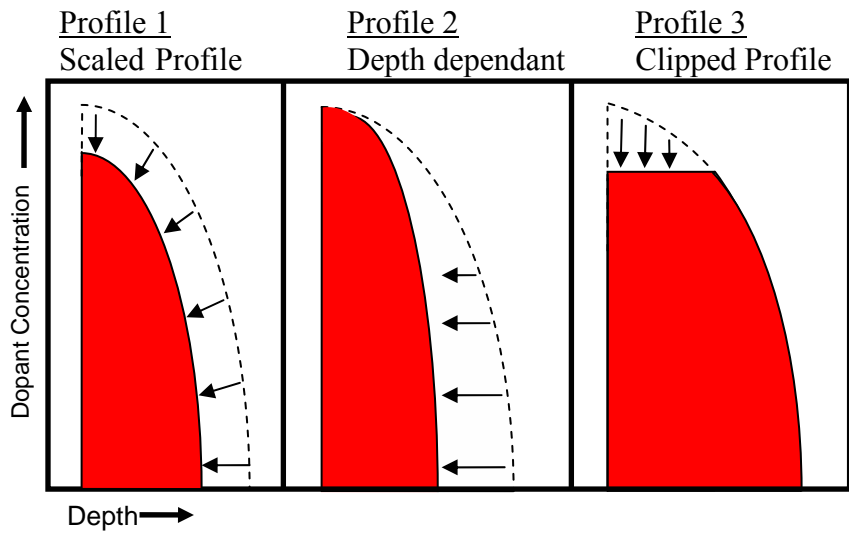


Fig. 3.9 – Activation profile possibilities, where the dotted line represents the implanted profile.

Chapter 4 Analysis Techniques

4.1 FOUR POINT PROBE

The methods available to determine active dopant in a silicon substrate are numerous; however they can be divided into two broad categories, electrical and optical. The simplest method of quantifying activation is sheet resistance. Sheet resistance is a thin film property based on the resistivity of the material. It is the resistivity for a specific thickness of material. Four-point probe is a technique that is used to measure the sheet resistance of a sample by using four equally spaced, collinear probes. The outer two probes are used to apply a current to the sample, and the resulting voltage is measured by the inner two probes. The applied current and measured voltage can be converted into a sheet resistance by the following equation:

$$R_s = \frac{\pi}{\ln(2)} \frac{V}{I} \Omega/\square \quad 4.1$$

The preceding constants are the geometric factor based on current distribution. This equation is applicable for samples with a thickness much less than the probe spacing [15]. The probe spacing must be equal for this equation to hold true, and the actual spacing is on the order of one millimeter. The sheet resistance measured can be used to determine the activated dose by using SUPREM software to reference the dose required for a specific R_s . The simulation assumes a scaled implant profile; therefore it is not really an active dose as it is an effective active dose. The amount of activation is determined by the ratio of activated dose to the implanted dose. A true measure of the active dose can be found mathematically by the following equation:

$$R_s = \frac{1}{q \int_0^{x_j} \mu \cdot n(x) dx} \approx \frac{1}{q \tilde{\mu} \phi} \quad 4.2$$

Equation 4.2 shows the relationship between sheet resistance and doping concentration. R_s can be approximated by the implanted dose (ϕ) and the effective mobility ($\tilde{\mu}$). A sheet resistance measurement is the most accurate method of determining resistivity and doping concentration, however, this does not mean that in the context of this experiment that it is the only method worth using [16]. The reason the active dose is determined by simulation rather than by this equation is that the mobility (μ) is dependant on the doping concentration therefore is impossible to separate these two values with this measurement technique. Even the simulation does not model the mobility properly, since the mobility depends on both the active and inactive doping, though with a different functional dependence. The SUPREM software does not model inactive doping.

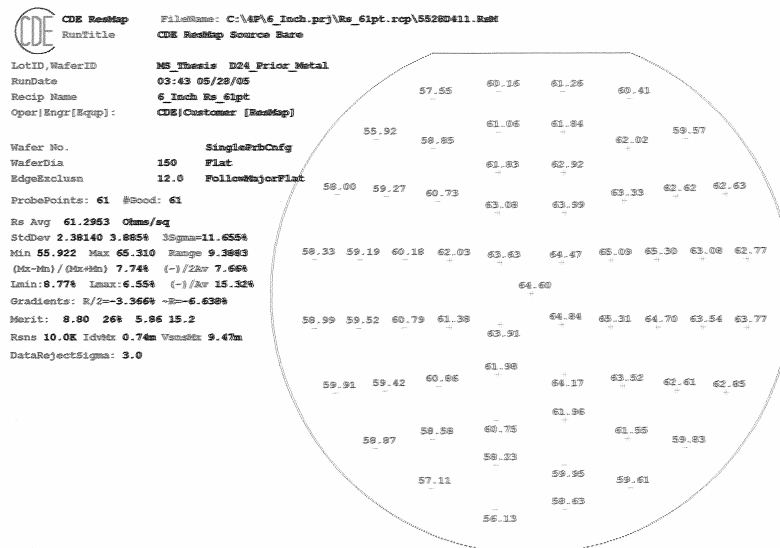


Fig. 4.1 – A sample sheet resistance map taken from a CDE Resmap system.

4.2 SPREADING RESISTANCE PROFILING

Spreading Resistance Profiling (SRP) is an analysis technique that can be used to determine the doping concentration as a function of depth into the wafer. It functions by using two probes to measure resistance similar in some ways to the four point probe technique. However, the sample is beveled to allow for resistivity measurements as a function of depth into the sample, and the probe spacing is much smaller, typically less than twenty microns. The angle must be kept shallow to provide sensitivity in the angstrom regime. The samples measured for spreading resistance for this study had bevel angles ranging from 0.00143 to 0.0038 degrees. Preparing the sample can be quite difficult, since the angular cut must be precise and uniform. The beveling process must

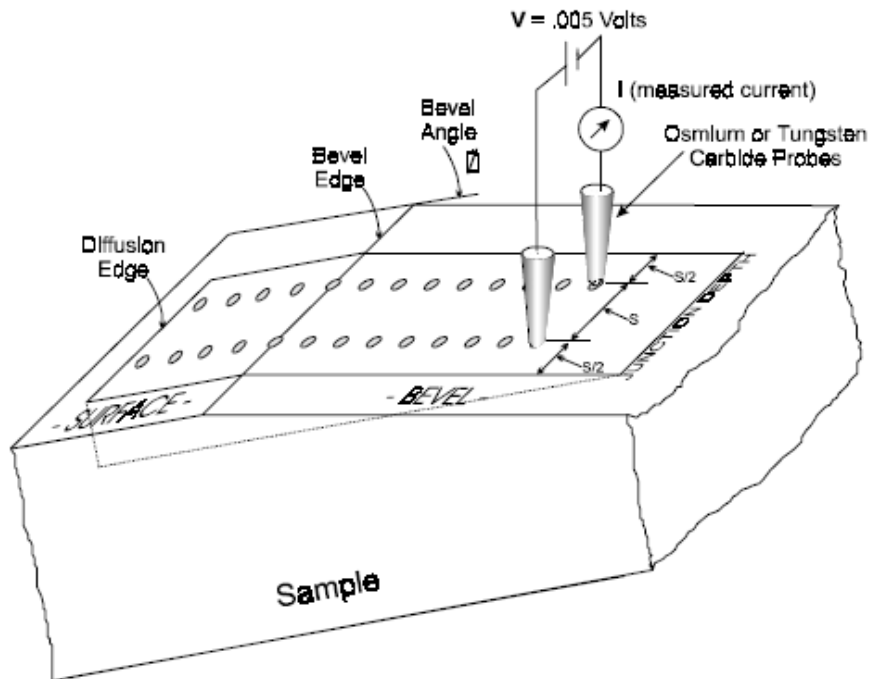


Fig. 4.2 – SRP measurement setup, from [16].

be completely mechanical so as not to introduce additional charge in the material to be studied. The measured resistance from the probes, R_m is a sum of several types of resistance and is given by the equation below,

$$R_m = R_c + SR + R_{bulk} \quad 4.3$$

Where R_c is the probe contact resistance, SR is the spreading resistance which is the desired parameter to be measured, and R_{bulk} is the semiconductor bulk resistance [15]. The bulk resistance is assumed to be negligible in most cases. The contact resistance becomes an offset in the measurement that requires frequent calibrations against samples with known resistivity to remove. This measurement is repeated across the sample, giving a concentration profile at regular depth intervals. This technique is destructive to the sample since the wafer must be beveled for the measurements to take place, limiting the uses of SRP. In a semi-infinite homogeneous layer, the spreading resistance due to the current restriction is given by,

$$SR = \frac{\rho}{2a} C.F. \quad 4.4$$

Where ρ is the resistivity of the sample, a is the circular radius of the probe known from the calibration procedure, and C.F. is the correction factor if the sample is not semi-infinite and homogeneous [15]. The resistivity of the sample can be measured and used to determine the doping concentration by using a known mobility as shown in equation 4.5.

$$\rho = \frac{1}{q \cdot (\mu_n \cdot n + \mu_p \cdot p)} \quad 4.5$$

Since the mobility must be known or assumed to determine doping concentration, the technique is of limited use on its own in the context of this study. The amorphization

process will affect the sample mobility and without a mobility measurement, it cannot be confirmed whether the annealing process restores bulk crystalline mobility in the silicon. However, this uncertainty in the concentration calculations does not change the measured resistivity. By integrating the resistivity over the depth of the implanted profile, a sheet resistance can be obtained. This sheet resistance is compared with the measured four-point probe sheet resistance to determine the accuracy of the measurement. Likewise, the doping concentration can be integrated over the implant depth to determine the active dose directly rather than rely on simulations like a simple sheet resistance measurement. The integration of doping concentration and resistivity can be prone to error due to an effect that causes the SRP to under-estimate the junction [17]. This effect is due to the bevel created for the SRP measurement, as the electrical field rotates when the surface angle is modified. This causes the electrical junction between carriers to change position. While this effect measures a reduced junction depth, the integration of the profile to determine active dose is only marginally effected, as the regions of highest concentration have a greater impact upon the integration. However, an attempt to counteract this effect was done; several samples were sent without p-n junctions. Raw data from SRP scans can be found in Appendix D. The analysis was done at Solecon Labs.

4.3 HALL EFFECT

The Hall Effect takes advantage of magnetic field influence over charged carriers to determine the mobility and carrier density of a material. Fig. 4.3 shows the Hall Effect for an arbitrary material. A current is applied to a sample in the x-direction, with a perpendicular magnetic field present in the z-direction. The charge carriers react in the

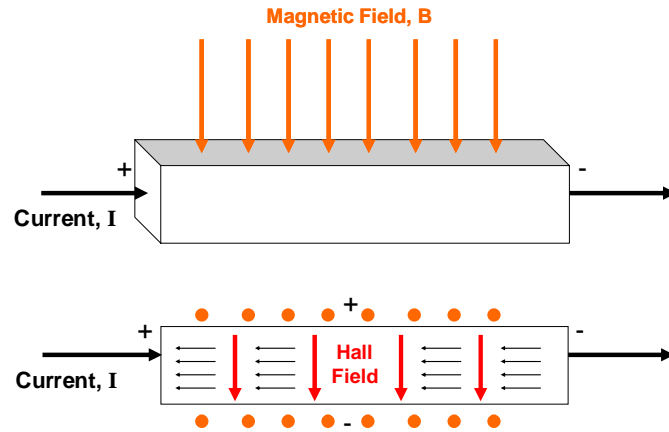


Fig. 4.3 – The Hall Effect.

presence of the field, causing a field to be created in the y-direction. This field can be measured in the form of a voltage and used to determine the Hall coefficient, R_H . The equation for this is shown below,

$$R_H = \frac{V_H \cdot t}{I \cdot B_{\perp}} \quad 4.6$$

Where V_H is the measured Hall voltage, t is the thickness of the material along the z-axis, I is the applied current, and B_{\perp} is the applied magnetic field [18]. The Hall coefficient is related to the carrier concentration by the following equation,

$$R_H = \text{sign}(e) \frac{1}{qn} \quad 4.7$$

Where q is the carrier charge, $\text{sign}(e)$ is the sign of the majority carrier and n is the carrier concentration [8]. If the majority carrier is electrons the Hall coefficient is negative and it is positive if the majority carrier is holes. This alone makes a Hall measurement a useful technique since the type of carrier can be determined. Equation 4.7 is a simplified approximation for the carrier concentration. It assumes a high concentration of carriers, no compensated doping, and an infinite block of material. The carrier mobility can also

be determined for a given sample by taking the ratio of the Hall coefficient to the resistivity of the sample.

Hall measurements will not be used in this study for several reasons. The first is that while the measurement can extract a doping concentration and mobility, neither of these values give any indication of the depth of the profile, or the shape. Therefore, they only represent an average value; no information is given about concentration or mobility versus the depth into the sample. The second reason is that the measurement can be highly inaccurate due to the dependence on the geometry of the sample. The equations shown above are only of value for a rectangular sample biased at both ends.

4.4 CAPACITANCE ANALYSIS

Capacitance analysis is a useful electrical characterization technique for determining doping of a semiconductor. It is performed by using a metal-oxide-semiconductor (MOS) structure. This structure is illustrated in Fig. 4.4. The testing of a MOS capacitor is done by sweeping the voltage across the capacitor and examining the how the capacitance changes. There are two basic regions of operation in a MOS structure, accumulation and depletion. Accumulation is where the charge applied on the metal gate is the opposite of the charge of the majority carriers in the device, that is a negative charge for a p-type wafer and a positive charge for an n-type wafer. The charge will cause the carriers in the substrate to be attracted to the surface of the device. In this case all the voltage applied to the MOS is across the oxide. Therefore, the capacitance in this mode of operation is only the capacitance of the oxide insulator, C_{ox} . The other region is depletion. This is where the charge on the metal gate is the same as the charge of the majority carrier in the substrate. This charge will repel the majority carriers and

attract the minority carriers. This sets up depletion region at the surface of the semiconductor. Since voltage is dropped across the depletion region, there will be some capacitance associated with the depleted region, C_s . If enough voltage is applied to the MOS structure, the semiconductor enters what is known as inversion. Inversion is where the number of minority carriers attracted to the surface exceeds the number of majority carriers left at the surface. Once inversion is reached, the theoretical capacitance will not change.

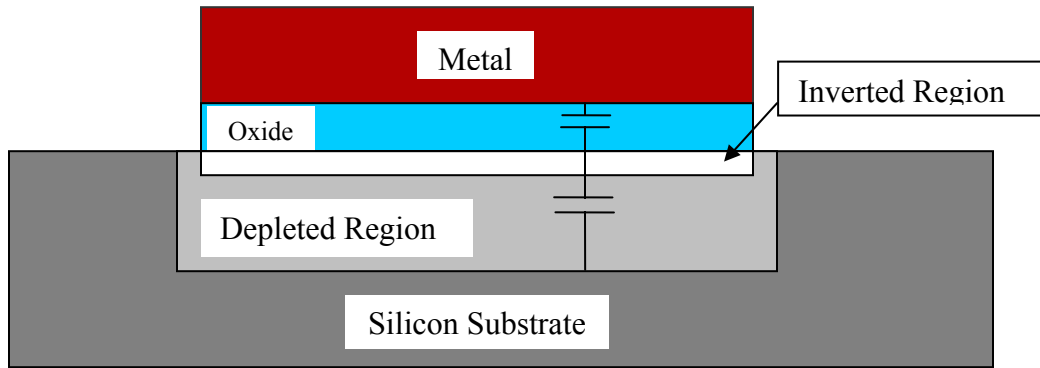


Fig. 4.4 – MOS capacitor under bias.

4.5 X-RAY DIFFRACTION

X-ray Diffraction (XRD) is an analysis technique used to determine morphology properties of a material. It is used to explore the structure of randomly orientated crystalline materials. By striking a thin layer of material with x-rays and measuring the resulting diffraction pattern, important information about the material structure can be obtained. The XRD for this experiment was done at Bruker AXS on a D8 thin-film in-plane diffractometer.

The x-rays diffract according to Bragg's Law, which predicts the angle of diffraction, θ , based on the wavelength λ , and the lattice spacing, d .

$$n\lambda = 2d \sin \theta$$

4.8

The intensity of the scattered x-rays is measured as a function of twice the incident angle. The diffraction pattern can give information about the crystal structure [19]. The breadth of the peak contains information about the grain size and micro-strain within the material. Micro-strain refers to a strain that is not uniformly distributed through the material. This can be induced by a bending stress or by defects within the material that can create regions of varying strain. The difficulty with quantifying this strain is that it can be coupled with the broadening of the intensity peaks due to changes in grain size. Single-crystal silicon does not contain grains, therefore this difficulty is not present. The converse of this is macro-strain, or a uniform strain through the material. Macro-strain is observed from a shift of the diffraction peak.

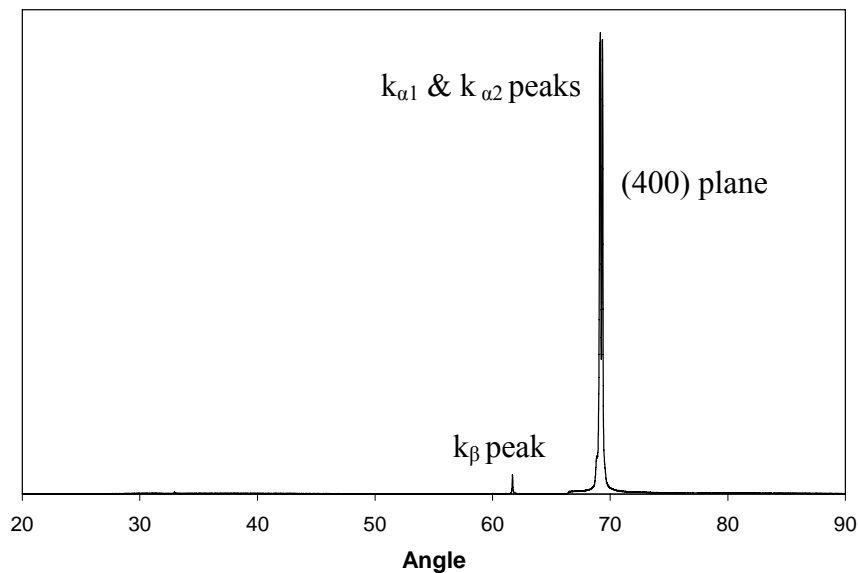


Fig. 4.5 – X-ray diffraction pattern for a silicon wafer. Only a single peak should be present due to the crystalline nature of the sample. The labeled peaks refer to the different wavelengths in the copper x-ray source.

4.6 TRANSMISSION ELECTRON MICROSCOPY

The use of electrons to image through a material is the analysis technique known as Transmission Electron Microscopy (TEM). A TEM system functions by measuring the effect of a highly energetic, on the order of 100-1,000 keV, beam of electrons that passes through the sample. The type of collision the electron beam undergoes demonstrates information about the material structure; elastic collisions can diffract the electrons, while inelastic collisions give information about grain boundaries, dislocations and defects in the material. Bright-field and dark-field imaging is possible, as well as observing diffraction patterns, by changing the optics of the beam path [20]. The depth of material that the electron beam can penetrate is determined by the acceleration voltage used. A major difficulty of this technique is creating a sample thin enough for the beam to penetrate. For this investigation, the TEM analysis was done at Corning Glass on a JEOL JEM-2000FX system.

4.7 SECONDARY ION MASS SPECTROSCOPY

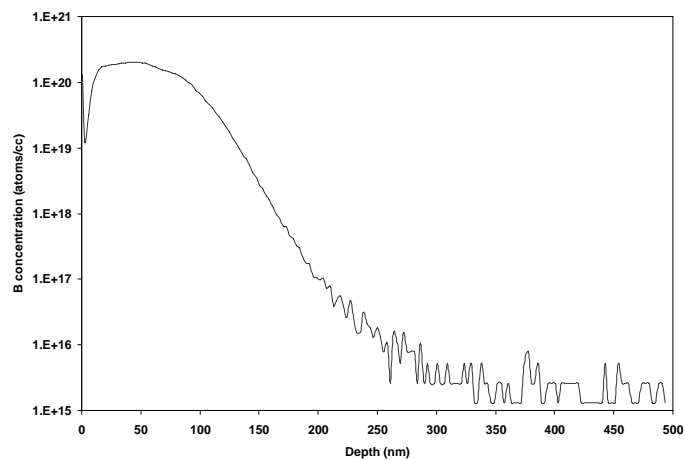


Fig. 4.6 – Sample SIMS scan for a boron implant. Notice that below $1 \times 10^{16} \text{cm}^{-3}$ concentration, the noise in the signal begins to increase.

Secondary Ion Mass Spectroscopy (SIMS) is a technique used to measure impurity concentration in a material. The SIMS analysis for this investigation was done at Corning Glass. A beam of ions, referred to as the primary beam, is used to sputter off atoms in the sample. These atoms can become ionized and form the secondary ion beam. This beam is measured by mass-to-charge spectrometry [21]. The source of the primary beam can determine the sensitivity and effectiveness of the process. For electropositive material, an oxygen beam is used; for electronegative material, the source is cesium [2]. In terms of measuring dopant concentration, boron requires an oxygen beam, while phosphorus is measured by a cesium beam. By measuring the ion emission as a function of sputter time, concentration versus depth can be determined [2]. SIMS analysis can be used to determine impurity concentration due to the ability to measure small concentrations of ions. It should be noted that calibration is required to determine true concentration levels from the intensity signal measurement.

Fig. 4.6 shows an example SIMS scan for an implanted wafer. The sharp decrease in concentration at the surface is not real; it is an artifact of the measurement and due to the inaccuracy of the ion beam at the very surface of the sample. This method measures both active and inactive impurities; therefore it is necessary to combine this technique with another measurement, such as SPR, to determine the amount of activation in a doped semiconductor. This technique is destructive to the sample, making it only useful for some analysis.

Chapter 5 Donor Activation

5.1 PHOSPHORUS ACTIVATION

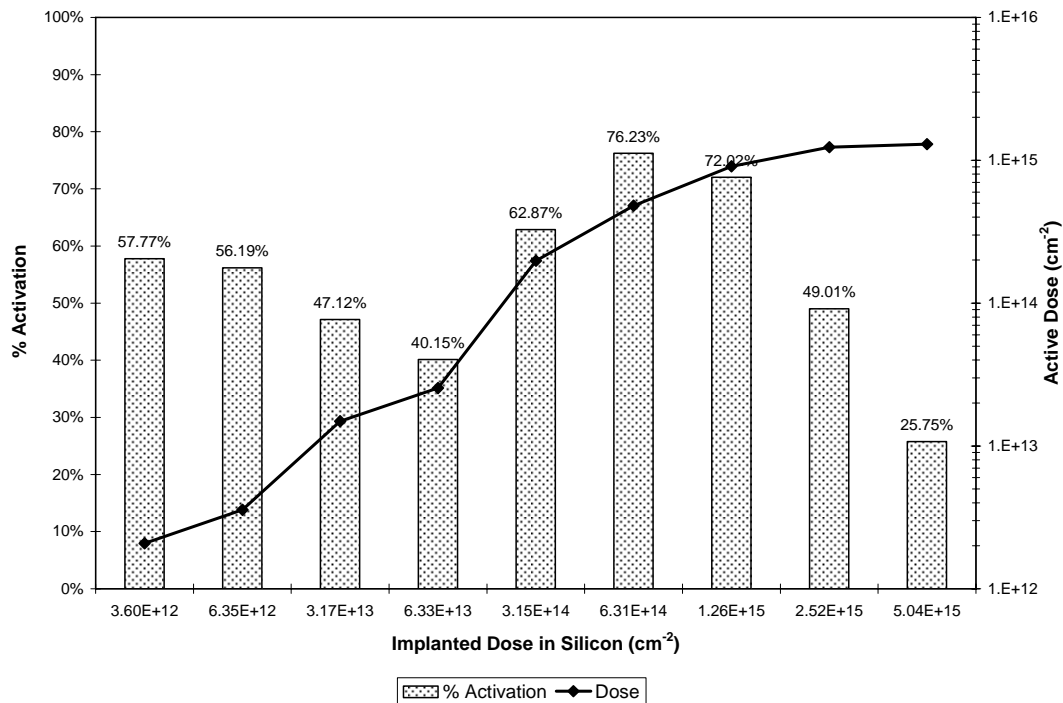


Fig. 5.1 – Percentage of phosphorus activation for a range of implanted doses. The x-axis is the amount of dose that is within the silicon. This axis is not scaled.

The most accurate method to quantify activation would be taking the ratio of the integrated active profile (SRP) to the integrated total dopant profile (SIMS). This ratio is referred to as the percent activation, and is the primary metric used in this investigation. However, it is not feasible to have SRP and SIMS data for each sample measured; therefore, the amount of active dose is modeled by means of SUPREM. In addition, even an SRP/SIMS ratio can yield unreasonable results under certain conditions (see section

5.4). A sheet resistance measurement, taken over the average of sixty-one data points, is matched with a SUPREM profile to determine the effective active dose. The simulation software assumes a scaled implant profile as stated in section 2.5. It is important to point out that both the simulated active dose and the integrated active dose from SRP data assume there is no mobility degradation due to defects in the silicon.

The investigation of phosphorus activation at 600°C was done for a wide range of implanted doses. The implanted doses range from 5×10^{12} to $8 \times 10^{15} \text{cm}^{-2}$, in order to capture the complete picture for most valid doses. Fig. 5.1 shows the initial results for activating phosphorus implants. The annealing was done in the furnace for one hour; this anneal was chosen to ensure equilibrium activation was reached for at 600°C.

The implant was done through 100nm screen oxide; this oxide causes a dopant loss of forty percent when removed. The x-axis represents the amount of the implant dose that remains within the silicon, according to simulation and SIMS analysis. It should be noted that the x-axis is not scaled in this chart. The data shows the dependence of activation on the implant damage, as in the mid-range of doses shows an upward trend with the amount of activation. A dose of $1 \times 10^{14} \text{cm}^{-2}$ is not enough to amorphize the silicon, therefore this point exhibits a low point in activation, however after this point, self-amorphization begins, allowing for more dopant to be incorporated into the lattice and giving much higher levels of activation, up to a peak of 76% at $1 \times 10^{15} \text{cm}^{-2}$. Beyond this dose, a limitation to the active dose is observed. The limitation will be referred to as an active dose saturation. The dose contains information about both active concentration and junction depth; both of these can affect the sheet resistance and therefore the active dose. However, neither of these is quantified for all samples, therefore, the saturation

must be associated with an active dose and not the more commonly used concentration solubility limit. The limit is $1.3 \times 10^{15} \text{ cm}^{-2}$; even with twice the dose implanted, the $5 \times 10^{15} \text{ cm}^{-2}$ data point does not provide any additional contribution to the activation or sheet resistance. Additional SRP data on this treatment combination could illuminate this effect, however it was not acquired. This plot shows that phosphorus is capable of self-amorphizing at high implant doses and this self-amorphization provides enough damage to allow activation to occur at significant levels.

5.2 ANNEALING PHOSPHORUS

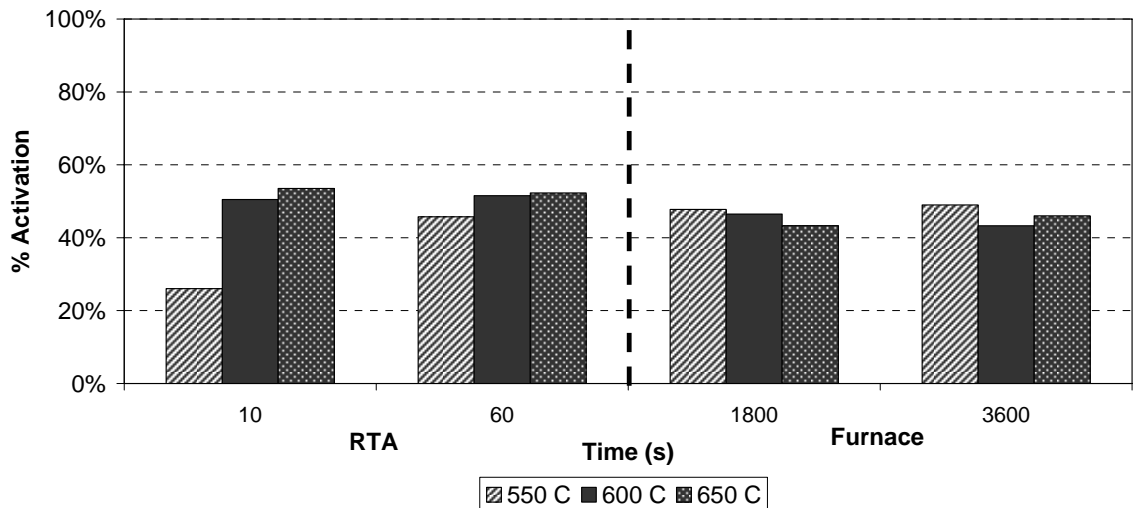


Fig. 5.2 – Phosphorus annealing experiment. Two anneal times per anneal type and 3 temperatures: 550, 600, and 650°C.

The annealing of phosphorus is the next concern; therefore, an experiment was done to determine the optimal annealing conditions. The implanted dose for this experiment was $4 \times 10^{15} \text{ cm}^{-2}$, sufficiently high to ensure full amorphization, so as not to further complicate the experiment. The annealing was broken into two categories, furnace and rapid thermal. The rapid thermal was done for ten seconds and one minute,

while the furnace anneal was done at thirty minutes or one hour. Three different temperatures were used in all cases, 550°C, 600°C, and 650°C to determine the affect of temperature variation on the activation. The results are shown in Fig. 5.2. The resulting data shows little variation between the annealing conditions, with one notable exception, the 550°C, ten second anneal. Activation was cut in half for this point, relative to the other data at 550°C. This suggests that at sufficiently low temperatures and short times, the dopant does not have enough energy to reach equilibrium activation, however if either condition is met, equilibrium can be reached. All of the thermal anneal data does not indicate any difference between anneal temperatures, which means that the anneal time of one minute in RTA is all that is necessary to reach equilibrium activation in this case.

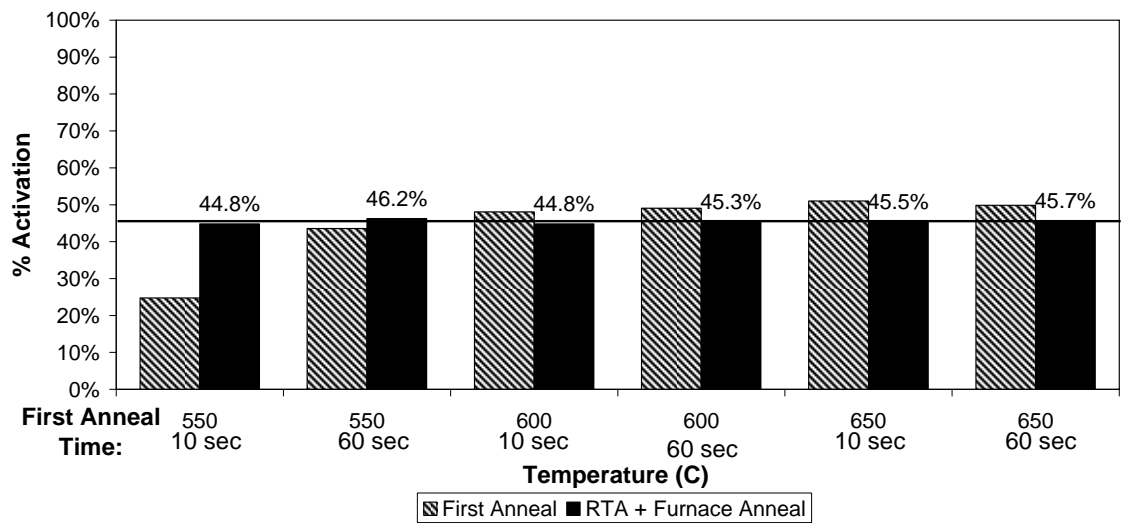


Fig. 5.3– The effect of a second furnace anneal on rapid thermal samples. The phosphorus dose is $4 \times 10^{15} \text{ cm}^{-2}$.

This experiment does not rule out an implant dose interaction with the temperature or the anneal time. Since the anneal time is more significant in this case, and due to the limitations in anneal temperature imposed by the applications, the next step was to determine whether the variations in the RTA processing could be removed by a subsequent furnace anneal. Fig. 5.3 shows how a second furnace-anneal alters the

amount of activation. The furnace anneal brings the dopants to an equilibrium position, regardless of whether more or less was previously activated. This equilibrium level, for a $4 \times 10^{15} \text{ cm}^{-2}$ dose, is 45%. To determine whether furnace and rapid thermal annealing provide equivalent levels of activation for a wide range of doses, the experiment shown in Fig. 5.4 was performed. The furnace anneal was performed for one hour, while the RTA was done at two minutes. The rapid thermal anneal was followed by the standard one hour furnace anneal.

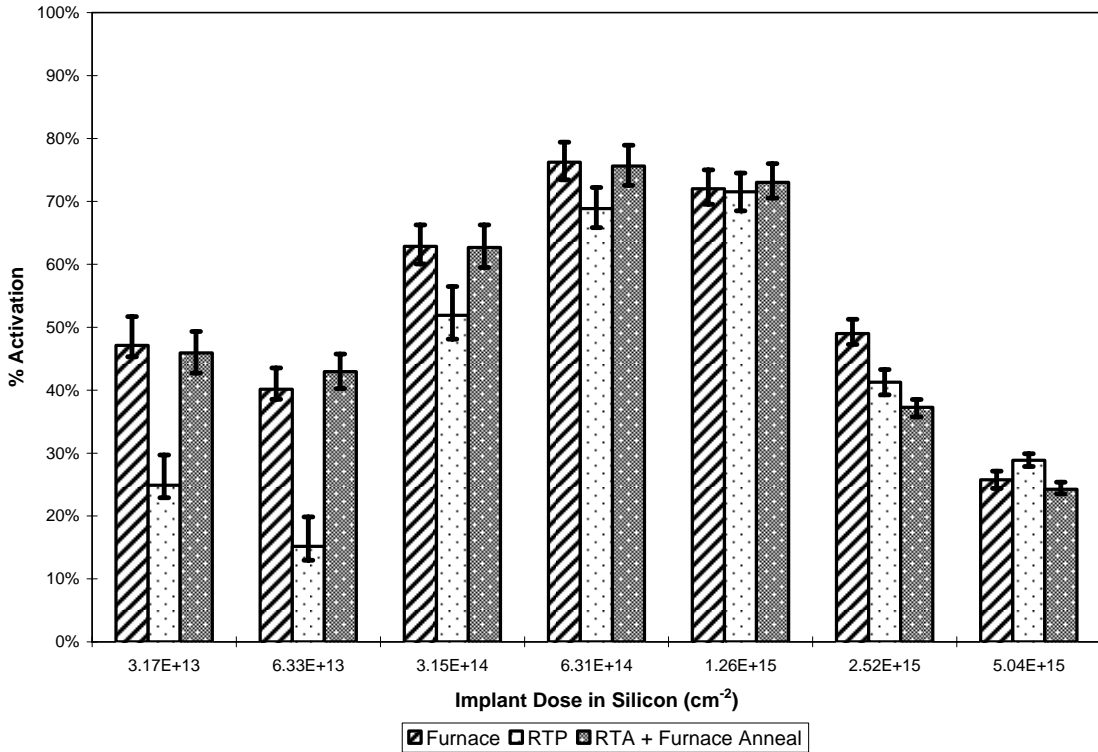


Fig. 5.4– Phosphorus activation for different anneal conditions: 1 hour furnace annealing, 2 minute RTA followed by a 1 hour furnace anneal.

The low doses show a large difference between RTA and furnace activation, however this difference lessens as the boron dose increases, until the RTA provides a higher amount of activation at $8 \times 10^{15} \text{ cm}^{-2}$. This shows that the rapid thermal process is not as susceptible to the dose saturation as the furnace annealing. Given enough time, the

dopants can de-activate, as shown in Fig. 5.3. This is only a concern at the higher phosphorus doses, since this is the only place where there is enough dopant to reach the equilibrium saturation level. It is apparent that there is an anneal time-dose interaction, since lower phosphorus doses require more time in order to reach the same level of activation. However, after the second furnace anneal, this dopant can become active.

5.3 X-RAY DIFFRACTION ANALYSIS

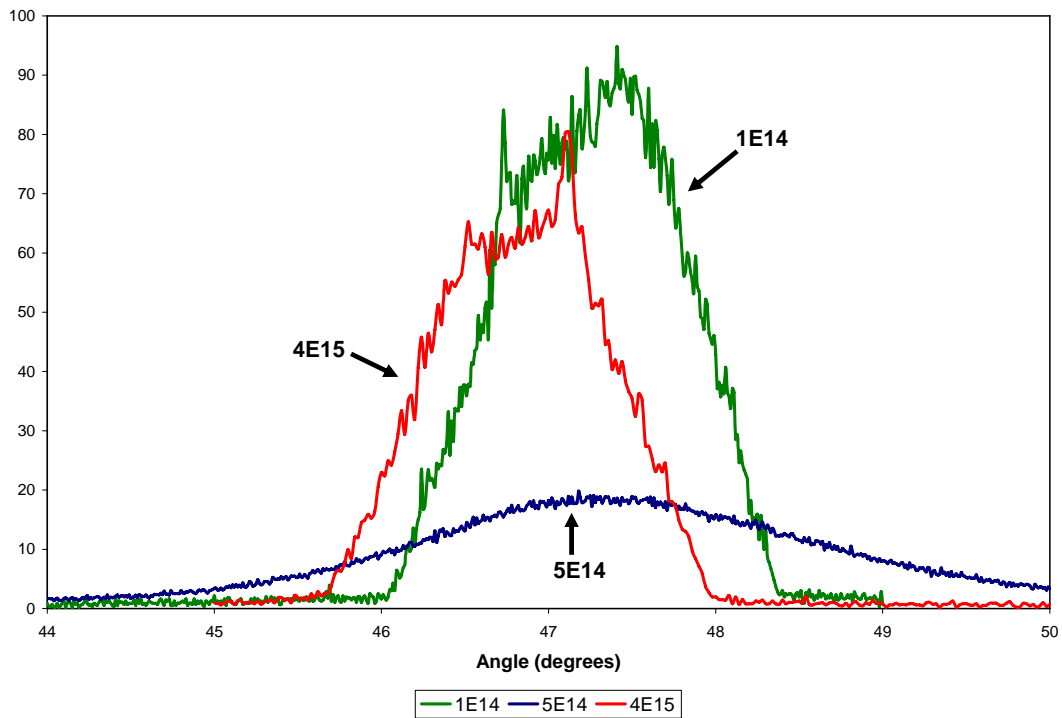


Fig. 5.5 – XRD for 1×10^{14} and $4 \times 10^{15} \text{ cm}^{-2}$ implanted phosphorus doses annealed for one hour at 600°C . A phosphorus implant of $5 \times 10^{14} \text{ cm}^{-2}$ was done without an anneal.

X-ray diffraction was done on several phosphorus samples in order to determine whether there was an impact on crystallinity and defects due to the implant. The implanted doses were $1 \times 10^{14} \text{ cm}^{-2}$, a dose unlikely to amorphize the silicon; a $5 \times 10^{14} \text{ cm}^{-2}$ dose without an anneal to determine how the phosphorus damages the silicon; and

$4 \times 10^{15} \text{cm}^{-2}$, a dose that will completely amorphize the surface. The samples were analyzed at Bruker AXS on a D8 thin-film in-plane diffractometer. The thin film in-plane x-ray diffraction option was required, since the implanted region is thin enough that conventional XRD penetrates too far inside the sample. The observed peak for these scans corresponds to the (220) plane as analyzed by Bragg's Law (equation 4.8).

The measurements do not show any information about crystallinity of the samples; if the material was poly-crystalline in nature, several peaks would be present. This is not observed, therefore the only information that can be obtained is micro-strain. By comparing the breadth of the peaks from one sample to another, some information can be discerned. The method to determine the breadth, or width of the peak, is full-width-half-max (FWHM), where the width of the peak is measured at half of the maximum. This allows for a normalization of the data for each sample. For the $1 \times 10^{14} \text{cm}^{-2}$ sample, the breadth is 1.36° , and for the $4 \times 10^{15} \text{cm}^{-2}$, the breadth is 1.22° . The breadth for the $5 \times 10^{14} \text{cm}^{-2}$ is 2.69° , much higher than either annealed sample. Therefore, without the anneal, a great deal more micro-strain is evident. This strain can be correlated to defects within the silicon.

5.4 PHOSPHORUS PROFILING

Sheet resistance is not a complete description of an implant, therefore, SRP and SIMS data was collected for several data points. SRP was done on phosphorus doses of 1×10^{14} , 1×10^{15} , and $4 \times 10^{15} \text{cm}^{-2}$. SIMS was performed on phosphorus doses of 1×10^{14} and $4 \times 10^{15} \text{cm}^{-2}$. SRP was carried out by Solecon Laboratories and SIMS was performed at Corning Inc. The annealing conditions for both SIMS and SRP were one hour in the furnace at a temperature of 600°C . These phosphorus doses were chosen to represent the

data because they demonstrate useful characteristics. The $1 \times 10^{15} \text{cm}^{-2}$ dose represents the highest level of activation, while the $1 \times 10^{14} \text{cm}^{-2}$ represents the lowest percentage of activation. The $4 \times 10^{15} \text{cm}^{-2}$ is the point at which the active dose saturates. Fig. 5.6 shows the three SRP plots superimposed with the SUPREM models used to predict the

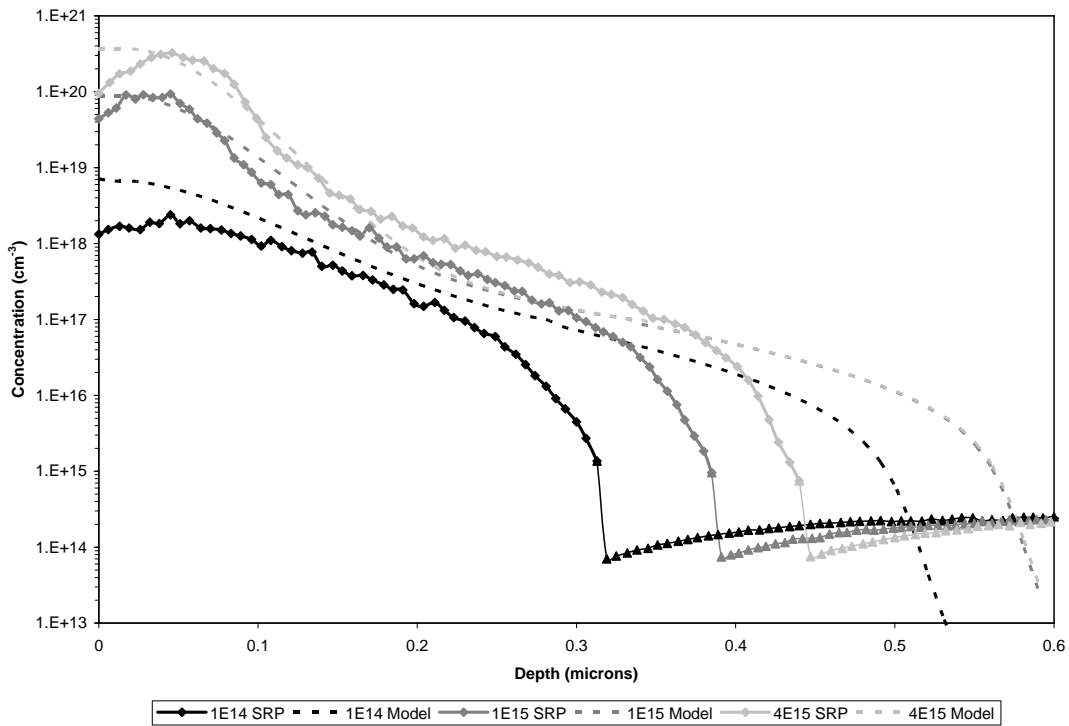


Fig. 5.6 – SRP for phosphorus implant doses of 1×10^{14} , 1×10^{15} , and $4 \times 10^{15} \text{cm}^{-2}$ superimposed with SUPREM implant models (dotted lines).

activation from the sheet resistance data. The active junction depths range from 300nm to 450nm. This junction depth is less than the simulated depth, however since the concentration is relatively low, this has little impact on the integrated dose. This discrepancy may be partially due to the interpretation of the electrical junction depth by SRP as noted in section 4.2. Fig. 5.7 and Fig. 5.8 show the SIMS and SRP data, once again superimposed with the SUPREM model. For the $1 \times 10^{14} \text{cm}^{-2}$ implant, a clipping effect can be seen with the activation profile. A concentration of $2 \times 10^{18} \text{cm}^{-3}$ is the saturation limit for this dose. At doses above $1 \times 10^{14} \text{cm}^{-2}$ this saturation is not observed,

however, this is due to the self-amorphization that occurs at higher doses, and is not present in this case. The amount of inactive dopant above this saturation corresponds to about 60% of the implanted ions, and by performing a numerical integration on these profiles; an activation of 40% is calculated. This corresponds well with the 44% activation predicted from sheet resistance measurements.

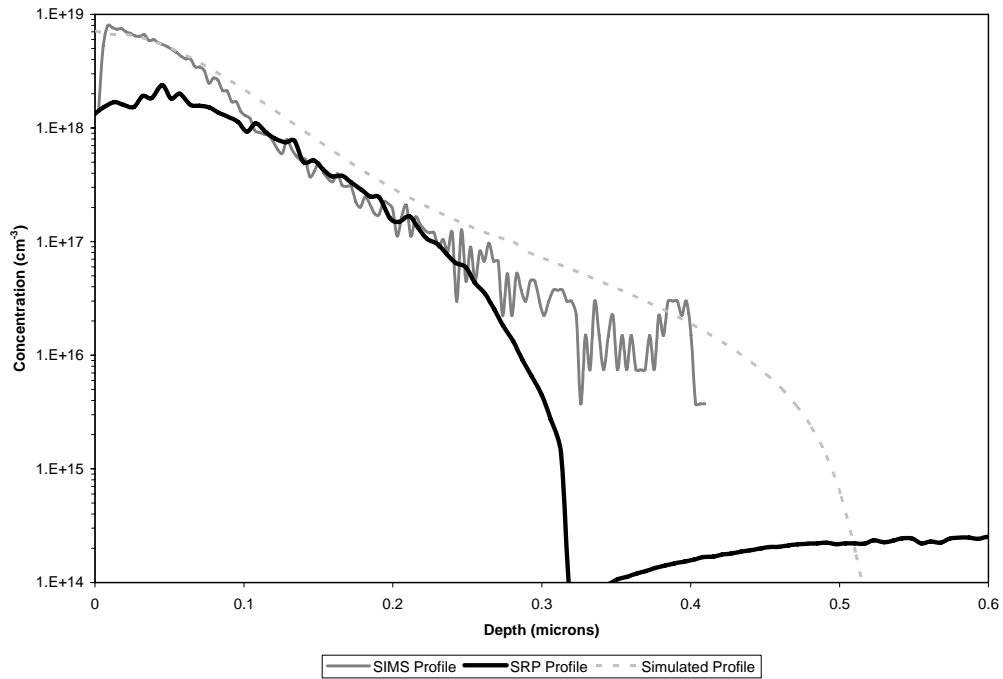


Fig. 5.7 – SIMS and spreading resistance profiles for $1 \times 10^{14} \text{ cm}^{-2}$ phosphorus implant, annealed at 600°C for 1 hour. SUPREM model included for reference.

The $4 \times 10^{15} \text{ cm}^{-2}$ implant does not have the similar clipped profile and due to the noise in the SIMS measurement at lower concentrations it is not possible to predict any depth dependence to the activation. Both the SRP and the SIMS match, however, the SIMS profile contains an anomaly. The profile is not rounded, but steadily decreasing in the high concentration region. Since this is a log scale, the actual effect this has on the difference between the SIMS and SRP is much more pronounced. The activation determined from this comparison of SIMS and SRP is 114%, notably impossible,

however much higher than the 50% interpreted by the sheet resistance. The unreasonable shape of the surface region of the SIMS profile could account for this difference.

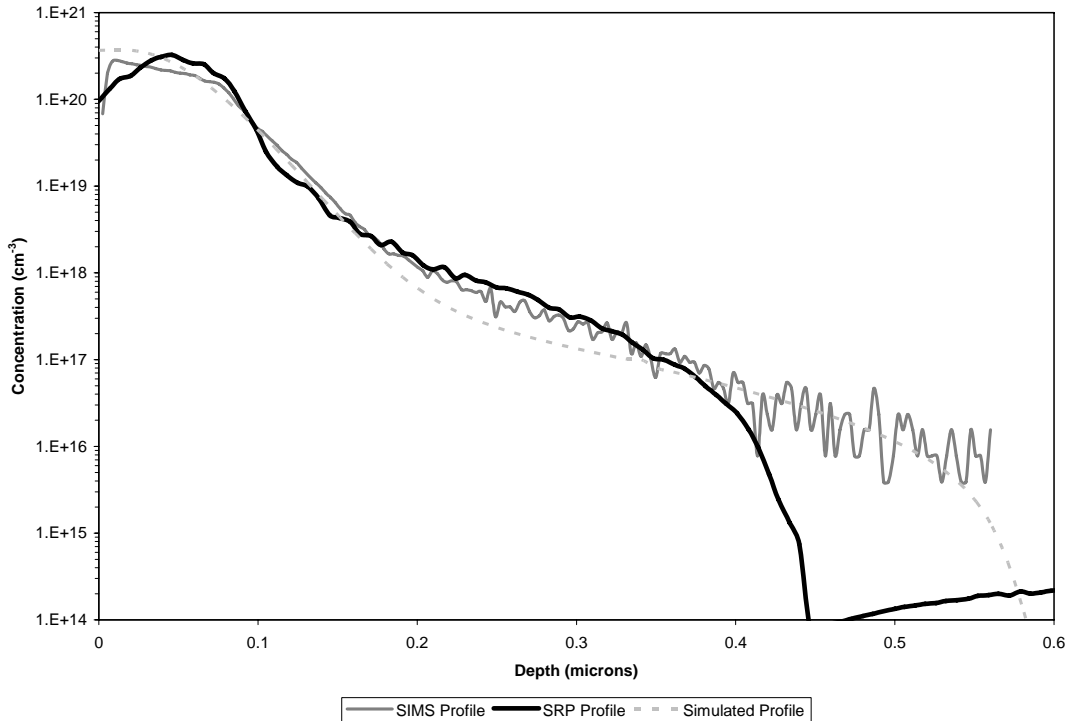


Fig. 5.8 – SIMS, model and spreading resistance profiles for $4 \times 10^{15} \text{cm}^{-2}$ phosphorus implant, annealed at 600°C for 1 hour.

5.5 ARSENIC ACTIVATION

Arsenic is an alternate dopant atom to phosphorus. It is typically used to create shallow n-type junctions as it has an atomic mass of 75, as opposed to phosphorus at 31amu. Arsenic also has a higher solid solubility limit when compared with phosphorus, since the atom matches better in the silicon lattice. Due to its higher mass it will create more implant damage per ion, requiring a lower dose to self-amorphize. It also diffuses less, which makes it ideal for shallow junction devices. A study of arsenic activation was

done to determine if the benefits of arsenic hold true at the 600°C temperature constraint. The arsenic implants were done at an energy of 120 keV through a 50nm screen oxide,

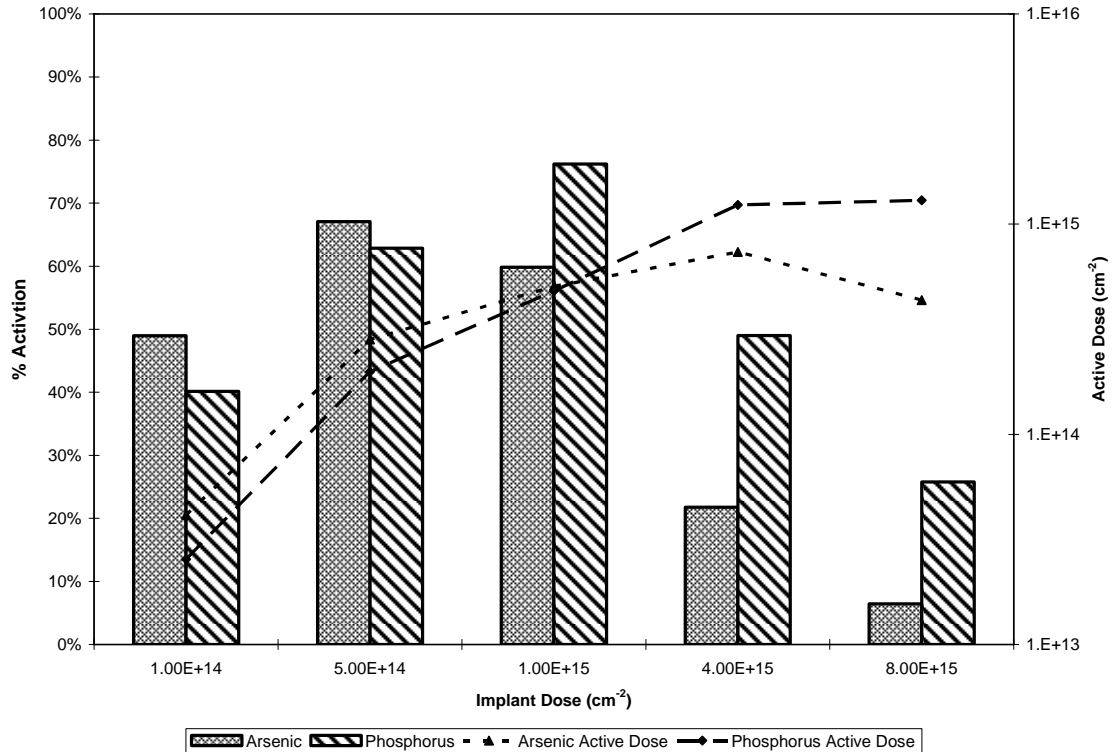


Fig. 5.9 – Arsenic percent activation as compared with relevant phosphorus data.

since arsenic has more mass, it requires more energy to reach a similar depth as phosphorus. Both rapid thermal and furnace annealing techniques were used to determine whether there was a difference in anneal time on the activation of arsenic as compared with phosphorus. A similar time dependence was found as in the phosphorus experiments; the rapid thermal anneals were not sufficient in activating lower doses of arsenic, however, at high doses, both anneals were equivalent. The interesting effect seen in this experiment is as the implanted dose increases passed $1 \times 10^{15} \text{cm}^{-2}$ the amount of dose that activates begins to decrease. This is not a saturation effect as seen with phosphorus, but instead there must be some mechanism that is removing available dopant

atoms from the pool of potential atoms. It is believed that the arsenic atoms are forming clusters, and at high doses the clusters become large enough to prevent most of the

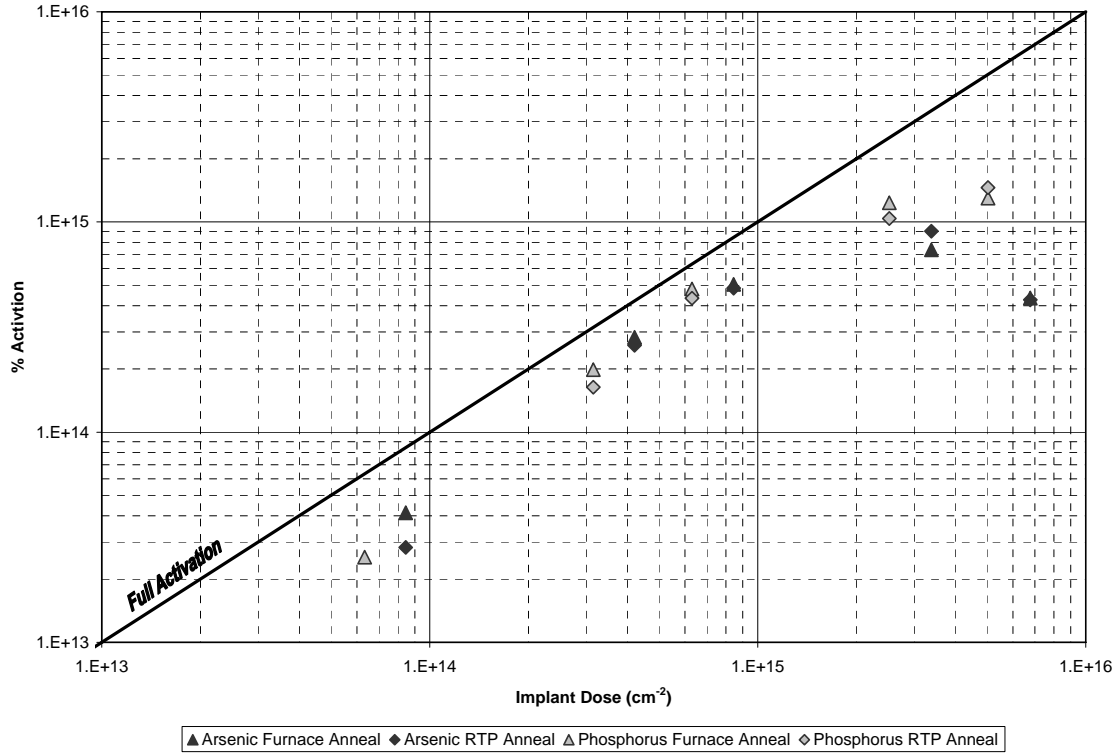


Fig. 5.10 – Arsenic active dose compared with phosphorus active dose for both furnace and RTA.

dopant from entering the lattice. Implanted arsenic clusters at a dose of $1 \times 10^{15} \text{ cm}^{-2}$ and this clustering becomes significant at higher doses [22]. A similar trend could be observed due to mobility degradation, which would also cause the sheet resistance to become higher for a given dose.

The clustering removes active dopant from available dopants [23]. For an implant dose of $8 \times 10^{15} \text{ cm}^{-2}$ the measured sheet resistance was similar to that of the $1 \times 10^{15} \text{ cm}^{-2}$ implant, while the measured sheet resistance for the $4 \times 10^{15} \text{ cm}^{-2}$ was lower, therefore putting eight times as many arsenic atoms into the silicon is less effective than putting only four times as many atoms into the silicon.

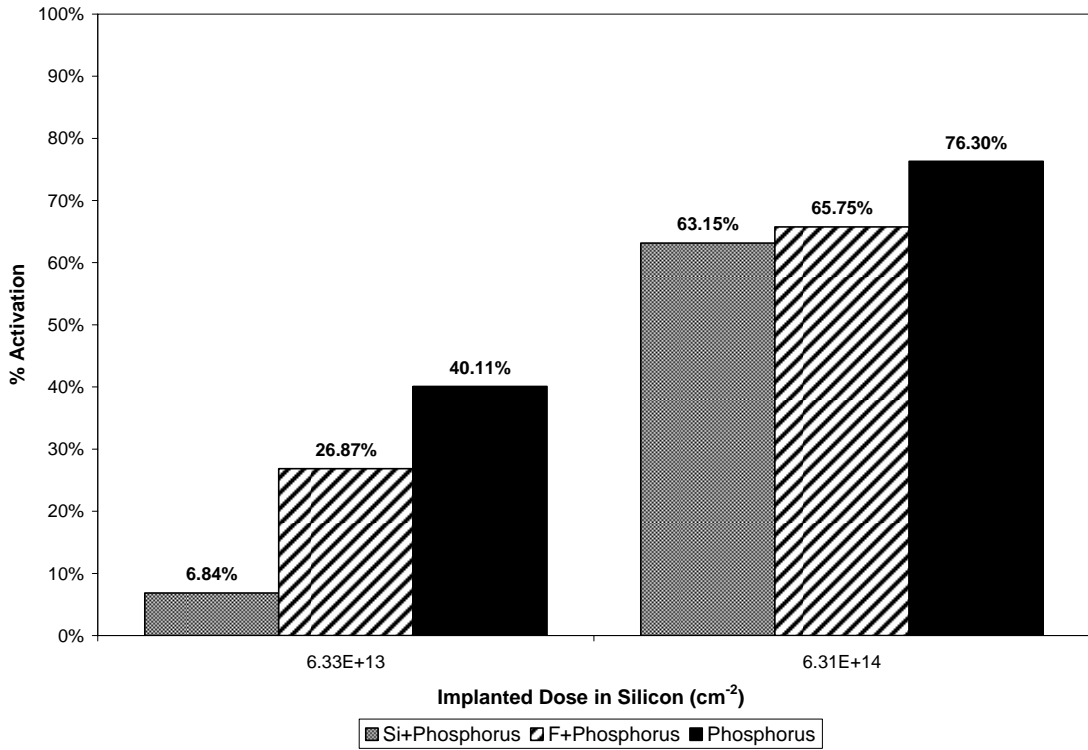


Fig. 5.11– Pre-amorphization implant for phosphorus, all samples furnace annealed for one hour.

5.6 PRE-AMORPHIZATION OF PHOSPHORUS

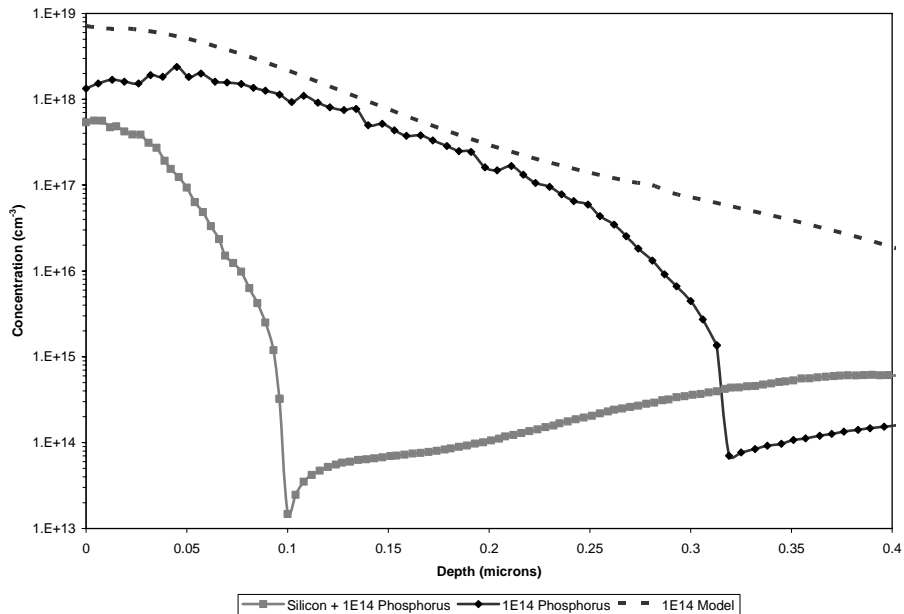


Fig. 5.12 – SRP of $1 \times 10^{14} \text{ cm}^{-2}$ phosphorus with and without a silicon pre-amorphization.

The increased activation of phosphorus due to self-amorphization leads to the next experiment, adding a pre-amorphization implant. Several atoms are available to cause implant damage to the silicon; for this experiment implanting fluorine and silicon were investigated. As Fig. 5.11 shows, the pre-amorphization causes a drastic increase in sheet resistance, and the corresponding decrease in modeled percentage of activation. Fluorine provides a higher level of activation than that of silicon, however, neither can match the activation of phosphorus on its own.

A spreading resistance profile was done to validate the very low levels of activation. Fig. 5.12 compares the active carrier profiles with and without a silicon pre-amorphization. The pre-amorphization drastically reduces the junction depth of the profile. Despite having a screen oxide in both cases, when the silicon is not amorphous, some ion channeling will occur. The pre-amorphization removes any form of channeling in the silicon lattice.

TEM analysis was done on the silicon pre-amorphized phosphorus sample, as shown in Fig. 5.13. The TEM was performed by Corning Glass on a JEOL JEM-2000FX system. Analyzing this micrograph shows that the defect-free region is only 27.8nm deep and a large region of defects exists beyond. The defective region extends to 83.3nm. This highly defective region explains how pre-amorphization impairs the activation of phosphorus. Although the phosphorus junction depth extends to 100nm, as shown in Fig. 5.12, the level of active dopant is much lower in all regions than without a pre-amorphization. The defects appear much larger in this case than with the fluorine pre-amorphization, suggesting that the extra silicon interstitials play a major role in the

formation of defects, at least when combined with phosphorus dopant. Not only is the junction reduced, but the active concentration level is reduced with the pre-

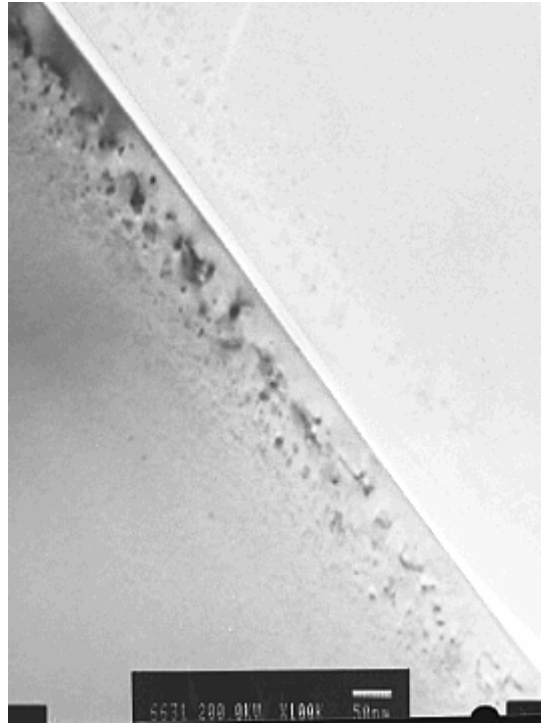


Fig. 5.13 – TEM micrograph of a phosphorus implant pre-amorphized by a silicon implant. Sample was annealed at 600°C for one hour.

amorphization. It is believed that this effect is due to the increased amount of interstitial atoms present. The silicon used to amorphize remains in the substrate and the phosphorus must compete with the silicon interstitials for vacant lattice sites. To study this further, SIMS was performed to examine if the distribution of phosphorus significantly changes. Fig. 5.14 shows the results and compares both SRP and SIMS profiles for phosphorus implants. The silicon pre-amorphization does not significantly change the phosphorus implant profile; however it does change the amount that activates. Therefore, it is true that the phosphorus remains within the substrate, but does not become electrically active below 0.1 microns when a silicon pre-amorphization is used.

SIMS measurements confirm the implanted dose to be correct, however, SRP predicts that only $2 \times 10^{12} \text{ cm}^{-2}$ dose becomes active.

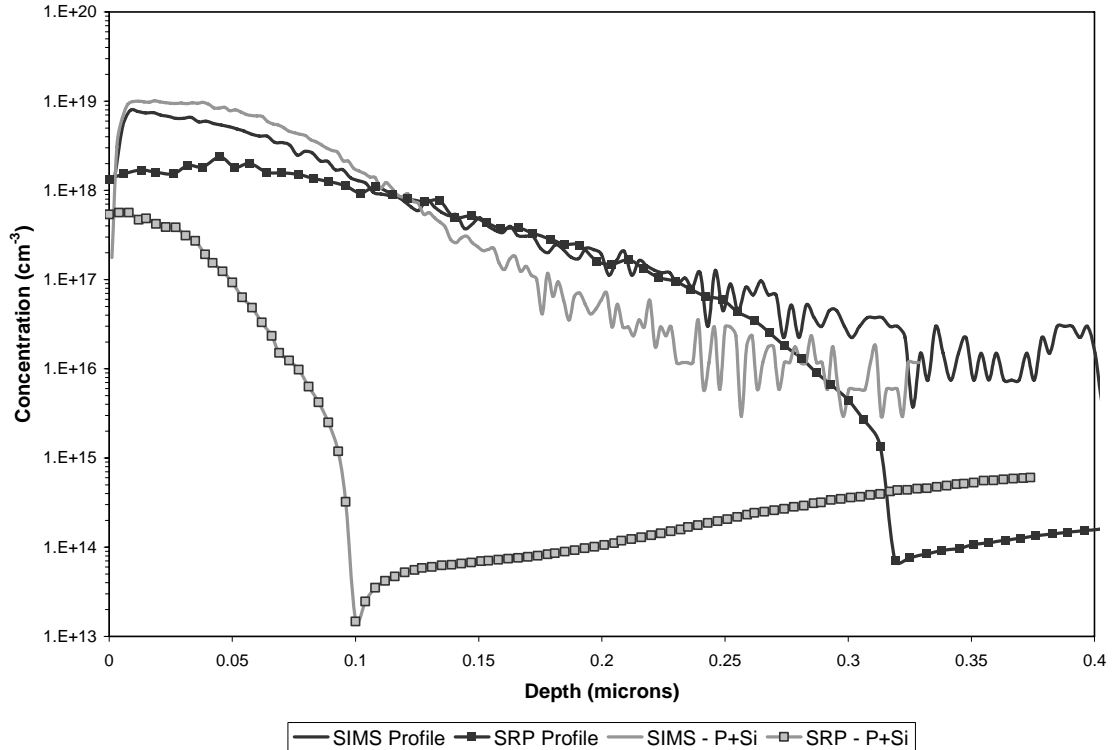


Fig. 5.14 – Phosphorus SIMS and SRP with and without a silicon pre-amorphization.

5.7 SUMMARY OF PHOSPHORUS AND ARSENIC

Phosphorus activation is a straight-forward process. The self-amorphization inherent in the process is sufficient to achieve high levels of activation at 600°C . The critical dose for to create a continuous amorphous layer is $5 \times 10^{14} \text{ cm}^{-2}$, and the in-plane XRD measurement confirms the disorder created by the implant. The XRD also demonstrated that the defects created by this self-amorphization can be removed by the anneal. RTA and furnace anneals indicate a dose dependence on the required anneal time to reach a steady-state level of activation. At high implant doses ($1 \times 10^{15} \text{ cm}^{-2}$ and greater) the time to reach this condition is short, on the order of one minute; low implant doses

(below $1 \times 10^{14} \text{cm}^{-2}$) require at least one hour of anneal to achieve steady-state activation. In addition to this dependence, the one hour furnace anneal provides an equilibrium level of activation, that can cause de-activation in some rapid thermal annealed samples.

Arsenic begins to self-amorphize at a lower dose than phosphorus, as expected due to the greater ion mass; however, at high concentrations of arsenic, the level of activation becomes very poor. This decrease in activation can be due to arsenic clustering, which prevents arsenic atoms from contributing to conduction. The activation of phosphorus is drastically reduced when a pre-amorphization implant is performed. Both fluorine and silicon implants were attempted to provide consistent damage regions for all phosphorus doses. The pre-amorphization process provided almost no activation with the $1 \times 10^{14} \text{cm}^{-2}$ phosphorus sample, and lower levels with the $1 \times 10^{15} \text{cm}^{-2}$ sample. It is postulated that the sample that self-amorphizes is less susceptible to a degradation in activation due to a pre-amorphization, as damage is already present. When the silicon pre-amorphization was performed for the $1 \times 10^{14} \text{cm}^{-2}$ phosphorus dose sample, the activation was reduced from forty percent to five percent. Therefore, a pre-amorphization process only hinders phosphorus activation, and should not be applied to any phosphorus implant at 600°C .

Chapter 6 Acceptor Activation

6.1 BORON ACTIVATION

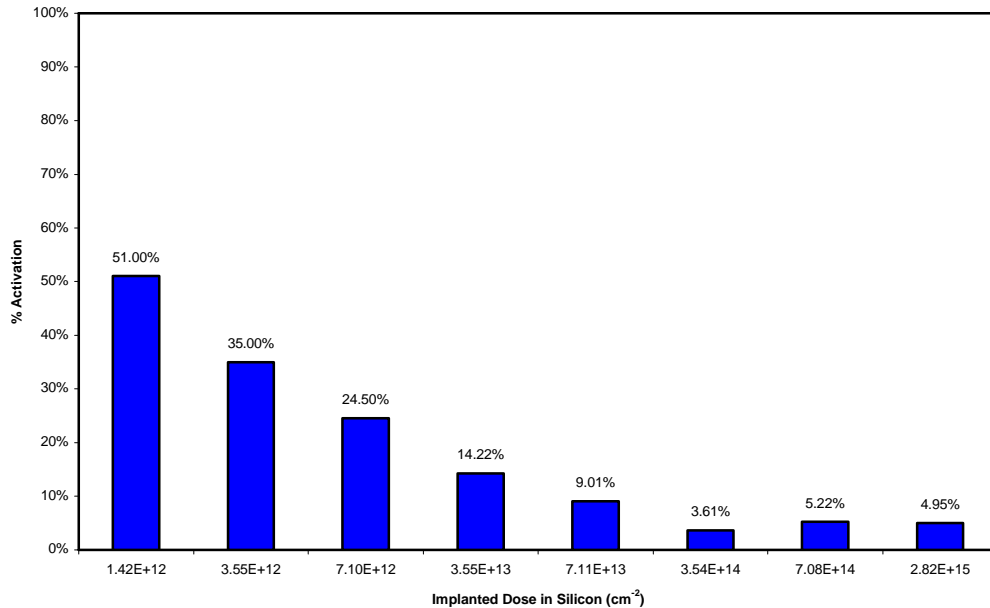


Fig. 6.1 – Boron percent activation for furnace annealing at 600°C for one hour.

Simply put, boron dopant does not activate well at 600°C. The anneal for the test, shown in Fig. 6.1, is 1 hour at 600°C. Low doses in the range of 2×10^{12} to $1 \times 10^{13} \text{cm}^{-2}$ appear to reach reasonable levels of activation. As the implanted dose increases, the amount of activation drops, until about 3-5% of the dose becomes active. Unlike phosphorus, in all cases no more than 50% of the dopant can be activated. This data matches the literature data shown in Fig. 2.2. Boron is not heavy enough to create vacancies that can aid activation, and the damage it does create is located only below the projected ion range (R_p). In order to activate high doses of boron, some pre-amorphization must be done. Low doses of boron can activate to reasonable levels

without relying on SPE. A pre-amorphization for a low dose implant makes little sense, since a low dose implant would most likely be used for threshold adjust implants in transistor processing; it is not desirable to amorphize the channel region of the transistor.

6.2 PRE-AMORPHIZATION

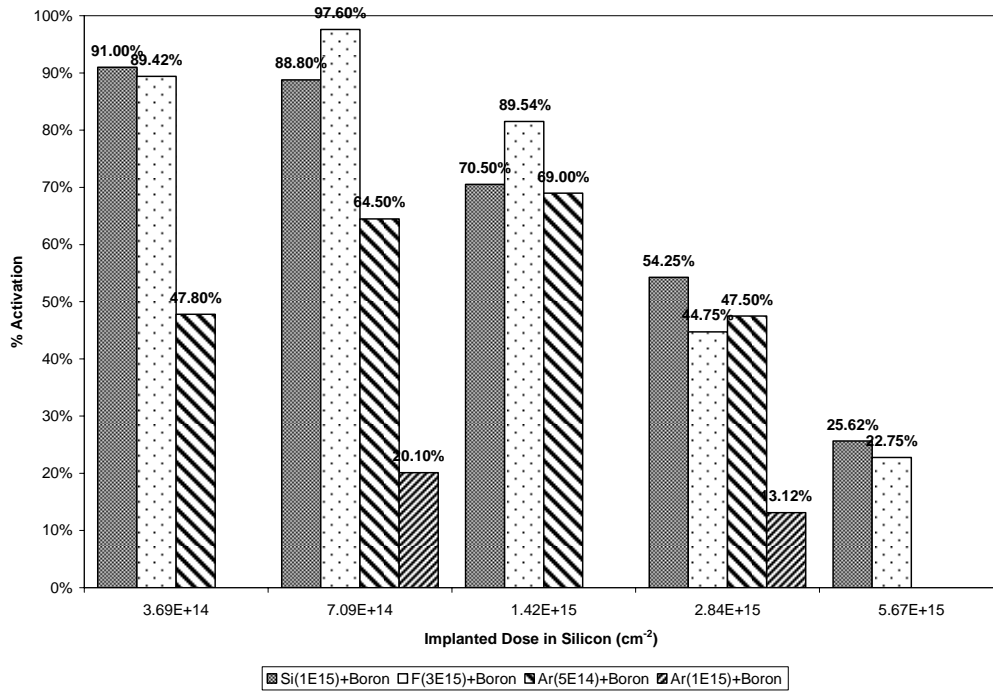


Fig. 6.2 – Pre-amorphization with silicon, argon, and fluorine for five boron doses. Samples were annealed at 600°C for one hour.

An experiment was done to determine which ion to use for a pre-amorphization. All of the higher doses of boron were tested, ranging from 5×10^{14} to $8 \times 10^{15} \text{ cm}^{-2}$. It is reasonable to expect heavier ions to activate more boron. Silicon (28amu), fluorine (19amu), and argon (40amu) ions were used. Fluorine and argon are readily available, though argon was expected to provide greater activation as argon is chemically inert and heavier than fluorine. Currently fluorine is implanted as part of the BF_2 ion, providing a

precedent for the use of it here in this investigation. Silicon should not add any new element to the substrate and is one of the standard amorphization ions.

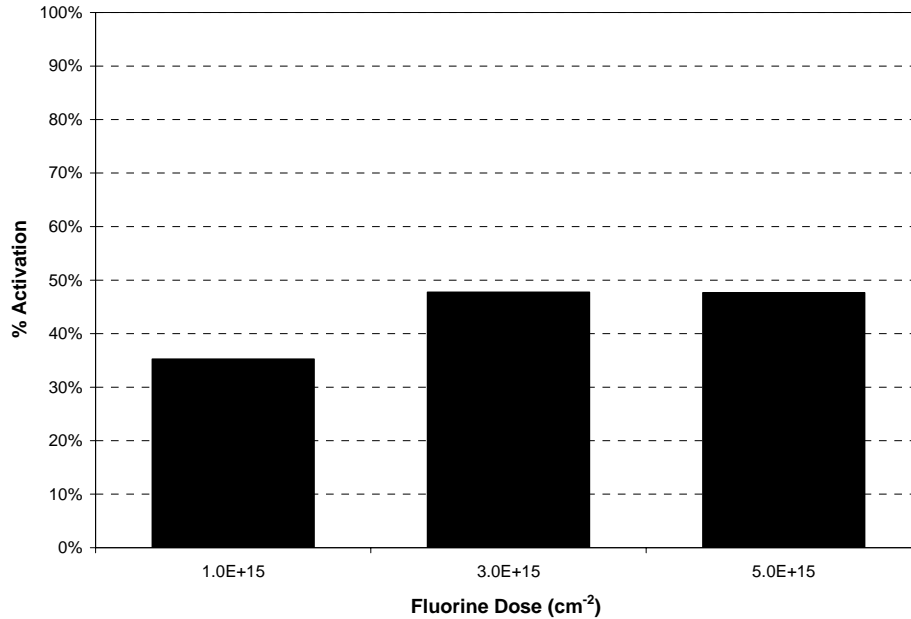


Fig. 6.3 – Fluorine pre-amorphization experiment for a constant boron dose of $4 \times 10^{15} \text{cm}^{-2}$. Samples were annealed at 600°C for one hour.

Fluorine was implanted with an energy of 75 keV and a dose of $3 \times 10^{15} \text{cm}^{-2}$. This dose was optimized by a simple screening experiment of three doses, $1 \times 10^{15} \text{cm}^{-2}$, $3 \times 10^{15} \text{cm}^{-2}$, and $5 \times 10^{15} \text{cm}^{-2}$, and it was found that the latter two show no difference in activation levels, but both are greater than the $1 \times 10^{15} \text{cm}^{-2}$ dose. This is consistent with the theory in that once enough damage is created to amorphize, more ion damage does not provide an improvement. The $1 \times 10^{15} \text{cm}^{-2}$ dose is not enough to achieve a full amorphization throughout the boron profile. Fluorine amorphization improves the activation of boron significantly; most the boron activates when fluorine is used as an amorphization ion. It should be noted that there is an active dose saturation limit of around $1.3 \times 10^{15} \text{cm}^{-2}$ for boron, similar to that of phosphorus, as seen in section 5.1. This limit will be further discussed in section 6.4.

The investigation on silicon pre-amorphization was done in part to determine whether the activation from other ions could be due to a chemical effect rather than related to the ion damage. The dose chosen for silicon was $1 \times 10^{15} \text{ cm}^{-2}$ since this is the same dose of phosphorus required to achieve full amorphization and silicon and phosphorus are very close atomic mass. The silicon was implanted at an energy of 120 keV to ensure the amorphous region extends beyond the range of the boron. Silicon provided similar activation as fluorine; however, fluorine is superior at the mid-range of doses, while silicon provides higher activation once the boron dose has reached the dose solubility limit. There does not seem to be much of an advantage of using silicon over fluorine for a pre-amorphization implant, and fluorine is available in most implanters as part of the BF_3 gas source.

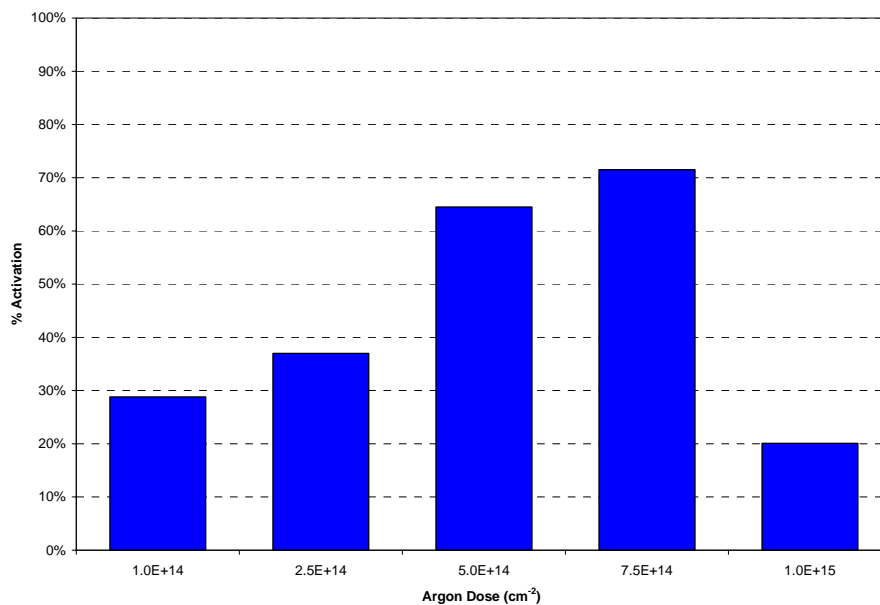


Fig. 6.4 – Percentage of Boron activation with varying argon doses. The boron dose tested was $1 \times 10^{15} \text{ cm}^{-2}$. The samples were annealed at 600°C for one hour.

A larger screening experiment was done with argon, as shown in Fig. 6.4. The implanted doses are 1×10^{14} , 2.5×10^{14} , 5×10^{14} , 7.5×10^{14} , and $1 \times 10^{15} \text{ cm}^{-2}$. It should be

noted that this is less than the fluorine doses in all cases, since it is heavier than fluorine and less should be needed to provide comparable levels of damage. The dose of boron used was $1 \times 10^{15} \text{cm}^{-2}$, as this dose gives good levels of activation with other pre-amorphization ions. The implant dose of $1 \times 10^{15} \text{cm}^{-2}$ argon actually seems to prevent activation as it reduced the active boron levels to around 20%. A dose of $5 \times 10^{14} \text{cm}^{-2}$ argon activated similar to the $7.5 \times 10^{14} \text{cm}^{-2}$, however the $5 \times 10^{14} \text{cm}^{-2}$ was used in subsequent experiments, since it was determined that this dose is sufficient to amorphize the silicon. Since all doses above $5 \times 10^{14} \text{cm}^{-2}$ should completely amorphize the boron implanted region, the presence of argon has been determined to provide less activation than fluorine or silicon pre-amorphization.

6.3 X-RAY DIFFRACTION ANALYSIS

Fig. 6.5 shows the scans for a boron and fluorine implant annealed at 600°C for one hour, compared with a fluorine implant that was not annealed. The doses used are $4 \times 10^{15} \text{cm}^{-2}$ and $3 \times 10^{15} \text{cm}^{-2}$ for boron and fluorine respectively. The peak for the annealed sample corresponds to the (220) plane, as with the phosphorus samples. The breadth of the peak for the boron implant was 1.2° , similar to that of the annealed phosphorus samples. The breadth for the fluorine implant is approximately 5° , much higher than even the unannealed phosphorus implant shown in Fig. 5.5. Therefore, the boron and fluorine implant damage is still removed by the standard anneal process; however the fluorine implant creates more damage than the phosphorus implant, having a larger impact on the pre-annealed defect density. This analysis makes similar assumptions as the analysis of the XRD of the phosphorus samples. One additional effect seen with this scan on the annealed sample is two distinct regions; the broad peak

between the angles of 46 and 48°, and at the center is a sharp peak. This is caused by mosaicity of sub-grains that have a slight mismatch in orientation. The diffraction intensity is much greater when a number of sub-grains are perfectly aligned.

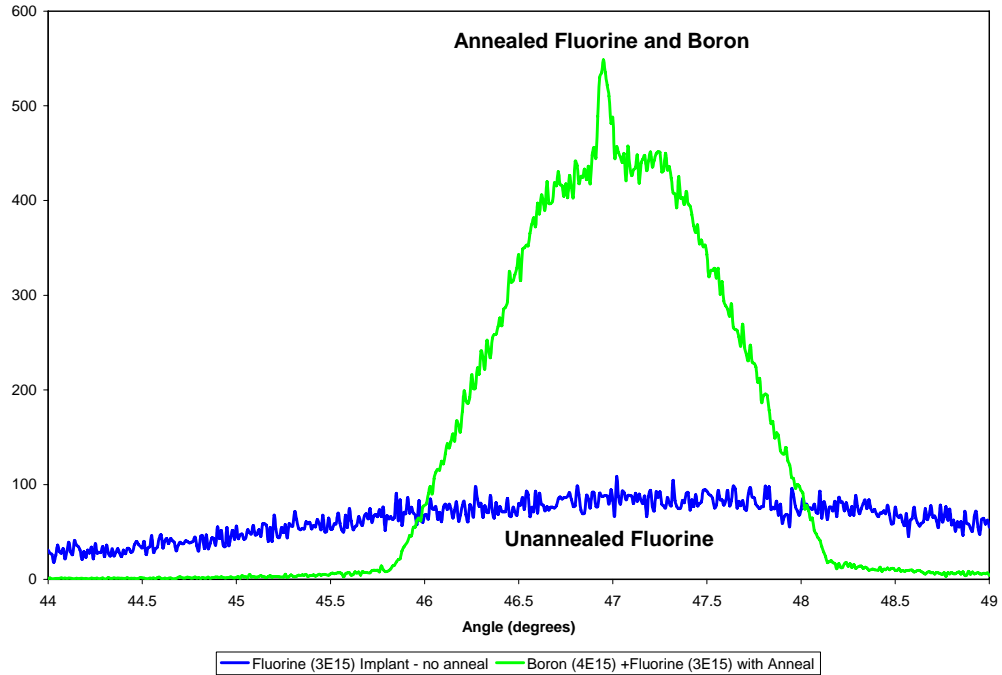


Fig. 6.5 – XRD scans for fluorine and boron with fluorine implants. The boron sample was annealed at 600°C for one hour.

6.4 ADDITIONAL STUDY ON FLUORINE AND BORON

An experiment, shown in Fig. 6.6, was done to compare results for a fluorine pre-amorphization, boron alone, and with a BF_2 implant. The BF_2 provides better activation than the boron by itself; however a separate fluorine implant gives even greater activation. The fluorine implants cause the boron to saturate at high doses, limited the activation. Rapid thermal anneals (600°C for 2 minutes) were compared with furnace anneals (600°C for 1 hour), and it was found that rapid thermal anneal of boron is superior to the furnace anneal, however, once fluorine is introduced, the activation is superior with the furnace anneal until dopant reaches the dose saturation limit. The rapid

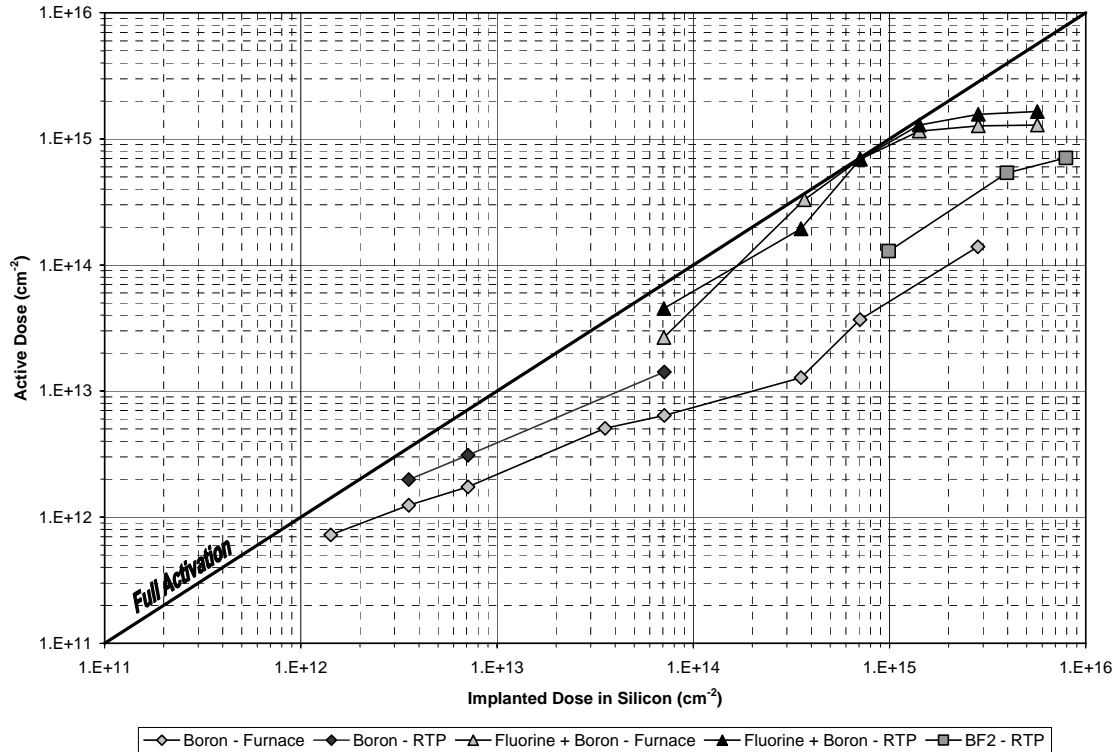


Fig. 6.6 – Boron active dose compared with active dose for BF₂ and fluorine pre-amorphization at both anneal conditions. The fluorine was implanted at 75 keV and a dose of 3x10¹⁵cm⁻² was used to provide adequate amorphization. The anneal was done at 600°C for one hour.

thermal process allows for a higher dose saturation point than the furnace, which allows it to activate more boron at high doses, greater than 1.2x10¹⁵cm⁻², which is the active dose saturation limit for the boron. This limit is exactly the same as seen with the phosphorus implants, and therefore, it must be due the annealing conditions rather than the ion used for doping. It should also be noted that when fluorine is used as a pre-amorphization ion at low boron doses, i.e. below 1x10¹⁴cm⁻², there is a mechanism that seems to inhibit the boron from activating. This is true for both types of annealing, although the furnace allows for activation down to 5x10¹³cm⁻² with fluorine. It appears as if the fluorine increases the time required to activate the dopant as the implanted dose decreases. This can be explained by considering the probability of a dopant atom finding an empty lattice

site. It is more probable with a higher dopant concentration; however the probability is reduced when additional atoms are present, since all atoms within the system compete for the same lattice sites.

Fluorine has been suggested to enhance the solid-solubility of boron [24]. This could potentially explain how fluorine improves the activation of boron over that of silicon or argon pre-amorphization, despite being lighter. The study done by Shauly and Lachman-Shalem demonstrates that by increasing the fluorine concentration results in an improvement in the activation of boron at 950°C. They performed SIMS analysis and it

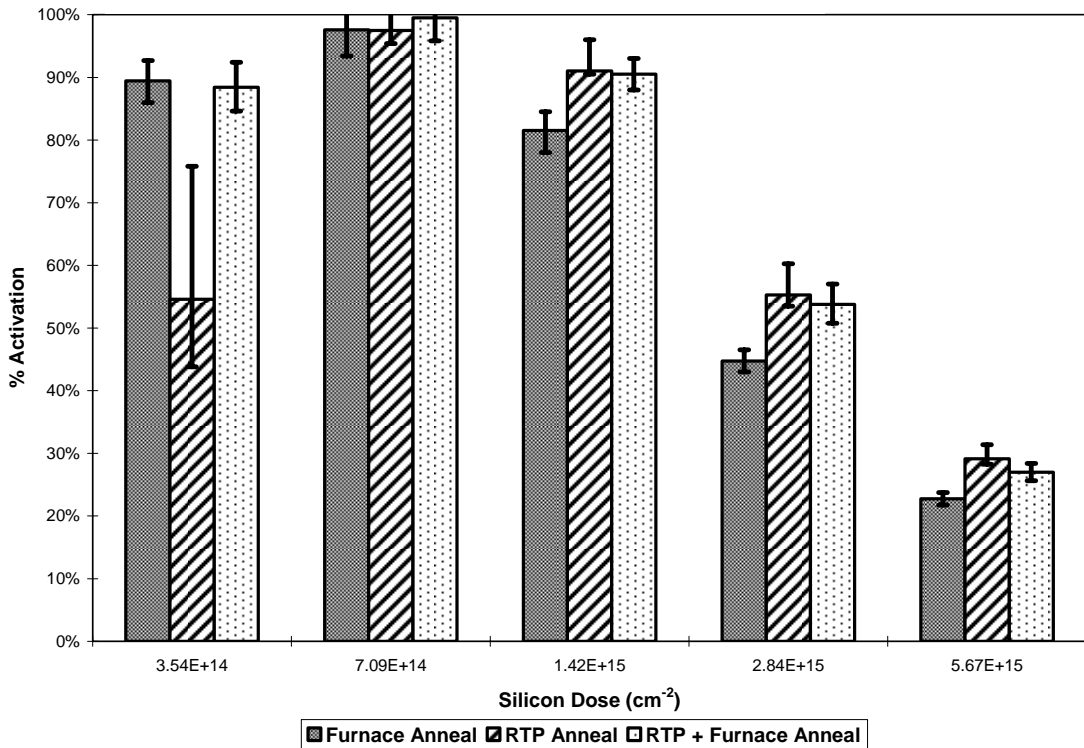


Fig. 6.7 – Anneal experiment for fluorine amorphized boron.

can be seen that the shape of the boron profile is dependent on the concentration of fluorine implanted into the silicon. However, at 600°C the boron profile is not able to respond to the fluorine implant in the same manner, and the resulting SIMS profiles are

discussed in section 6.7. In addition, electrical activation is not a given at 600°C, therefore, SRP measurements are also necessary.

This experiment shown in Fig. 6.7 discusses the percent activation for boron with a fluorine pre-amorphization at three different anneal conditions: one hour furnace, two minute RTA, and both in sequence. As with the previous experiment, it is apparent that the RTA anneal does not activate as well at lower doses, but provides a higher activation at higher doses. This leads to the assumption that there is a time-dose interaction, where the boron atoms do not have enough time to activate during the anneal when there are not as many in the silicon. However, the RTA provides higher activation where the boron is reaching the dose saturation point, since there is not enough time for the dopants to precipitate out of the lattice. An additional explanation is error in the annealing system itself. The temperature could overshoot; and there is evidence of improper calibration of the temperature readouts in the RTA system used in this experimentation. The second anneal was performed to test whether additional thermal energy could enhance or reverse the amount of activation seen from the RTA. The second furnace anneal will perform similar to that of the second anneal in the phosphorus experiments, a subsequent furnace anneal sets the active boron concentration to its equilibrium level, removing the enhancement or reduction seen from a RTA process. At $1 \times 10^{15} \text{cm}^{-2}$ dose over 90% of the boron activates. At lower doses, 5×10^{13} and $1 \times 10^{14} \text{cm}^{-2}$ (not shown), the percent activation is over 100% as predicted by the sheet resistance measurement. This indicates that the measurement gives a sheet resistance higher than what is theoretically possible for the given implant dose. This number could be due to inaccuracies in the modeling or the measurement technique itself; however, it is impossible to separate this from a single

measurement. Therefore, the focus of much of the later profiling from SRP and SIMS is on this discrepancy.

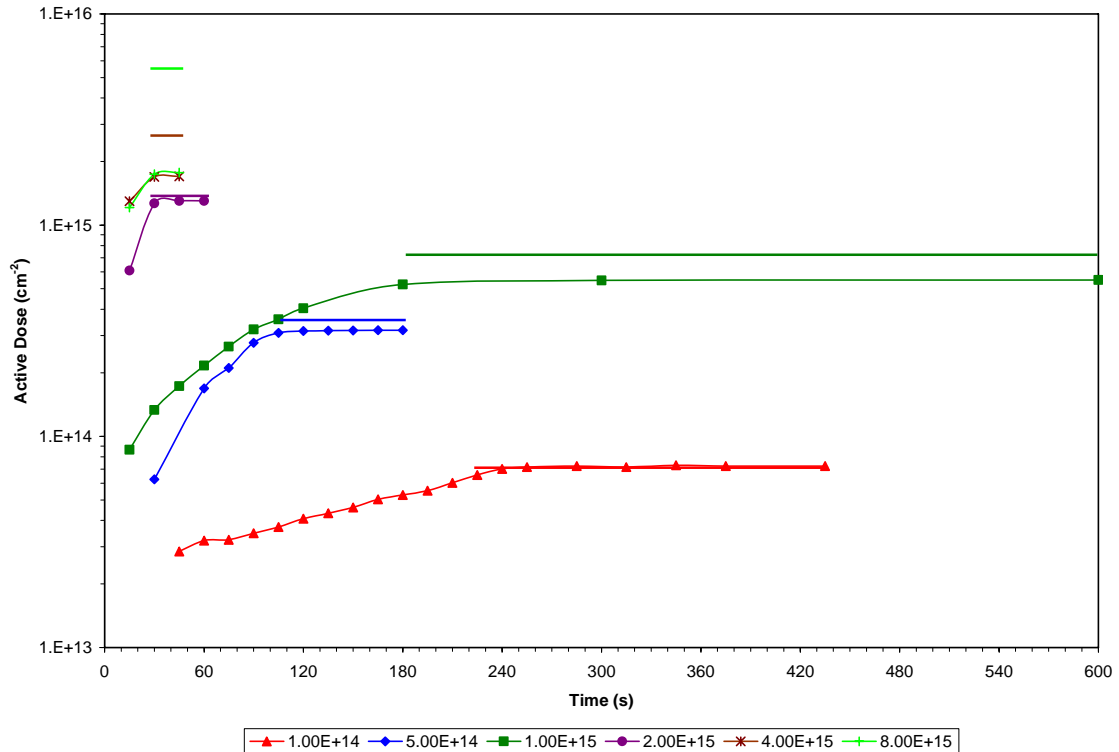


Fig. 6.8 – Active dose versus anneal time for fluorine pre-amorphized boron implants. The horizontal lines indicate 100% activation levels for each implant dose.

The anneal time has an interaction with the boron dose. It appears that the lower the dose, the longer it takes to reach the peak value of activation. Therefore, an experiment was performed to determine the time required to activate for a specific dose. The range of doses for this experiment was 5×10^{12} to $8 \times 10^{15} \text{ cm}^{-2}$. A wider range of doses was done to determine the full extent of the time dependence. All samples were pre-amorphized with $3 \times 10^{15} \text{ cm}^{-2}$ fluorine ions and annealed by rapid thermal processing. Fig. 6.8 shows the active dose versus the anneal time for the data that did show

appreciable levels of activation. The horizontal lines indicate the 100% activation level for each set of data.

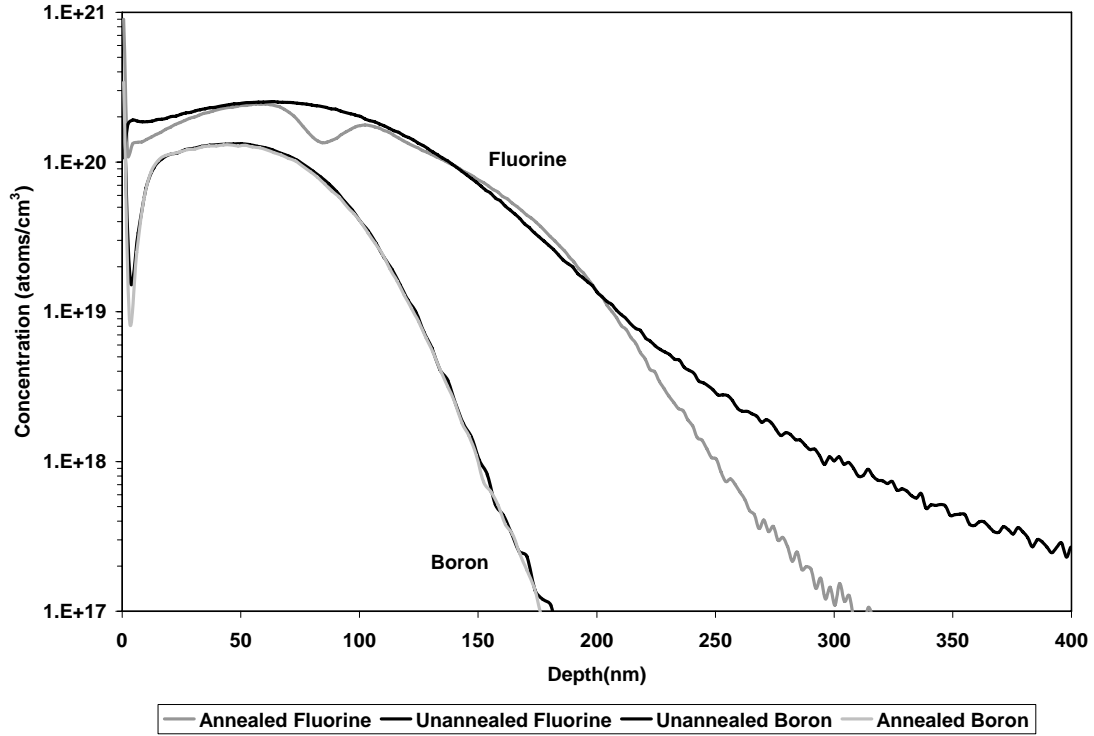


Fig. 6.9 – Adjusted Boron and Fluorine SIMS profiles before and after an anneal.

At the $1 \times 10^{14} \text{ cm}^{-2}$ dose, the time to activate is over four minutes, while at the higher dose of $8 \times 10^{15} \text{ cm}^{-2}$, the time required is only thirty seconds. This data helps to explain the data in Fig. 6.7 where there was very little activation after two minutes at low doses, but with the same anneal at high doses, the activation was higher than that of the one hour furnace anneal.

In addition to the low levels of activation, there was discoloration observed after the rapid thermal anneal. This was due to interference between the remaining damaged silicon and the crystalline silicon. The index of refraction is dependent on the concentration of dopant atoms, and therefore a change in index can account for the

discoloration observed in this experiment. This demonstrates that the solid-phase epitaxy process is dependent on the implanted dose of boron for samples that have seen a fluorine pre-amorphization. This discoloration was not present on any of the furnace annealed samples or the phosphorus implanted samples. Appendix A.2 discusses this effect in greater detail.

The SIMS data for the boron profiles required a correction factor to give results consistent with the implant dose counter. The raw data integrates to a dose greater than that of the implanted dose, indicating that this correction is necessary. The correction is applied to scale the doping concentration measured from the SIMS signal. The correction factor for the concentration scaling is 0.45.

SIMS was done a sample both before and after the anneal to determine whether any diffusion of the boron or fluorine occurs at 600°C. The anneal done was 600°C for 3 minutes. The boron profile remains unchanged; however the fluorine does exhibit a change, showing a decrease in concentration around 100nm. This decrease does not suggest diffusion in the conventional sense, but instead segregation due to material changes throughout this region. The post-anneal fluorine profile has been seen in many other cases when attempting to profile a fluorine or BF₂ implant [1]. This effect is further explained in section 6.7, where the fluorine profile is discussed.

In order to determine how the concentration profile of boron scales with dose, several SIMS profiles were done for 1×10^{14} , 1×10^{15} , and $4 \times 10^{15} \text{ cm}^{-2}$ doses. As Fig. 6.10 shows, the concentration appears to scale with dose, however, it should be noted that the pre-amorphization conditions (ions and dose) affects the depth of the profile. The argon

pre-amorphization has the steepest drop in concentration, while the silicon as the shallowest. The fluorine lies between these. Since all pre-amorphization doses were

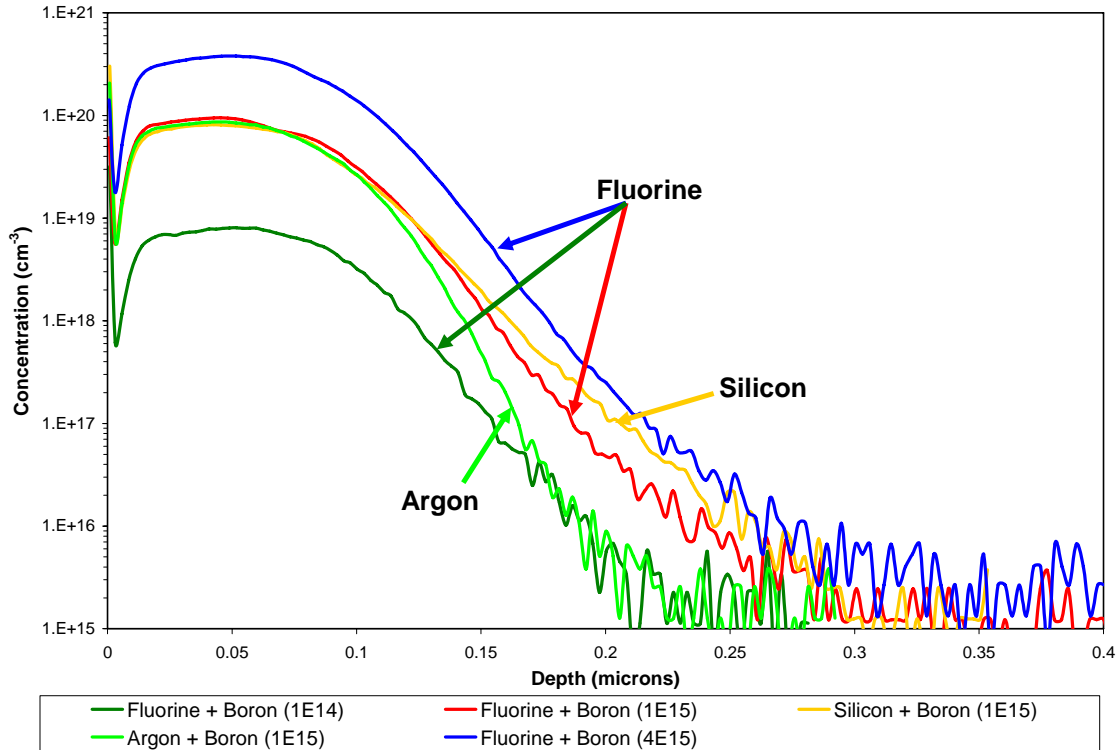


Fig. 6.10 – Boron SIMS profiles for $1 \times 10^{14} \text{cm}^{-2}$, $1 \times 10^{15} \text{cm}^{-2}$, and $4 \times 10^{15} \text{cm}^{-2}$ doses. The $1 \times 10^{15} \text{cm}^{-2}$ dose includes all three methods of pre-amorphization, fluorine, argon and silicon. All anneals were done at 600°C for 1 hour.

scaled to provide similar levels of damage, there must be a chemical effect from the ion that reduces the depth of the boron atoms. The pre-amorphization ion does not affect the maximum concentration, just how quickly the profile falls off.

Spreading resistance profiling and SIMS results are summarized on Table 6-1. When integrating the profiles from SIMS and SRP, the active and total implanted doses can be obtained. The values included are: implanted dose, silicon dose or the amount of the implant dose that should remain within the silicon, four point probe resistance, the modeled active dose from simulation, SRP dose, integrated sheet resistance from the SRP

measurement, and integrated dose from the SIMS measurement. The percent activation is first given as a ratio between the modeled active and total silicon doses. The second percent activation is a ratio between SRP dose and the SIMS dose. There are some discrepancies between the amounts of activation predicted by sheet resistance when compared with the ratio of the integrated profiles. It is easy to determine where this discrepancy arises when comparing the model profiles with the active profiles. The model does not accurately predict the amount of boron activation, due to the presence of a pre-amorphization. At best the modeling can be used as a relative comparison between samples.

Table 6-1
SRP and SIMS integrations and 4-pt. probe Results

| Implant Conditions | | | Rs Data | | | SRP Data | | | SIMS Data | |
|--------------------|--------------|--------------|-------------|-------------|-------------|----------|---------------------|---------------------|-----------|-------------|
| Species | Implant Dose | Silicon Dose | 4-pt. probe | Active Dose | % Activate | SRP Dose | R _s Int. | Solecon 4-pt. probe | Dose | % Activate |
| B+Ar | 1.E+15 | 7.1E+14 | 269.3 | 4.6E+14 | 65% | 3.8E+14 | 297 | 291.2 | 7.1E+14 | 53% |
| B+Si | 1.E+14 | 7.1E+13 | 1132.0 | 8.6E+13 | 121% | 1.9E+13 | 3324 | 1800 | 7.1E+13 | 27% |
| B+Si | 1.E+15 | 7.1E+14 | 194.9 | 6.3E+14 | 89% | 7.4E+14 | 171 | 210 | 7.2E+14 | 102% |
| B+Si | 8.E+15 | 5.7E+15 | 90.3 | 1.5E+15 | 26% | 1.9E+15 | 76 | 91.5 | | |
| B+F | 1.E+14 | 7.1E+13 | 1039.8 | 9.5E+13 | 134% | 2.7E+13 | 2557 | 1500 | 7.1E+13 | 38% |
| B+F | 1.E+15 | 7.1E+14 | 175.4 | 6.6E+14 | 93% | 5.9E+14 | 200 | 176.5 | 7.2E+14 | 82% |
| B+F | 4.E+15 | 2.8E+15 | 86.6 | 1.4E+15 | 51% | 1.5E+15 | 91 | 95.3 | 3.0E+15 | 50% |
| P+Si | 1.E+14 | 6.3E+13 | 2375.8 | 4.3E+12 | 7% | 2.0E+12 | 6963 | 4900 | 7.1E+13 | 3% |
| P | 1.E+14 | 6.3E+13 | 980.0 | 2.5E+13 | 40% | 2.3E+13 | 1020 | 1000 | 7.1E+13 | 32% |
| P | 1.E+15 | 6.3E+14 | 134.0 | 4.8E+14 | 76% | 5.8E+14 | 124 | 131.8 | | |
| P | 4.E+15 | 2.5E+15 | 56.9 | 1.2E+15 | 49% | 2.2E+15 | 49 | 57 | 1.9E+15 | 114% |

SRP of boron gives very different results than that of phosphorus. These samples had boron and fluorine ($3 \times 10^{15} \text{ cm}^{-2}$ at 75 keV) implants and two boron doses, 1×10^{15} and $4 \times 10^{15} \text{ cm}^{-2}$. Both were annealed at 600°C for one hour. The active boron profiles both cut off abruptly near 0.1µm. Beyond this is an n-type region, but not the starting wafer concentration; there is a region from 0.1µm to about 0.3µm where the n-type

concentration is changing. It is believed that the additional n-type carriers are from the fluorine implants. However, this region is not a constant concentration, but increasing from the junction until a maximum at $0.2\mu\text{m}$ and then decreases, and in the case of the $1 \times 10^{15} \text{cm}^{-2}$ boron dose, decreases below the background wafer concentration. If the fluorine allowing the is creation of electron carriers in the region between 0.1 and $0.2\mu\text{m}$, then the boron is counter-doping creating the increasing trend. Fig. 6.11 shows the single-Pearson model for amorphous implants. This model was chosen because it matches the actual profile closer than the Dual-Pearson model, used for phosphorus implants, demonstrating that the pre-amorphization removes any form of ion channeling in the silicon.

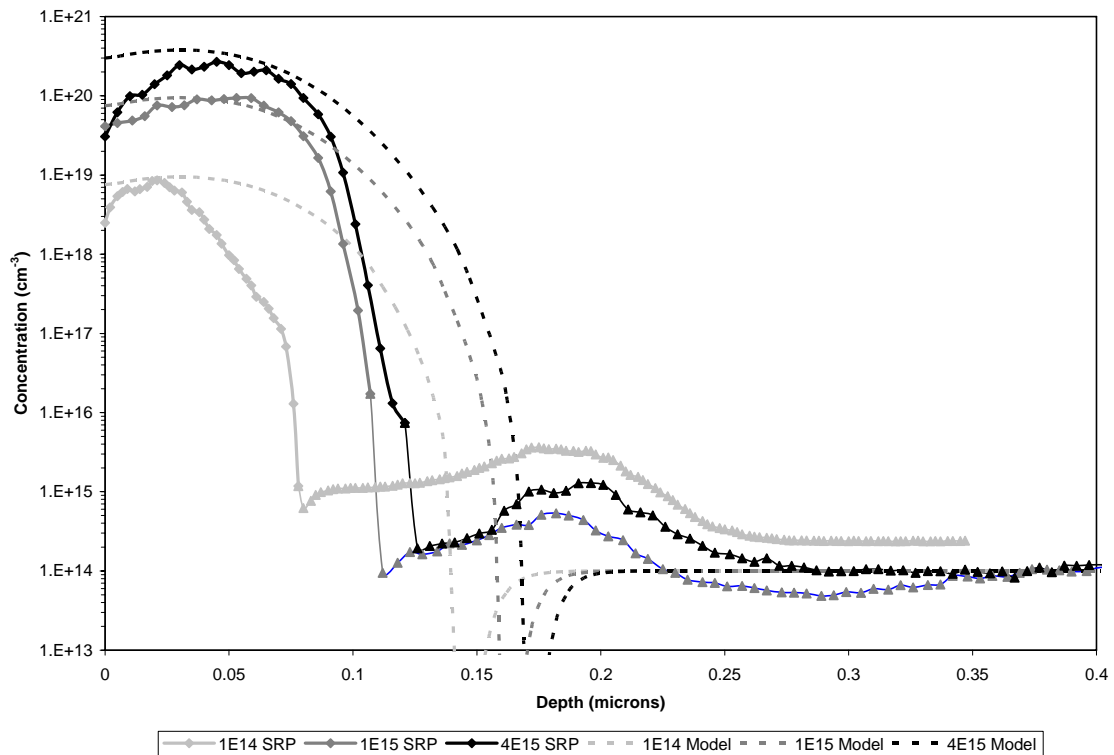


Fig. 6.11 – Boron SRP for 1×10^{14} , 1×10^{15} , and $4 \times 10^{15} \text{cm}^{-2}$ doses, overlaid with SUPREM SRP models.

The set of samples shown in Fig. 6.12 compares the effect of anneal time on activation for a $1 \times 10^{14} \text{ cm}^{-2}$ boron dose. This dose was chosen as a larger time increment will still show a large variation. A higher dose would anneal too fast for any useful data to be extracted. All samples received the same fluorine pre-amorphization, $3 \times 10^{15} \text{ cm}^{-2}$ at 75 keV. For these samples p-type wafers were used to remove the effect of the junction and associated depletion regions on the SRP measurement. However, a junction was created by fluorine doping, creating an n-type region between $0.1 \mu\text{m}$ and $0.2 \mu\text{m}$. The anneal times; one, two, and three minutes; do give increasingly higher levels of activation for increased time, showing that the anneal time of two minutes is not sufficient for a $1 \times 10^{14} \text{ cm}^{-2}$ dose.

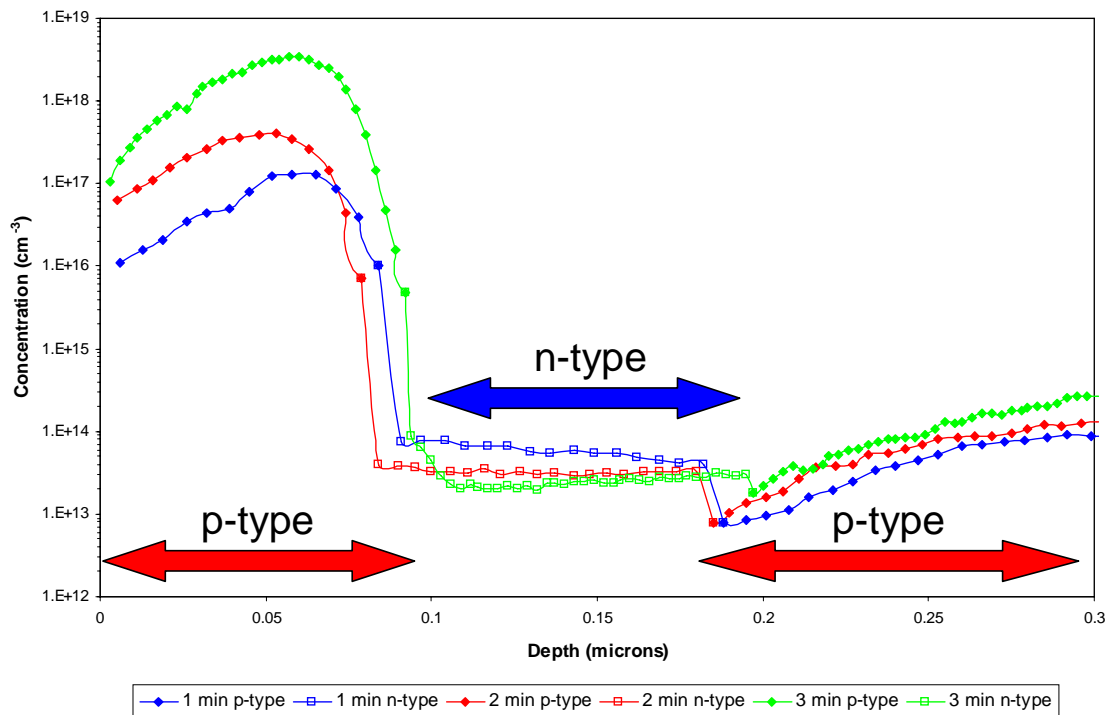


Fig. 6.12 – Boron SRP for three anneal times. The boron dose is $1 \times 10^{14} \text{ cm}^{-2}$ and annealed at 600°C .

The n-type concentration is also somewhat dependent on the anneal time, with higher concentrations for shorter times. Unlike in Fig. 6.11, the concentration of the n-type region is mostly constant. This is could be due to the starting wafer concentration, or because the boron does not have time to activate in this region, as the junction is not quite as abrupt.

SIMS and SRP can be used to determine where the inactive and active portion of the dopant exists by compared the overlaid profiles. The sensitivity of the SIMS measurement cannot detect concentrations lower than $1 \times 10^{15} \text{ cm}^{-3}$ for boron, therefore any value below this results in noise. However it can be seen that the concentrations of boron exist well below the junction depth measured by SRP. Fig. 6.13 shows the SIMS and

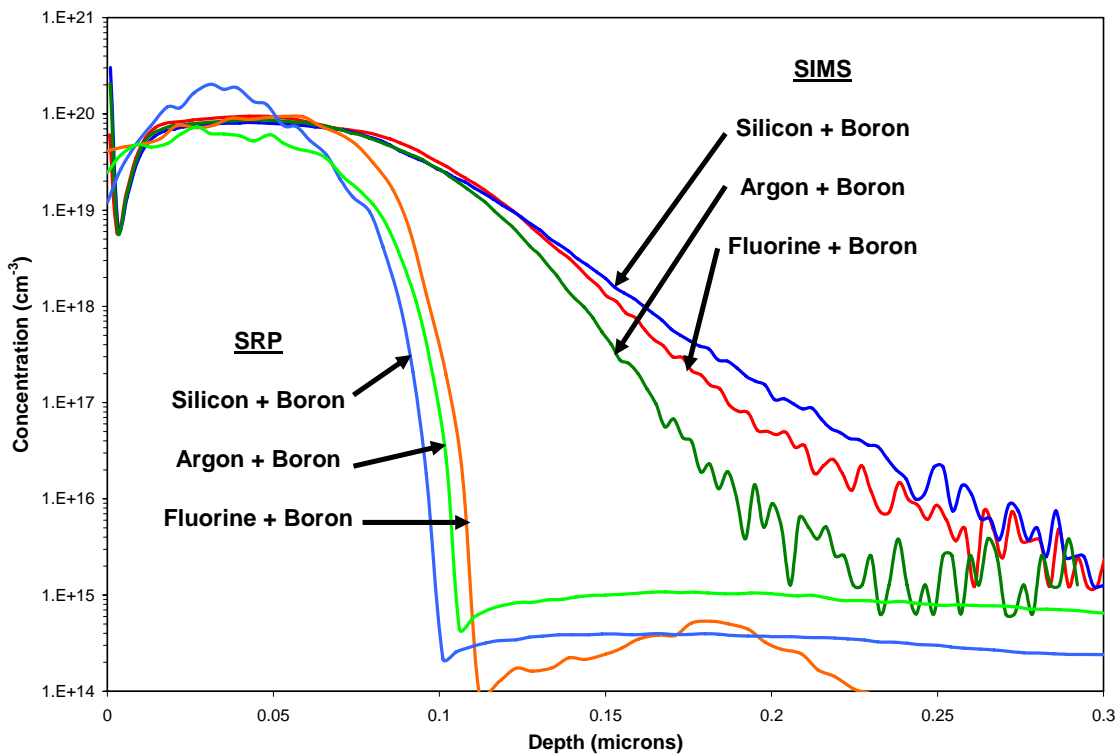


Fig. 6.13 – SRP and SIMS profiles for $1 \times 10^{15} \text{ cm}^{-2}$ boron with fluorine, argon and silicon pre-amorphization implants.

SRP overlaid for the $1 \times 10^{15} \text{cm}^{-2}$ boron implant dose and all three species used for pre-amorphizations. This further illustrates the trend discussed for Fig. 6.10, that each pre-amorphization ion creates a slightly different shaped profile for the boron implant. As the SRP shows, the junction depth for the active dopant is also slightly dependent on the pre-amorphization ion; however, this trend is not the same as with the SIMS profiles. Fluorine creates the deepest junction, while silicon creates the shallowest. In addition, the argon and silicon pre-amorphization processes do not create the unusual n-type region below the boron junction as with the fluorine process. However, the background wafer concentration for the silicon and argon samples were significantly higher than that of the fluorine sample, therefore it is possible that this n-type region could be created and is masked by the higher background concentration. It is believed that the additional ions that create the n-type region are preventing the boron from activating at this depth or that the active boron in this region is masked by counter-doped fluorine. If the latter were the case, active boron would appear for the argon and silicon pre-amorphizations and they do not. There is no evidence of argon doping. Therefore, the abrupt junction created by the pre-amorphization process is not due to fluorine counter-doping, but instead due to defects and excess interstitials that are introduced by the pre-amorphization implant. The number of ions introduced is not the controlling factor; the size of the ion combined with the number of ions must interact to control the depth of the junction. Fig. 6.14 shows the SIMS profiles overlaid with the SRP data for the $4 \times 10^{15} \text{cm}^{-2}$ boron dose and a fluorine pre-amorphization.

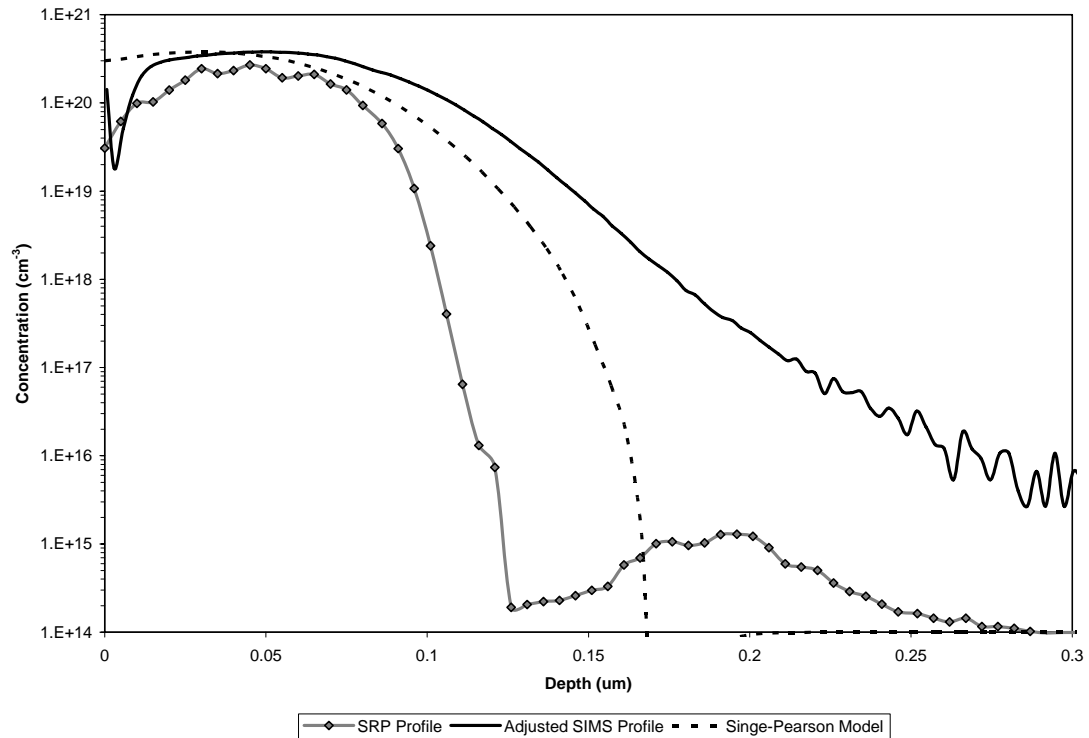


Fig. 6.14 – SRP, SIMS, and model profiles for $4 \times 10^{15} \text{ cm}^{-2}$ boron with fluorine implants.

The $1 \times 10^{14} \text{ cm}^{-2}$ boron dose provides some ambiguous results. The measured sheet resistance for these samples was greater than should be possible for this level of dopant. In order to discern the issue with this measurement, SRP and SIMS were performed on several samples at different pre-amorphization conditions for this dose. The integrated sheet resistance for these samples from the SRP data was found to be $2250 \Omega/\text{sq.}$ for the fluorine implant and $3320 \Omega/\text{sq.}$ for the silicon implant, well within the limits for this combination. These resistance values correspond to activation of 37% and 26%; the profiles are shown in Fig. 6.15. It was determined that the sheet resistance measurement at this dose when a pre-amorphization is applied is not accurate.

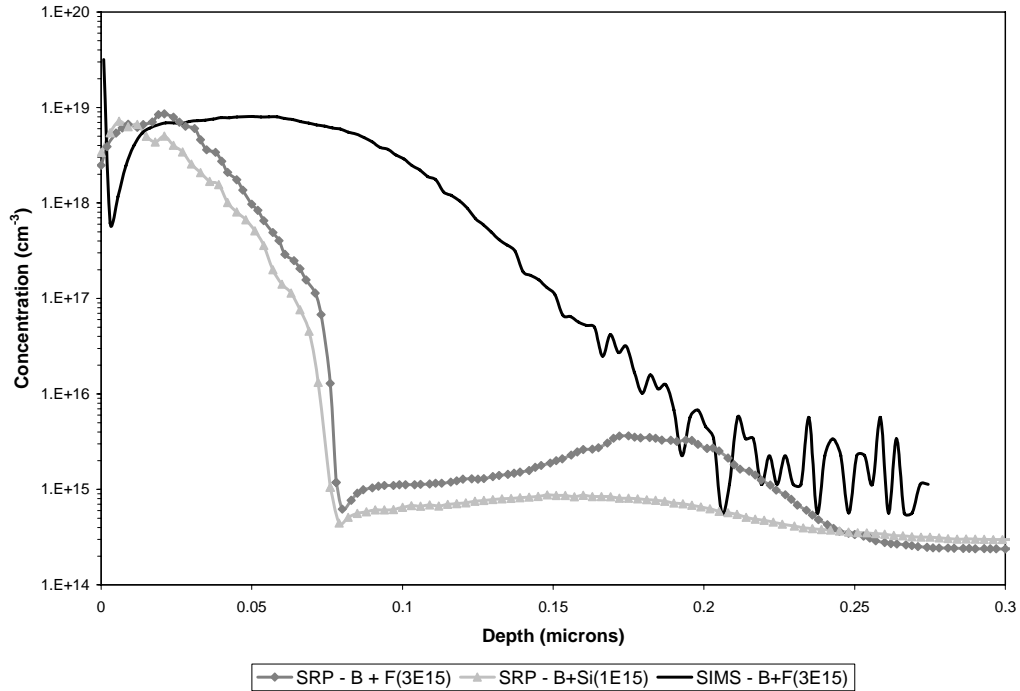


Fig. 6.15 – $1 \times 10^{14} \text{cm}^{-2}$ boron implant – SRP and SIMS comparing silicon and fluorine pre-amorphizations profiles.

6.5 TEM ANALYSIS

Transmission electron microscopy (TEM) was performed on several samples to determine the extent of defects created by the implantation process. The TEM was done at Corning Inc. on a JEOL JEM-2000FX system. Two samples received this analysis: boron and fluorine implant and a phosphorus and silicon implant. The implant dose for the pre-amorphization was the standard process outlined in section 6.2, $1 \times 10^{15} \text{cm}^{-2}$ for silicon and $3 \times 10^{15} \text{cm}^{-2}$ for fluorine. The implant dose for the active species was $1 \times 10^{14} \text{cm}^{-2}$ for both boron and phosphorus. The anneal was done at 600°C for one hour. Fig. 6.16 shows the micrograph for the boron and fluorine implant. The defects created by the implantation seem to be localized in a region 93nm below the surface of the silicon. This can be correlated to the SRP data, specifically the data shown in Fig. 6.12

and Fig. 6.15. The junction for the active boron is located above 100nm, right before the region where the defects exist. This high concentration of defects can explain the lack of boron activation below 100nm and it is possible that these defects can correspond to the anomalous n-type region that exists on the samples shown in Fig. 6.12. However the defective region is only about 27.8nm wide and the n-type region is about 100nm deep, making it unlikely that the n-type region is visible to the TEM.

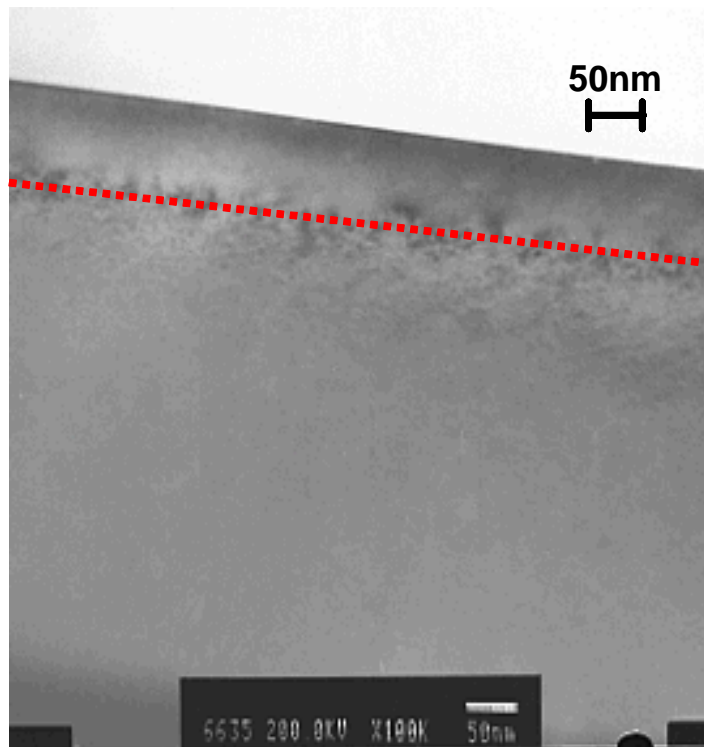


Fig. 6.16 – TEM of Boron implant with a fluorine implant used for a pre-amorphization. Anneal was done at 600°C for one hour.

6.6 LOW DOSE BORON ACTIVATION

Low concentrations of boron can be measured using MOS capacitors. Fig. 6.17 shows the data comparing a capacitor with a $2 \times 10^{12} \text{cm}^{-2}$ implant with that of a capacitor without an implant. The boron implant causes a shift to the threshold voltage which marks the region where the silicon is depleted. There are more carriers present in the

silicon, and therefore, a higher voltage must be applied to sweep them away. The difference in the threshold voltage can be used to predict the active dose by the following equation:

$$\phi = \frac{\Delta V_t C_{ox}'}{q} \quad 6.1$$

where C_{ox}' is the oxide capacitance per unit area and ΔV_t is the change in threshold voltage. For this particular dose, the amount of activation is found to be 70%, which when compared to the resistance measurement from section 6.1, is 20% more activation. The usefulness of the C-V analysis is that the measurement does not depend on the mobility of the carriers as with the sheet resistance. However, it is unlikely that this low implant dose has a serious degradation of the mobility.

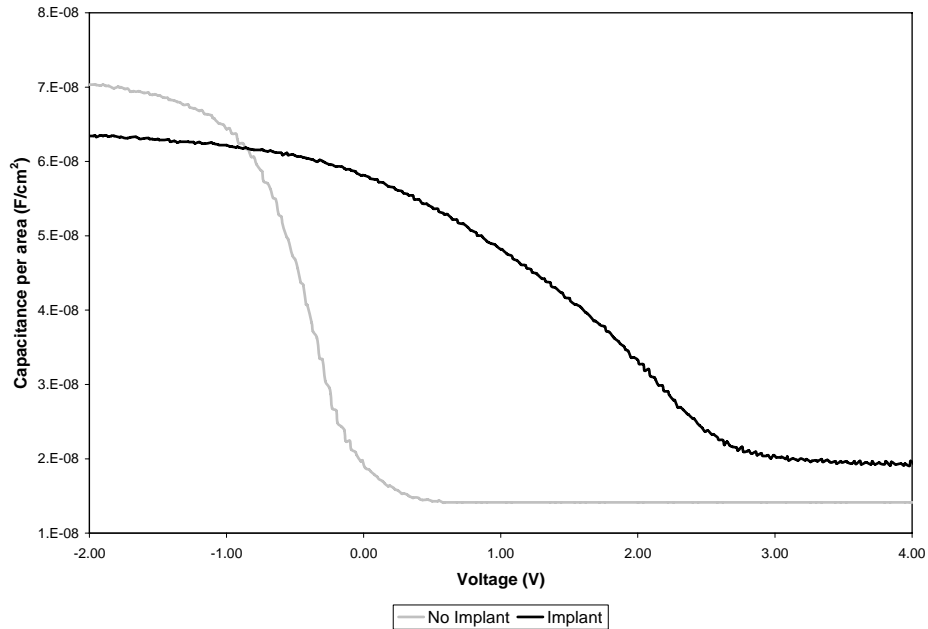


Fig. 6.17 – Capacitor-voltage measurements with and without a boron implant.

Pre-amorphizations were attempted for low boron doses, in the range of 5×10^{12} to $5 \times 10^{13} \text{ cm}^{-2}$, however, the fluorine ions apparently prevent activation, even after one hour

in the furnace. The only change observed was a slight reduction of sheet resistance; however, this effect will be discussed in the following sections. Pre-amorphizations reduce the junction depth of the implant and it is possible that if the concentration of boron is low enough, there will not be enough boron in the region that can activate to create a junction.

The dose of $5 \times 10^{12} \text{cm}^{-2}$ did not activate at all, even after one hour, showing that fluorine either prevents or slows the activation at this low dose. Neither the 1×10^{13} nor the $5 \times 10^{13} \text{cm}^{-2}$ doses achieved any significant level of activation when fluorine is involved. The sheet resistance of these samples was lower than the theoretical minimum for that implanted dose. This implies that while the boron is not activating, the ion damage combined with the extremely low level of carriers creates a series resistance that increases the wafer sheet resistance over that of the bulk.

6.7 FLUORINE AND ARGON PROFILING

In order to understand the effect of fluorine, SIMS was performed on several samples. Fig. 6.18 shows an argon profile for a $5 \times 10^{14} \text{cm}^{-2}$ dose and four fluorine profiles at a dose of $3 \times 10^{15} \text{cm}^{-2}$ for varying boron doses. The shape of the fluorine profile appears to be influenced by the amount of boron present. Without any boron, approximately 50% of the fluorine is lost in either the screen oxide or during the anneal. Once boron is introduced, the amount of fluorine lost changes; at a boron dose of $1 \times 10^{14} \text{cm}^{-2}$, 25% of the fluorine is lost, at $1 \times 10^{15} \text{cm}^{-2}$ and higher, only 5% is lost. This five percent must be the amount lost in the oxide, and the rest is due to the lower concentrations of boron. The boron traps the fluorine ions in the silicon, preventing it from out diffusing. Similarly, only 5% of the argon dose is lost, due to the screen oxide

removal. Other experiments have demonstrated that fluorine does not out-diffuse completely at higher temperatures, such as 950°C [24].

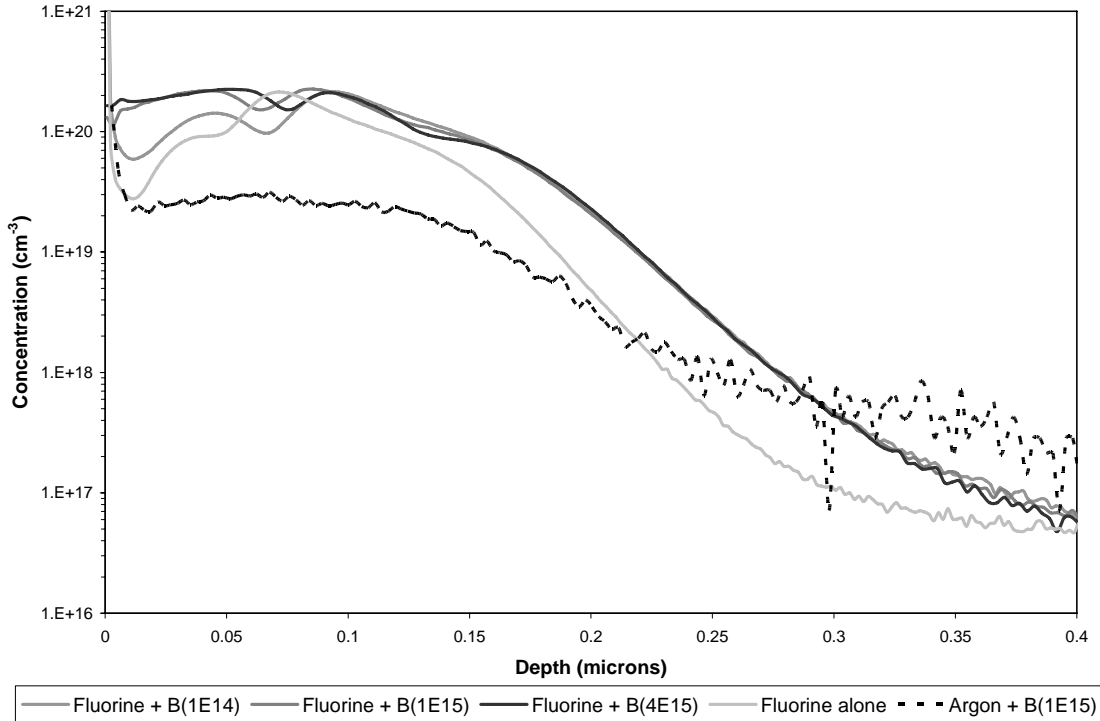


Fig. 6.18 – Fluorine and Argon SIMS profiles for no boron implant, and for boron doses of 1×10^{14} , 1×10^{15} , and $4 \times 10^{15} \text{ cm}^{-2}$. All samples annealed at 600°C for 1 hour.

Not only is the concentration of fluorine varying with boron dose, but the shape of the profile changes as well. As seen in Fig. 6.9 the annealing changes the shape of the fluorine profile, however, this effect can be different for concentrations of boron. Without any boron, the fluorine profile appears to be shifted to the left, closer to the surface. It is possible that the boron implant pushes the fluorine atoms deeper into the silicon during the implant. Each sample with boron present shows a characteristic dip in concentration near the edge of the boron profile after the anneal. At 600°C, it is likely that fluorine can diffuse only in regions that undergo the solid-phase epitaxy, however, when enough boron is present, this diffusion is prevented. This would explain how there

is a small region near the boron junction when the concentration of fluorine is reduced, although the fluorine beyond that region remains due to the crystal structure of the silicon. Without boron present, the fluorine is free to out-diffuse in the amorphous region.

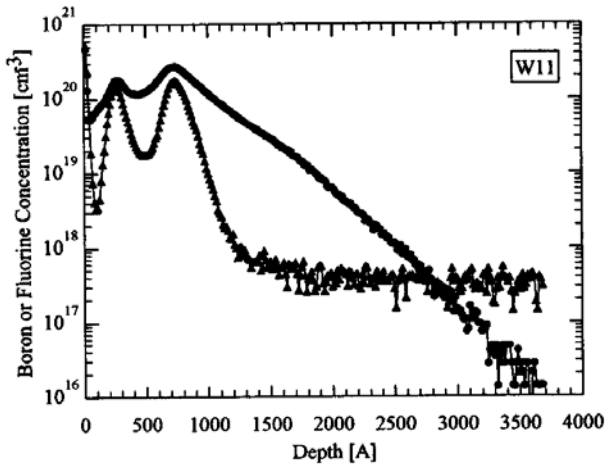


Fig. 6.19 – Experimental data from [24] showing SIMS measurements of boron and fluorine after a 950°C, 30 second anneal.

The fluorine is suspected to create an n-type region within the silicon, as shown in Fig. 6.11 and Fig. 6.12. In order to test this further, a p-type wafer was implanted with the same dose of fluorine, $3 \times 10^{15} \text{cm}^{-2}$, and then annealed at 600°C for one hour. The resulting sheet resistance was measured to be on average, 5000Ω/sq. If there was no activation, the resistance would be the same as the starting wafer, 800Ω/sq. This means that there is an n-type junction created. This sheet resistance corresponds to an effective phosphorus dose of $1.27 \times 10^{12} \text{cm}^{-2}$, giving an activation of approximately 0.05%. Therefore, a very small concentration of fluorine donates electrons in some way to the conduction of the system. Fig. 6.19 shows experimental data from the study mentioned above that illustrates the presence of a fluorine dip present after a 950°C anneal. This

study also showed this dip was not present prior to the annealing process, and the percentage lost was related to the implanted boron dose.

6.8 SUMMARY OF BORON EXPERIMENTS

Unlike phosphorus, a pre-amorphization process is necessary to activate boron. Only very low doses ($2 \times 10^{12} \text{cm}^{-2}$) were able to activate at any reasonable level without a pre-amorphization of either silicon or fluorine. A pre-amorphization with silicon or fluorine is superior to a BF_2 implant for self-amorphization, as the position of the amorphous region can be tailored to encase the boron implant, and allow the tail of the boron profile to activate. Silicon and fluorine also provide higher levels of activation compared with an argon pre-amorphization, despite the fact that argon has a higher ion mass. There is evidence that argon prevents the SPE process at high doses, which could account for the lower levels of activation seen with the argon process. In-plane XRD confirms the surface disorder due to a fluorine pre-amorphization, and the subsequent anneal of this damaged region returns to a similar state as high dose phosphorus samples. Much of the later work was done with a fluorine pre-amorphization due to availability and cost of the silicon implant. The annealing of the fluorine and boron implanted samples is similar to the annealing of phosphorus. An active dose saturation is observed as well as a time dependence to achieve a steady-state activation level. Fluorine has been observed to have donor-like behavior in regions below the boron junction. In addition, a post-anneal dip in the fluorine concentration has been identified via SIMS analysis near the junction measured by SRP. This dip has been observed under higher temperature anneals for other work. TEM confirms a highly defective region near the boron junction that could be causing this unusual behavior near the junction.

Chapter 7

Conclusion

Dopant activation with a thermal constraint of 600°C can be accomplished. In the case of donors, both phosphorus and arsenic can be used. However, phosphorus provides a more robust process for a variety of implant doses, as arsenic clusters at high concentrations and preventing activation. The amount of activation is dependent on the anneal conditions and the implant dose. For a high implant dose, short anneal times in a RTA process provide the best activation. For low doses, a long anneal in a furnace provides better activation. This general trend is true for all ion species. A pre-amorphization process does not enhance phosphorus activation; in fact it reduces it, in some cases reducing the amount of activation to near zero. The phosphorus ion is heavy enough to provide adequate self-amorphization of the silicon to allow activation at 600°C. The additional atoms from the pre-amorphization appear to degrade the activation due to the formation of secondary defects.

The results were quite the opposite for boron activation. Boron requires a pre-amorphization implant of some kind in order to activation to appreciable levels. The easiest process is to implant the BF_2 molecule. However, this provides limited activation, on the order of 20%. A co-implantation of fluorine and ^{11}B provides the best activation for the given anneal conditions and constraints. Pre-amorphizing with silicon or argon also provide enhanced activation with respect to BF_2^+ , however, argon does not give as much enhancement as silicon or fluorine. At high concentrations of argon, the activation can be even more limiting; it was shown that argon at high concentrations inhibits SPE.

The specific ion species used to create a continuous amorphous layer was shown to impact the resulting profiles significantly. There is a dependence between the pre-amorphization ion used and the depth of both the active and total boron profile. This dependence goes beyond the concentration of atoms implanted; fluorine provides the deepest active junctions, while silicon implants allow the boron to penetrate furthest into the silicon crystal. This is true even when three times as much fluorine is implanted compared with the silicon implant. The silicon implant amorphization is equivalent to fluorine in terms of activation, however each process has drawbacks. The source for silicon implants is not as common in standard semiconductor processing, whereas fluorine is readily available on most implanters. Since there is no significant enhancement at any dose/anneal condition for silicon pre-amorphization over fluorine amorphization, fluorine appears to be the better choice due to availability and cost of an implant gas source for silicon. This being said, the fluorine amorphization process has flaws as well. Fluorine has an impact on the annealing process, as it appears to increase the time required to activate boron, and fluorine has been shown to react with boron in several ways. Fluorine can change the shape of the boron profile and visa versa. Fluorine also appears to prevent lower boron doses from activating. Fluorine implants create an unusual effect below the junction of the boron profile, and in this region it can cause a donor-like behavior which is interpreted as an n-type region. However, since all pre-amorphization ions limit the electrically active junction depth of the dopants to near 100nm; this additional n-type region created by the fluorine is not solely responsible for this junction depth constraint.

The annealing process can have a drastic effect on the activation. The major difference between furnace and RTA is the ramp rate and the steady-state time. It has been observed that the time required to activate dopants depends heavily on the implanted dose, both with and without pre-amorphization. Rapid thermal processing for boron alone is an improvement over that of furnace annealing. However, once fluorine is introduced, the fluorine prevents activation at short anneal times. Therefore, RTA does not enhance the activation until the boron dose exceeds $1 \times 10^{15} \text{cm}^{-2}$ when fluorine is involved. A similar trend is observed for phosphorus, therefore the time-dose interaction is rooted in the amorphization of the silicon, not the fluorine itself, although the presence of fluorine may enhance this effect, since fluorine has been shown to reduce the motion of atoms within silicon due to diffusion. The time-dose dependence of activation is always present, however fluorine increases the time necessary to achieve final activation levels for a given boron dose. The enhancement seen with boron is due to ion damage, which boron is not capable of performing on its own.

SRP and SIMS data suggests that the junction depth of the active profiles with pre-amorphizations is limited to approximately $0.1 \mu\text{m}$. The dopant profiles extend well beyond this point, however, the limiting conditions of the anneal prevent dopant activation below this boundary. Without a pre-amorphization, the junction depth of phosphorus is $0.3 \mu\text{m}$. There is very little evidence of a concentration dependence to the activation profile, the activation is only dependent on the implant and anneal conditions, however SRP measurements were never obtained for the highest phosphorus or boron dose implants, which may exhibit an electrically active solubility limit. It is important to emphasize that SIMS and SRP are not raw measurements of doping concentration. Both

use calibration standards and there was noted inconsistency in certain measurements. In addition, the sheet resistance measurements, while accurate for high levels of activation, proved to be ambiguous for samples where a low level of activation occurs. This may be due to confounding with the background wafer doping, mobility degradation, and defects created by the implant process.

An investigation of the quality of the junctions fabricated with ion implant and low temperature annealing is currently in progress. It is possible that the junction regions between the p- and n-type regions will result in current leakage once devices are made due to defects remaining after the anneal. The models used to estimate the amount of active dopant may require adjustment, as they do not match the measured profiles in all cases. The effect of annealing has not been completely explored for each pre-amorphization condition, nor is it understood why argon prevents SPE at high concentrations. Regardless, dopant activation at low temperatures has been definitively demonstrated. The work presented here is not exhaustive; however, arguments used to explain the experimental observations present a consistent physical model for low temperature dopant activation.

References

- [1] Y. Wang et. al. *Solid-phase crystallization and Dopant Activation of Amorphous Silicon Films by Pulsed Rapid Thermal Annealing*. Applied Surface Science. 1998.
- [2] S. Wolf, Stanley, and R. Tauber, *Silicon Processing for the VLSI Era*, vol. 1, 2000.
- [3] S. Whelan, A. La Magna, V. Privitera, G. Mannino, M. Italia, and C. Bongiorno, *Dopant redistribution and electrical activation in silicon following ultra-low energy boron implantation and excimer laser annealing*. The American Physics Society, 2003.
- [4] R. F. Pierret, *Semiconductor Device Fundamentals*, 1996.
- [5] J. D. Plummer, M. D. Deal, P. B. Griffin, *Silicon VLSI Technology: Fundamentals, Practice and Modeling*. Prentice Hall, Upper Saddle River, NJ. 2000.
- [6] http://www.ifw-dresden.de/iff/11/spec/areas/diamond/spec_diamond.html
- [7] J. W. Mayer and S. S. Lau. *Electronic Science: For Integrated Circuits in Si and GaAs*. Macmillan Publishing Company, New York, 1990.
- [8] C. Kittel, *Introduction to Solid State Physics*. John Wiley & Sons, New York. 1976.
- [9] R. C. Jaeger, *Introduction to Microelectronic Fabrication*. Prentice Hill, New Jersey. 2002.
- [10] Liu, J., Downey, D., Jones, K., Ishida, E., *Fluorine Effect on Boron Diffusion*. IEEE, 1999.
- [11] Dieter K. Schroder, *Semiconductor Material and Device Characterization*. Wiley, New York, 1998.
- [12] A. Sultan, S. Banerjee, S. List, G. Pollack, and H. Hosack, *Evaluation of Si Pre-Amorphization for obtaining ultra-shallow Junctions*. IEEE, 1997.
- [13] Y. Ebiko, K. Suzuki, and N. Sasaki, *Improving the Activation of the P+ Region of Low-Temperature Polycrystalline Si TFTs by Using Solid-Phase Crystallization*. IEEE 2005.
- [14] M. E. Law, *Process Modeling for Future Technologies*. IBM Journal of Research & Development. Vol. 46, no. 2/3, pg. 339-346 2002.
- [15] J. Boussey, *Stripping Hall Effect, Sheet and Spreading Resistance Techniques for Electrical Evaluation of Implanted Silicon Layers*. Laboratoire de Physique des Composants à Semiconducteurs. 1998
- [16] R. Brennan, D. Dickey, *Determination of Diffusion Characteristics using Two- and Four-point Probe Measurements*. Solecon Laboratories Inc., San Jose, California. www.solecon.com.
- [17] M. J. Binns et. al. *The Control of Boron Auto-doping during Device Processing for P/P+ Epi Wafers with no Back-surface Oxide Seal*. 9th Int. Symposium Silicon Materials Science & Technology, Philadelphia, May 12-17, 2002.
- [18] R. S. Popovic, *Hall Effect Devices*. Institute of Physics Publishing, Philadelphia. 2004.
- [19] D. Bowen and B. K. Tanner, *High Resolution X-ray Diffractometry and Topography*. Taylor & Francis, New York. 1998.
- [20] Ohring, Milton, *The Materials Science of Thin Films*. Harcourt Brace Jovanovich, San Diego, California. 1992.

- [21] <http://www.semiconfareast.com/SIMS.htm>
- [22] M. A. Sahiner, S. W. Novak, J. Woicik, J. Liu, and V. Krishnamoorthy, *Arsenic Clustering and Precipitation Analysis in Ion-implanted Si Wafers by X-ray Absorption Spectroscopy and SIMS*. IEEE, 2000.
- [23] Jianjun Xie and S. P. Chen, *Diffusion and Clustering in Heavily Arsenic-Doped Silicon: Discrepancies and Explanation*. Physical Review Letters, Vol. 83, N. 9, August 1999.
- [24] Shauly, Eitan N., Lachman-Shalem, Sivan. *Activation improvement of ion implanted boron in silicon through fluorine co-implantation*. Journal of Vacuum Science and Technology. March/April 2004.
- [25] Athena User's Manual 2D Process Simulation Software. Silvaco International, Santa Clara, CA. 2004.

Appendix A Fabrication Processes

A.1 FURNACE ANNEALING

The furnace recipe was done such that the temperature seen by the wafer was as close to 600°C over the entire process. It is not possible to keep the process temperature exactly at 600°C for the duration of the recipe, due to stabilization and insertion. The recipe is described in detail in Table A-1. The furnace is heated to 550°C before the wafers are inserted. This is done in order to minimize the time the wafers spend ramping to the soak temperature. After the wafers are inserted, a five minute stabilization is done to ensure that the temperature is uniform throughout the furnace tube. The temperature ramps from 550°C to 600°C in fifteen minutes and allowed to soak for up to one hour.

| Table A-1 Furnace recipe details | | | | |
|--|-----------|------------|------------------|------------------|
| Step | Name | Time (min) | Temperature (°C) | gas flow (L/min) |
| 1 | heat up | 30 | 550 | 5 |
| 2 | push in | 12 | 550 | 10 |
| 3 | stabilize | 5 | 550 | 10 |
| 4 | ramp up | 15 | 600 | 10 |
| 5 | stabilize | 5 | 600 | 10 |
| 6 | soak | 50 | 600 | 15 |
| 7 | purge | 5 | 600 | 15 |
| 8 | ramp down | 15 | 25 | 10 |
| 9 | pull out | 10 | 25 | 5 |

A.2 RAPID THERMAL ANNEALING

Rapid thermal annealing is done using IR lamps as a heat source. The recipe must be calibrated in order to provide consistent heating of the wafer for each process. The recipe begins with a nitrogen purge to remove any oxygen from the ambient. This oxygen could group an oxide film at high temperatures. This effect was not a concern for this process, however, it is still important as it helps ensure that each run has a consistent ambient. The ramp rate for the anneals is 150°C/sec. In order to ramp to 600°C, the ramp time is approximately four seconds. The steady-state or soak time is determined by the process, ranging from ten seconds to three minutes. The chamber is then allowed to cool to room temperature before the next run. This is to ensure the chamber conditions are consistent from run to run. The calibration of the recipe is done by control five parameters: T_SW, GAIN, DGAIN, ICOLD, and IWARM. T_SW is the temperature at which the ramp stops and the steady-state step begins. This is set to a lower temperature than the steady-state temperature to prevent temperature spiking once the calibration parameters take over. The GAIN parameter is the amount of adjustment that is made to account for fluctuations in the chamber temperature. The DGAIN parameter is the frequency which the temperature is checked for adjustment. The ICOLD parameter is used for the first run to determine the lamp intensity at the start of the run. The IWARM parameter is automatically set to the lamp intensity at the end of the run. This is done to ensure run-to-run stability. These parameters varied over the course of the processing, however, the final version of the anneal recipe is shown on Table A-2.

Non-uniformity across the wafer was observed in the rapid thermal system. Due to this effect, various phases of the annealing were seen across the wafer. The pattern

expanded with subsequent annealing, therefore, it was determined that the non-uniformity was in the lamp intensity creating a significant thermal gradient across the wafer. This pattern must be due to different phases of silicon creating interference effects. This indicates that the SPE process has not be completed during the anneal. Since different implant doses were used, it was determined that the time for SPE was dependent on the implant dose as well as the anneal temperature.

| <u>Table A-2</u> RTA recipe calibration parameters | |
|--|------|
| T_SW | 64 |
| GAIN | -20 |
| DGAIN | -15 |
| ICOLD | 1476 |

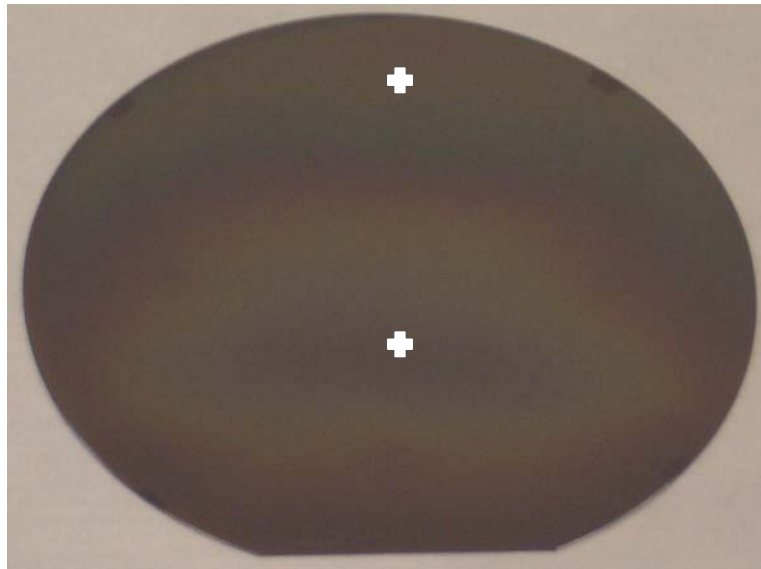


Fig. A.1 – Wafer annealed for 3 minutes at 600°C. Points indicate where SRP was done.

Due to uniformity issues in the annealing, it was necessary to remove averaging in some of the data. The RTA system uses a pyrometer to measure the emissivity of the silicon to control the temperature during the anneal. The pyrometer reads in the center of

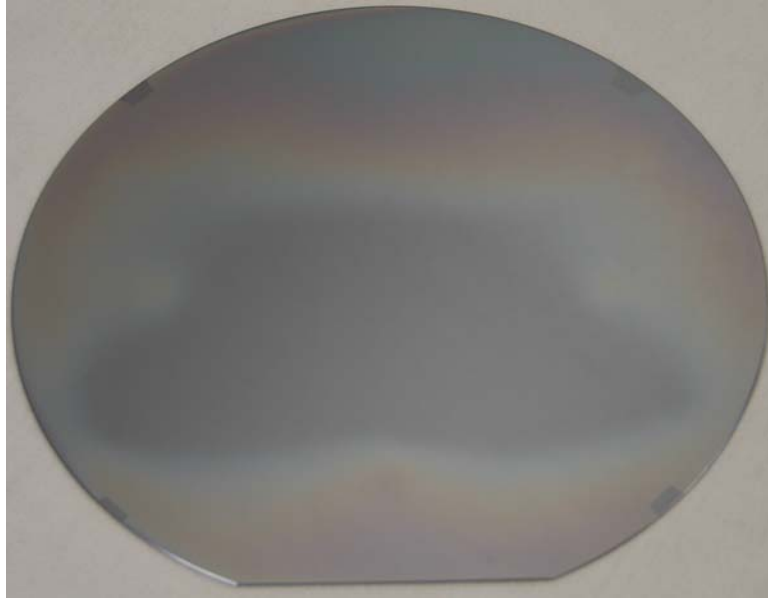


Fig. A.2 – Wafer annealed at 600°C for 5.5 minutes. Implant is $5 \times 10^{13} \text{cm}^{-2}$ of boron.

the wafer, therefore, when averaging across the wafer failed to accurately characterize the process; the center point was used as a metric.

The wafers shown in Fig. A.1, Fig. A.2, and Fig. A.3 illustrate how this anneal non-uniformity is observed. It should be noted that the non-uniformity in the coloration of the wafer is present in the sheet resistance as well. This pictures illustrate the final anneal, as each of these samples was annealed many times at time increments of fifteen seconds. This test was done to show how this discoloration and change in sheet resistance is changes with anneal time. Once the experiment was complete, the wafer was annealed in the furnace, a process that removes any discoloration and completes the anneal. The difference between the $5 \times 10^{13} \text{cm}^{-2}$ and the $5 \times 10^{14} \text{cm}^{-2}$ shows how the discoloration is dependent on the implant dose as well, since even though the dose is much higher, the discoloration is removed faster. The sample shown in Fig. A.1 was sent for SRP, to further examine how the shape of the doping profile changes due to this discoloration.

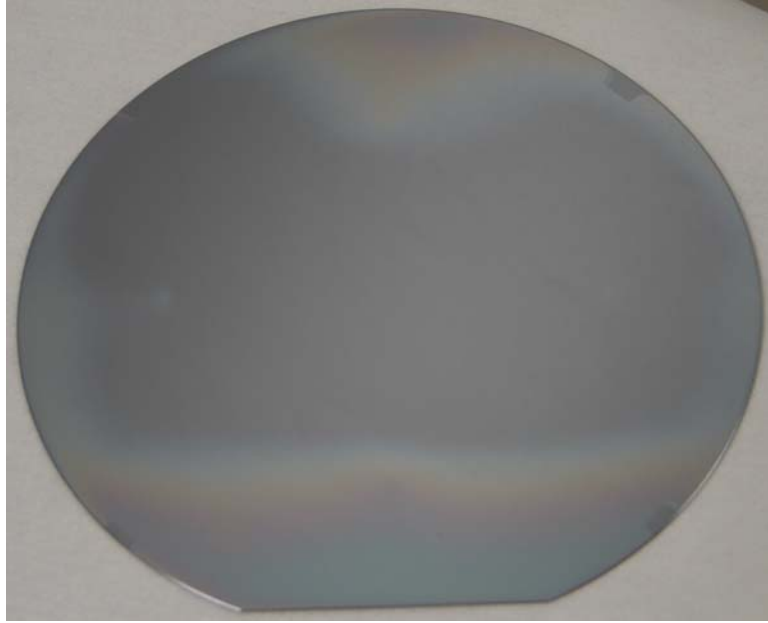


Fig. A.3 – Wafer Annealed at 600°C for 3 minutes. Implant is boron at $5 \times 10^{14} \text{ cm}^{-2}$ dose.

SRP data for variations across the wafer shows that the activation is indeed incomplete. One scan was done near the center of the wafer, the region that appeared to be crystalline silicon, while the second was done near the edge where the sheet resistance was highest. This data proves that the discoloration in the wafer can be correlated to the activation of boron. The sample measured was one with the n-type region discussed in section 6.4. It can be seen here that this n-type region is dependent upon boron activation, since at different points of the same wafer, various amounts of both boron and fluorine become active. This could be due to boron counter-doping the n-type region. The n-type concentration is higher than the background p-type concentration of the edge point, while at the center this concentration is lower than the background. This shows that the doping effect of the fluorine is high enough to overcome the background concentration, and that the activation of additional boron serves to compensate where the anneal is complete.

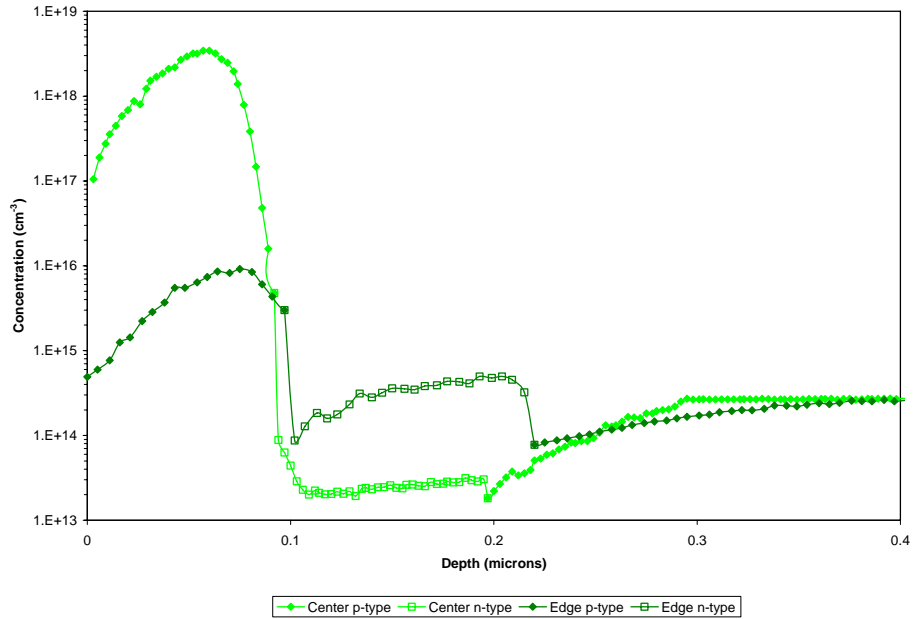


Fig. A.4 – SRP from two points on an incomplete anneal. The sample was implanted with $1 \times 10^{15} \text{ cm}^{-2}$ boron and annealed for three minutes.

A.3 TEOS DEPOSITION

The screen oxide used in this experiment was a PECVD, or plasma-enhanced chemical-vapor deposition, deposited oxide referred to as TEOS, due to the deposition precursor, Tetra-Ethyl-Ortho-Silicate. The advantage of using this process is that the temperature at which the oxide is deposited is only 390°C. This prevents using any thermal processing even before the dopants are introduced into the silicon, ensuring that any defect sites that exist in the starting wafer will not be artificially removed by using a thermally grown oxide. The recipe uses a thirty second stabilization and a deposition time of 10.3 seconds. This is followed by a ten second lift-off step to remove any unreacted TEOS. The power used for the deposition is 255 watts, to give a target thickness of 100nm.

Appendix B Table of Experiments

Table B-1
Phosphorus Experiments

| Experiment | Variables | Constants | Anneal Type | Sample Numbers |
|-------------------------------|--|--|-------------------|---|
| Anneal Experiment | Anneal time (10 sec - 1 hour) temperature (550 - 650C) | Implant energy Implant dose | RTA or Furnace | p1, p2, p3, p4, p5, p6, p7, p8, p13, p14, p15, p16, p17, p18, p19, p20, p21, p22, p23, p24, p25 |
| Dose Experiment | Implant Dose (5E12 - 8E15) | Anneal time Temperature Implant energy | Furnace | p4, p29, p30, p31, p32, p33, p34, p35, p36 |
| Second Anneal Experiment | First anneal time (10 sec - 1 hour) First anneal (550 - 650C) Implant Dose (5E12 - 8E15) Anneal (RTA, Furnace, Both) | Implant energy | Both | p1, p2, p3, p4, p5, p6, p7, p8, p13, p14, p15, p16, p17, p18, p19, p20, p21, p22, p23, p24, p25, p29, p30, p31, p32, p33, p34, p35, p36 |
| Rapid Thermal - Phosphorus | Implant Dose (5E12 - 8E15) | Anneal time Temperature Implant energy | RTA | p41, p42, p43, p44, p45, p50, p51 |
| Pre-amorphization | Implant Dose (1E14 and 1E15) Pre-amorphization (F and Si) | Anneal Time Anneal Temperature Implant Energy | Furnace | SP1, SP2, p54, p55 |
| Spreading Resistance | Implant Dose (1E14, 1E15, and 4E15) Fluorine pre- amorph | Anneal time Temperature Implant energy | Furnace | SP1, p32, p34, p36 |
| SIMS analysis | Implant Dose (1E14 and 4E15) Fluorine pre- amorph | Anneal time Temperature Implant energy | Furnace | SP1, p42, p7 |

Table B-2
Arsenic Experiments

| Experiment | Variables | Constants | Anneal Type | Sample Numbers |
|-----------------|-----------------------------------|--|----------------------|--|
| Dose Experiment | Implant dose (1E14 to 4E15) | Implant Energy Anneal Time Anneal Temperature | RTA and Furnace | AP1, AP2, AP3, AP3, AP4, AP5, AP6, AP7, AP8, AP9, AP10 |
| Second Anneal | Implant dose (1E14 to 4E15) | Implant Energy Anneal Time Anneal Temperature | Secondary Furnace | AP1, AP2, AP3, AP3, AP4, AP5, AP6, AP7, AP8, AP9, AP10 |

Table B-3
Boron Experiments

| Experiment | Variables | Constants | Anneal Type | Sample Numbers |
|-----------------------------------|---|--|-------------------|--|
| Boron Implant | Boron Dose (2E12 - 4E15) | Implant Energy Anneal Time Anneal Temperature | Furnace or RTA | n46, n47, n48, n83, n84, n85, B21, B3 |
| Low Dose Anneal Time | Boron Dose (5E12 - 1E14) Anneal Time (60 and 120 sec) | Implant Energy Anneal Temperature | RTA | n28, n29, n30, n31, n32, n33 |
| Pre-amorphization | Pre-amorphization (Ar, Si, F) Boron Dose (1E14 - 4E15) | Implant Energy Anneal Time Anneal Temperature | Furnace | SN1, SN2, SN3, SN4, SN5, SN6, SN7, SN8, n51, n53, n55, n57, n59, n61, n87, n77, n78, n79, n80, n81, n82 |
| Argon Dose | Argon Dose (1E14 - 1E15) Boron Dose (1E14 - 4E15) | Implant Energy Anneal Time Anneal Temperature | Furnace | n86, n88, n89, n90, n91, n78, n80 |
| Fluorine Energy | Fluorine Energy (75 and 100) | Boron Dose Implant energy Anneal Time Anneal temperature | Both | n65, n66, n67, n68 |
| Pre-amorphization and Anneal Time | Boron Dose (1E14 - 8E15) Anneal Time (60, 120 sec) | Fluorine Dose/Energy Boron Energy Anneal Temperature | RTA | n26, n27, n34, n35, n36, n37, n38, n39 |

Table B-3

Boron Experiments - continued

| Experiment | Variables | Constants | Anneal Type | Sample Numbers |
|-------------------------------|---|--|--------------------|--|
| Fluorine Pre-amorphization | Boron Dose (5E13 - 8E15) Anneal (RTA, Furnace, Both) | Implant Energy Anneal Time Anneal Temperature | Both | n51, n52, n53, n54, n55, n56, n57, n58, n59, n60, n61, n62, n3, n64 |
| BF2 Experiment | BF2 Dose (1E15 - 8E15) | Implant Energy Anneal Time Anneal Temperature | RTA | n40, n41, n42, n43, n44, n45 |
| Anneal Time | Anneal Time (15 - 300 sec) Boron Dose (5E12 - 8E15) | Implant Energy Anneal Temperature | RTA | n49, n50, n69, n70, n71, n73, n74, n75, n76 |
| Spreading Resistance | Boron Dose (1E14 - 8E15) Pre-amorphization (Ar, F) Anneal Time (1 - 3 min) | Implant Energy Anneal Temperature | Both | p38, p39, p40, n58, n60, n78, n87, SN1, SN7, SN8 |
| SIMS Analysis | Boron Dose (1E14 - 8E15) Pre-amorphization (Ar, F) | Implant Energy Anneal Time Anneal Temperature | Furnace | SN7, n78, p53, n87, n57, n59 |

Appendix C Sheet Resistance Data

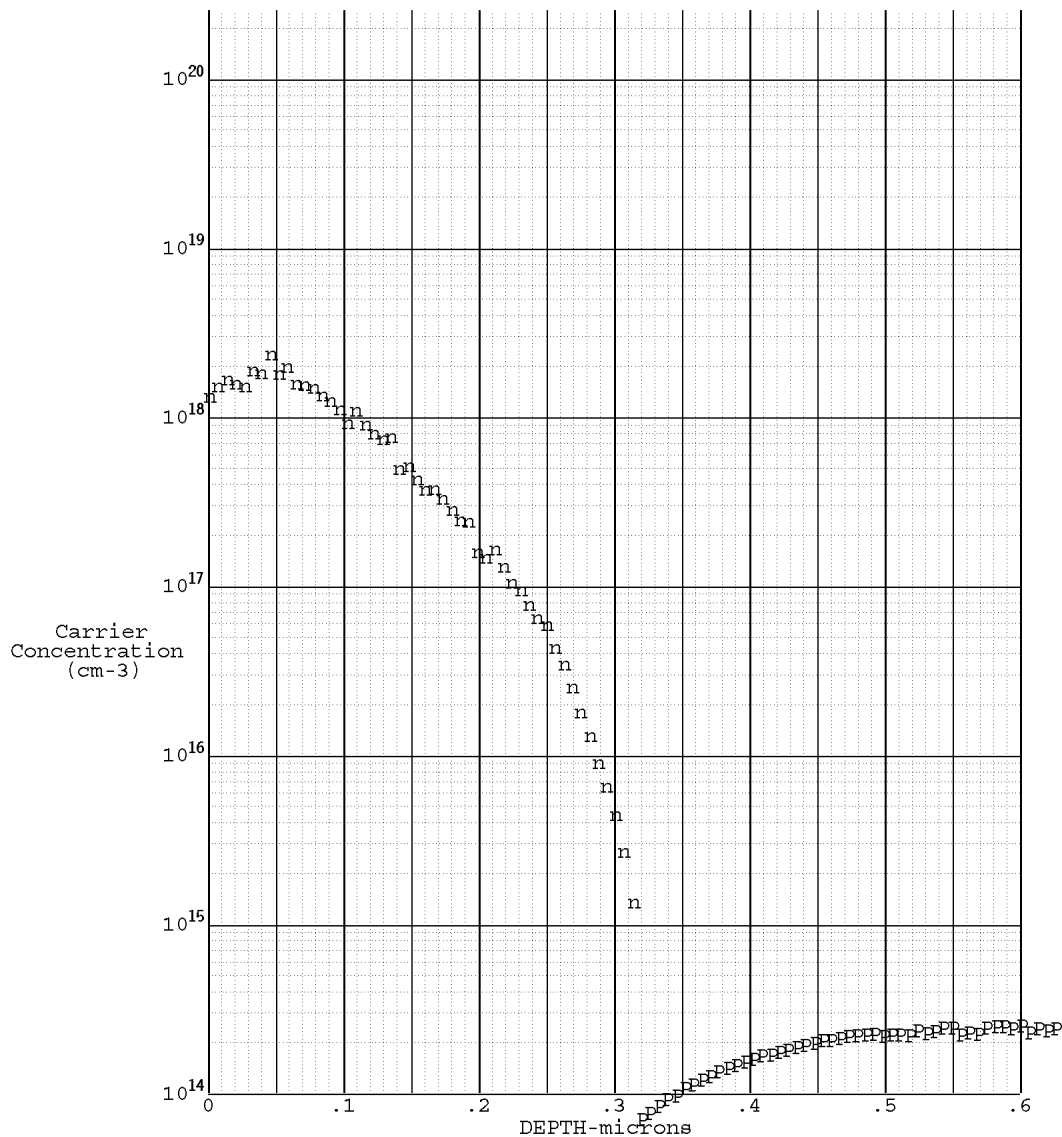
Table C-1
P-type wafers

| Wafer ID | Starting Rs | First Anneal Rs | Second Anneal Rs | Wafer ID | Starting Rs | First Anneal Rs | Second Anneal Rs |
|----------|-------------|-----------------|------------------|----------|-------------|-----------------|------------------|
| p1 | 541.69 | 53.459 | | p35 | 624.422 | 75.6317 | |
| p2 | 442.68 | 55.624 | | p36 | 590.998 | 56.9026 | |
| p3 | 429.47 | 47.7325 | 56.7125 | p37 | 618.134 | | |
| p4 | 492.23 | 54.539 | | p38 | 624.568 | | |
| p6 | 499.11 | 59.982 | | p39 | 626.404 | | |
| p7 | 534.17 | 63.911 | | p40 | 593.299 | | |
| p8 | 524.37 | | | p41 | 612.224 | 1668.6 | 1281.33 |
| p9 | 535.25 | 298.23 | | p42 | 625.473 | 1526.7 | 959.45 |
| p10 | 515.5 | 3095.97 | | p43 | 614.622 | 324.824 | 281.965 |
| p11 | 523.07 | | | p44 | 630.972 | 146.681 | 135.183 |
| p12 | 520.29 | | | p45 | 615.878 | 76.1667 | 74.5821 |
| p13 | 501.23 | 56.94 | | p50 | 528.995 | 66.9899 | 73.5881 |
| p14 | 457.2 | 58.473 | | p51 | 556.929 | 48.9539 | 57.2001 |
| p15 | 500.73 | 60.56 | | p53 | 526.477 | | |
| p16 | 468 | 63.894 | | p54 | 552.675 | 1194.58 | |
| p17 | 529.85 | 53.776 | 61.2953 | p55 | 529.992 | 152.827 | |
| p18 | 458.96 | 52.593 | 61.599 | SP1 | 313.584 | 2375.78 | |
| p19 | 527.83 | 60.837 | 60.674 | SP2 | 424.603 | 158.419 | |
| p20 | 458.4 | 101.65 | 62.34 | AP1 | 324.6 | 1031.07 | 840.322 |
| p21 | 527.66 | 55.609 | 62.44 | AP2 | 315.052 | 847.835 | |
| p22 | 558.8 | 54.567 | 61.7974 | AP3 | 420.098 | 236.539 | 222.009 |
| p23 | 533.21 | 60.337 | | AP4 | 422.464 | 219.312 | |
| p24 | 561.16 | 66.2467 | | AP5 | 338.686 | 137.031 | 130.815 |
| p25 | 554.83 | 64.654 | | AP6 | 338.784 | 132.208 | |
| p26 | 606.067 | | | AP7 | 338.044 | 77.733 | 91.1483 |
| p27 | 639.941 | | | AP8 | 336.764 | 93.779 | |
| p28 | 626.428 | | | AP9 | 339.235 | 153.699 | 138.449 |
| p29 | 626.033 | 3730.58 | | AP10 | 337.987 | 151.044 | |
| p30 | 627.621 | 2609.38 | | RP1 | 338.656 | 1748.71 | |
| p31 | 606.222 | 1249.44 | | XP1 | 397.896 | 1104.6 | |
| p32 | 621.296 | 980.48 | | XP2 | 420.792 | | |
| p33 | 622.464 | 280.98 | | XP3 | 423.92 | 63.27 | |
| p34 | 624.37 | 133.99 | | | | | |

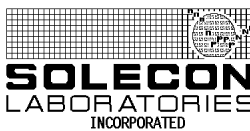
Table C-2
N-type wafers

| Wafer ID | Starting Rs | First Anneal Rs | Second Anneal Rs | Wafer ID | Starting Rs | First Anneal Rs | Second Anneal Rs |
|----------|-------------|-----------------|------------------|----------|-------------|-----------------|------------------|
| n20 | 207.27 | 338.749 | 937.375 | n63 | 828.1 | 100.715 | 101.268 |
| n21 | 204.261 | 203.53 | 1112.7 | n64 | 814.78 | 111.565 | |
| n22 | 206.229 | 638.047 | 314.678 | n65 | 817.91 | 1221.41 | |
| n23 | 207.648 | 214.268 | 172.383 | n66 | 816.47 | 1727.46 | 1283.89 |
| n26 | 833.73 | 202.77 | 185.274 | n67 | 801.285 | 96.775 | |
| n27 | 834.753 | 189.431 | 189.835 | n68 | 831.94 | 113.971 | |
| n28 | 835.928 | 11530 | 10709 | n69 | 831.863 | 1337.36 | 1283.17 |
| n29 | 826.21 | 10240 | 10992 | n70 | 835.326 | 2113.28 | |
| n30 | 823.393 | 7877 | 7321.6 | n71 | 820.564 | 360.38 | |
| n31 | 825.99 | 7350.1 | 7897.41 | n72 | 822.737 | | |
| n32 | 825.42 | 2863.1 | 3473.2 | n73 | 832.611 | 98.719 | |
| n33 | 818.08 | 2856.3 | 3769.62 | n74 | 814.23 | 77.5211 | |
| n34 | 835.98 | 3123 | 1762.87 | n75 | 834.781 | 74.4129 | |
| n35 | 828.86 | 2178.5 | | n76 | 234.848 | 273.789 | |
| n36 | 821.07 | 77.93 | 80.5732 | n77 | 265.24 | 487.987 | |
| n37 | 824.11 | 80.405 | 82.894 | n78 | 269.276 | 261.532 | |
| n38 | 827.8 | 77.094 | 83.508 | n79 | 267.385 | 255.561 | |
| n39 | 830.751 | 78.692 | 84.428 | n80 | 305.171 | 640.975 | |
| n40 | 827.57 | 613.62 | 557.114 | n81 | 237.764 | 92.2058 | |
| n41 | 828.08 | 624.16 | 571.352 | n82 | 310.348 | 291.773 | |
| n42 | 850.65 | 193.1 | 183.998 | n83 | 295.062 | 5294.39 | |
| n43 | 825.3613 | 203.36 | 192.325 | n84 | 286.973 | 4565.25 | |
| n44 | 832.45 | 167.25 | 146.763 | n85 | 300.509 | 3027.42 | |
| n45 | 845.47 | 159.943 | 145.567 | n86 | 283.265 | 130.097 | |
| n46 | 838.48 | 24534 | | n87 | 282.314 | 1039.75 | |
| n47 | 832.373 | 15031 | | n88 | 284.622 | 637.873 | |
| n48 | 823.71 | 11370 | | n89 | 308.425 | 237.771 | |
| n49 | 823.51 | 848.447 | 732.154 | n90 | 314.781 | 433.959 | |
| n50 | 825.81 | 1722.26 | 2147.11 | n91 | 293.671 | 543.27 | |
| n51 | 815.175 | 2030.33 | | SN1 | 257.144 | 1131.95 | |
| n52 | 827.02 | 1299.16 | 2020.91 | SN2 | 355.037 | 253.964 | |
| n53 | 828.875 | 1306.55 | | SN3 | 249.674 | 1385.25 | |
| n54 | 823.38 | 1844.6 | 1325.09 | SN4 | 328.891 | 359.695 | |
| n55 | 820.31 | 352.733 | | SN5 | 354.462 | 126.781 | |
| n56 | 815.66 | 569.108 | 368.787 | SN6 | 230.291 | 85.7388 | |
| n57 | 819.444 | 178.505 | | SN7 | 356.718 | 194.903 | |
| n58 | 816.775 | 178.78 | 175.353 | SN8 | 237.397 | 90.259 | |
| n59 | 820.75 | 102.39 | | XN1 | 362.074 | | |
| n60 | 818.582 | 84.27 | 86.6805 | XN2 | 248.88 | 94.13 | 98.4596 |
| n61 | 834.987 | 100.734 | | B3 | | 652.34 | |
| n62 | 821.01 | 80.535 | 86.3223 | B21 | | 1628.7 | |

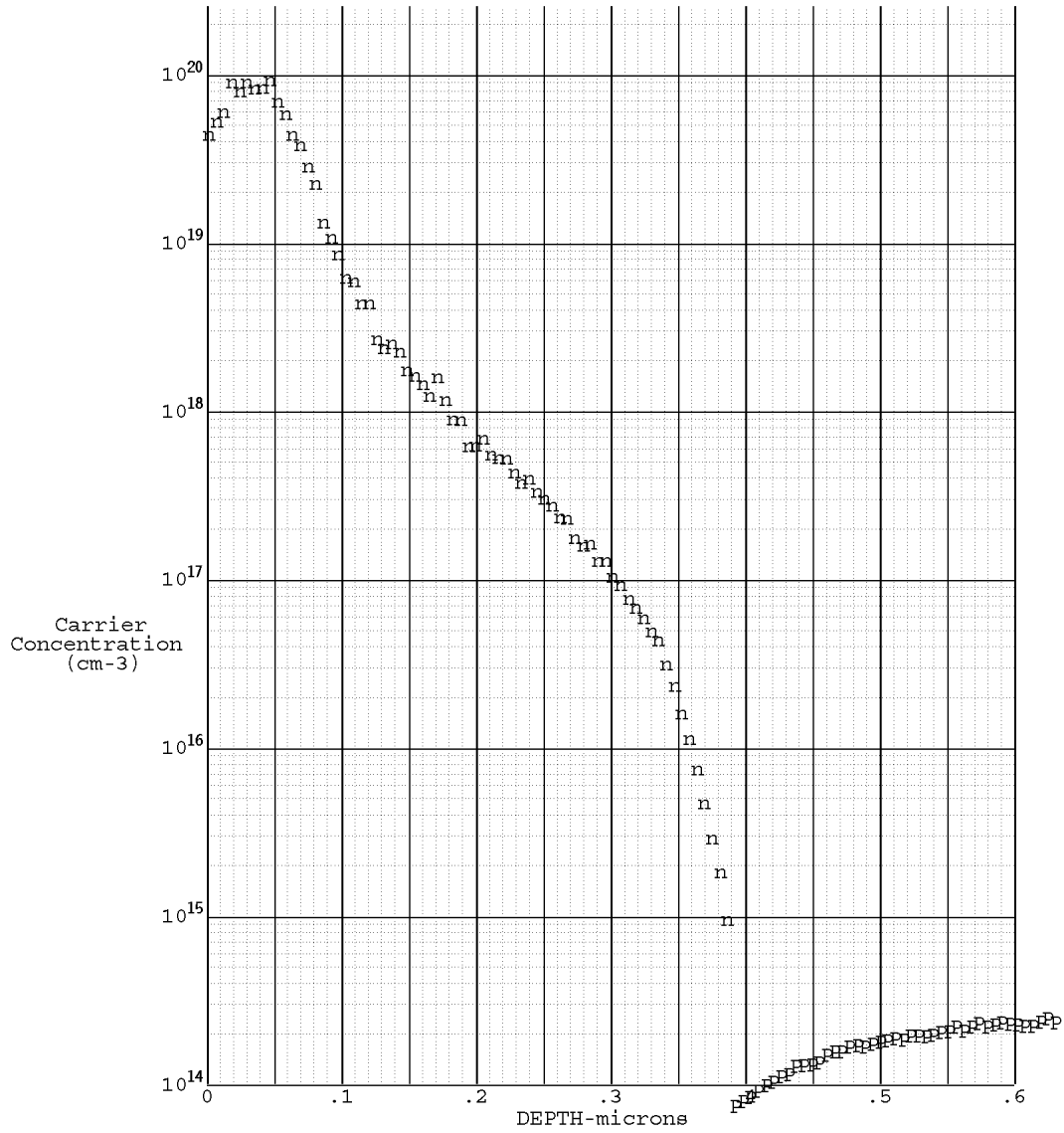
Appendix D Spreading Resistance Data




| | | | | | |
|--------------|------------|-------------|-----------|-------------|--------------------------------|
| Date | 12/08/05 | Probe Load | 2.5 grams | Orientation | <100> Si |
| File # | RNBML785 | Bevel Angle | .00319 | Step Increm | 2 um |
| Source | RIT | | | Sample # | P32 A |
| Job # | 511128 | | | 1-N Dose= | 2.3E+13 cm-2 Sheet= 1 Kohms/sq |
| Profile by | Martins | | | | |
| 4-pp sheet = | 1 Kohms/sq | | | | |

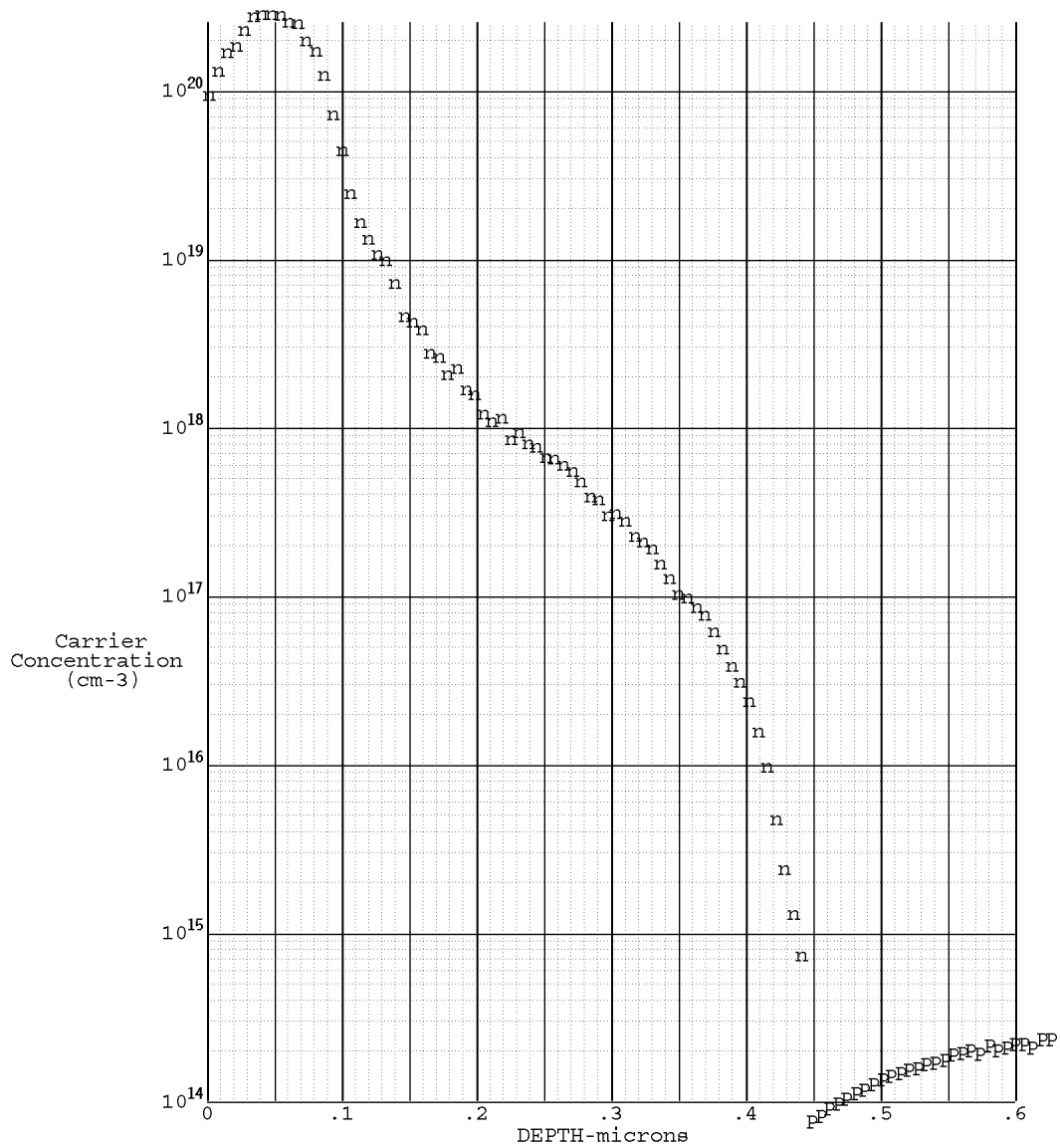



770 Trademark Drive Reno, NV 89521-5926 (775) 853-5900 www.solecon.com



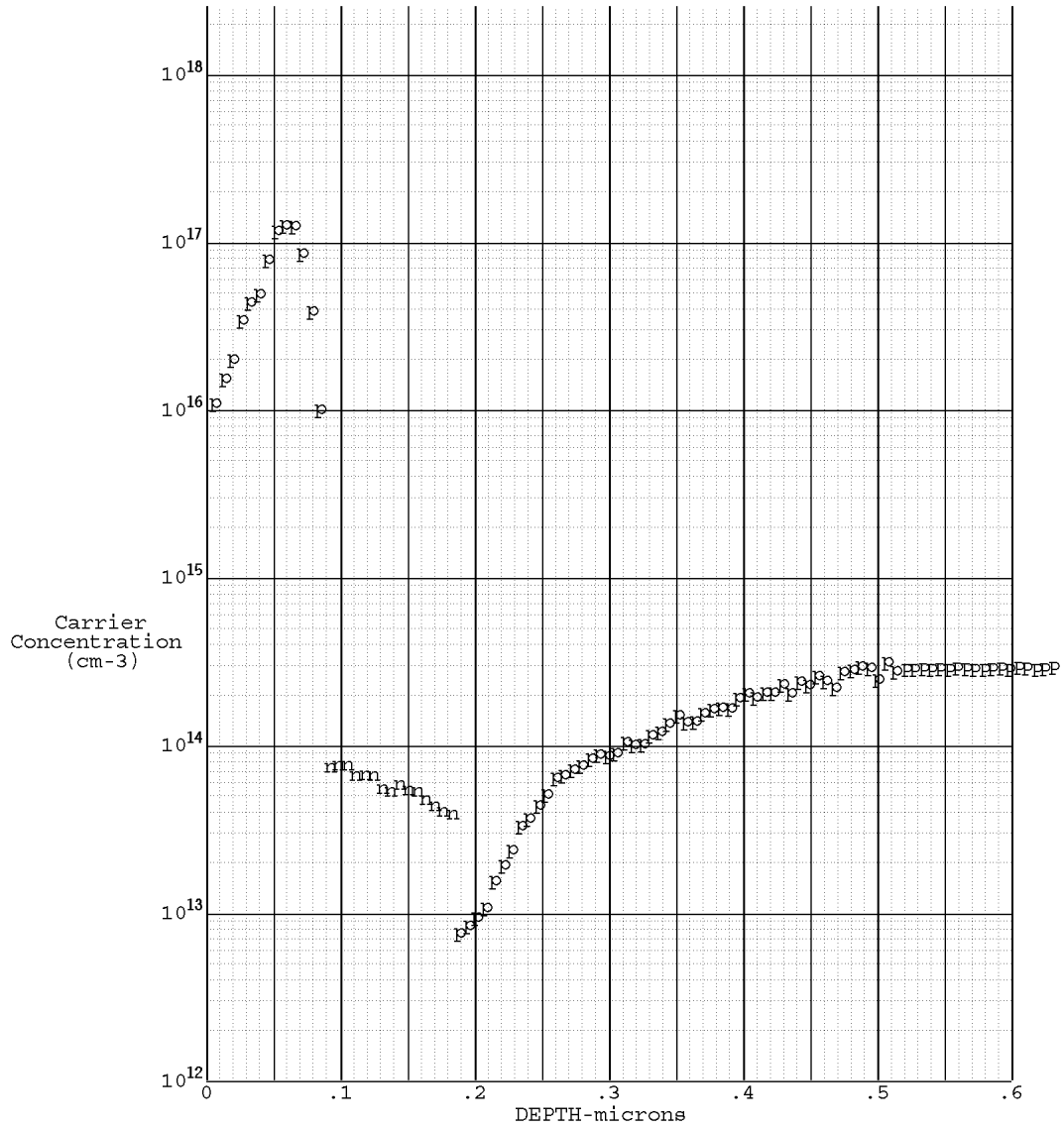
| | | | | | |
|--------------|---------------|--|-----------|-------------|---------------------------------|
| Date | 12/08/05 | Probe Load | 2.5 grams | Orientation | <100> Si |
| File # | RNBML787 | Bevel Angle | .00283 | Step Increm | 2 um |
| Source | RIT | | | Sample # | P34 A |
| Job # | 511128 | | | 1-N Dose= | 5.8E+14 cm-2 Sheet= 120 ohms/sq |
| Profile by | Martins |  | | | |
| 4-pp sheet = | 131.8 ohms/sq | | | | |

770 Trademark Drive Reno, NV 89521-5926 (775) 853-5900 www.solecon.com



| | | | | | |
|--------------|------------|--|-----------|-------------|--------------------------------|
| Date | 12/08/05 | Probe Load | 2.5 grams | Orientation | <100> Si |
| File # | RNBML789 | Bevel Angle | .00329 | Step Increm | 2 um |
| Source | RIT | | | Sample # | P36 A |
| Job # | 511128 | | | 1-N Dose= | 2.2E+15 cm-2 Sheet= 38 ohms/sq |
| Profile by | Martins |  | | | |
| 4-pp sheet = | 57 ohms/sq | | | | |

770 Trademark Drive Reno, NV 89521-5926 (775) 853-5900 www.solecon.com

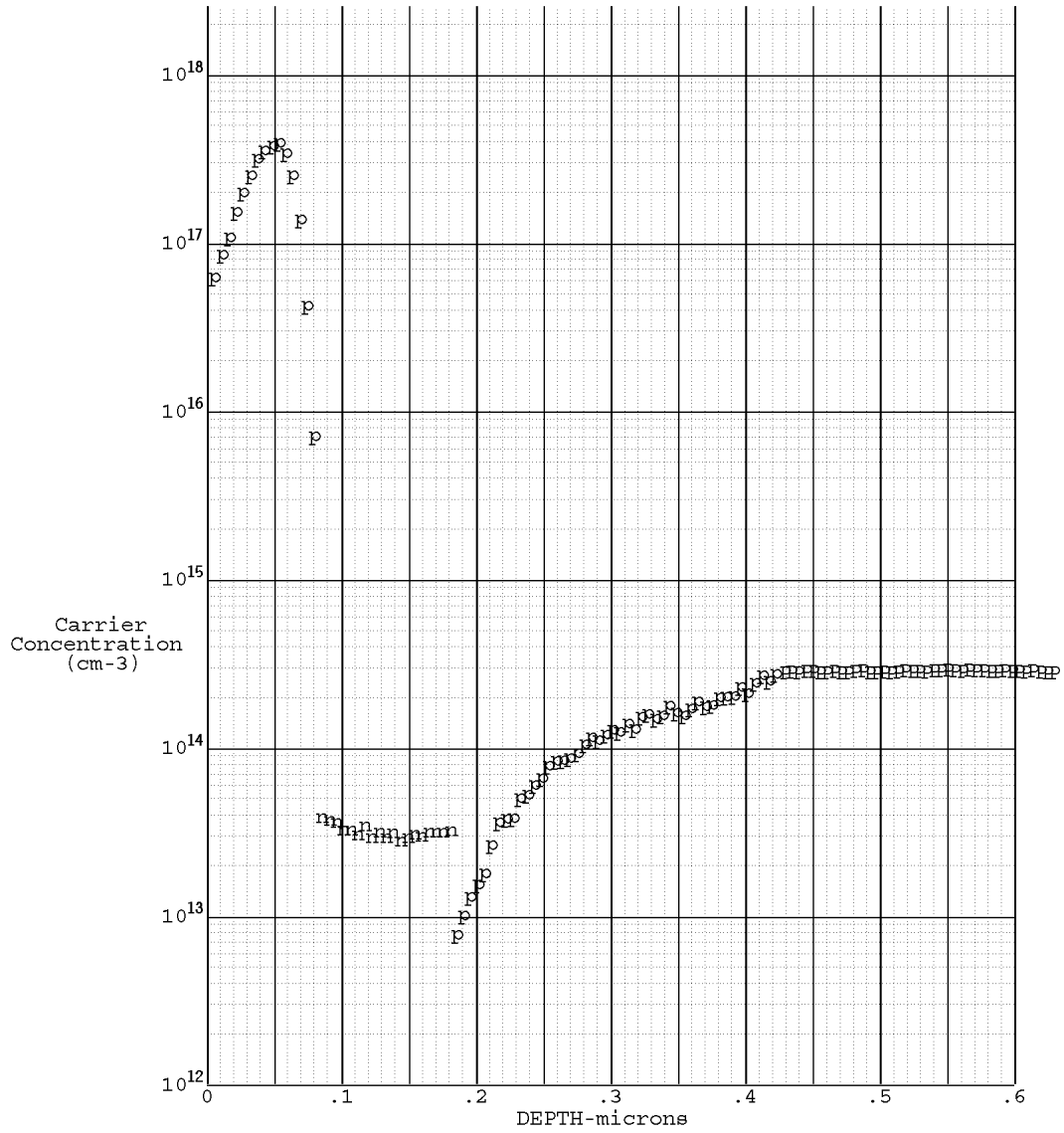


| | | | | | |
|--------------|---------------|-------------|-----------|-------------|----------------------------------|
| Date | 12/08/05 | Probe Load | 2.5 grams | Orientation | <100> Si |
| File # | RNBML791 | Bevel Angle | .00325 | Step Incom | 2 um |
| Source | RIT | | | Sample # | #P38 A |
| Job # | 511128 | | | 1-P Dose= | 5E+11 cm-2 Sheet= 37 Kohms/sq |
| Profile by | Martins | | | 2-N Dose= | 5.8E+08 cm-2 Sheet= 7500 Kohms/s |
| 4-pp sheet = | 30.4 Kohms/sq | | | | |



770 Trademark Drive Reno, NV 89521-5926 (775) 853-5900 www.solecon.com

9

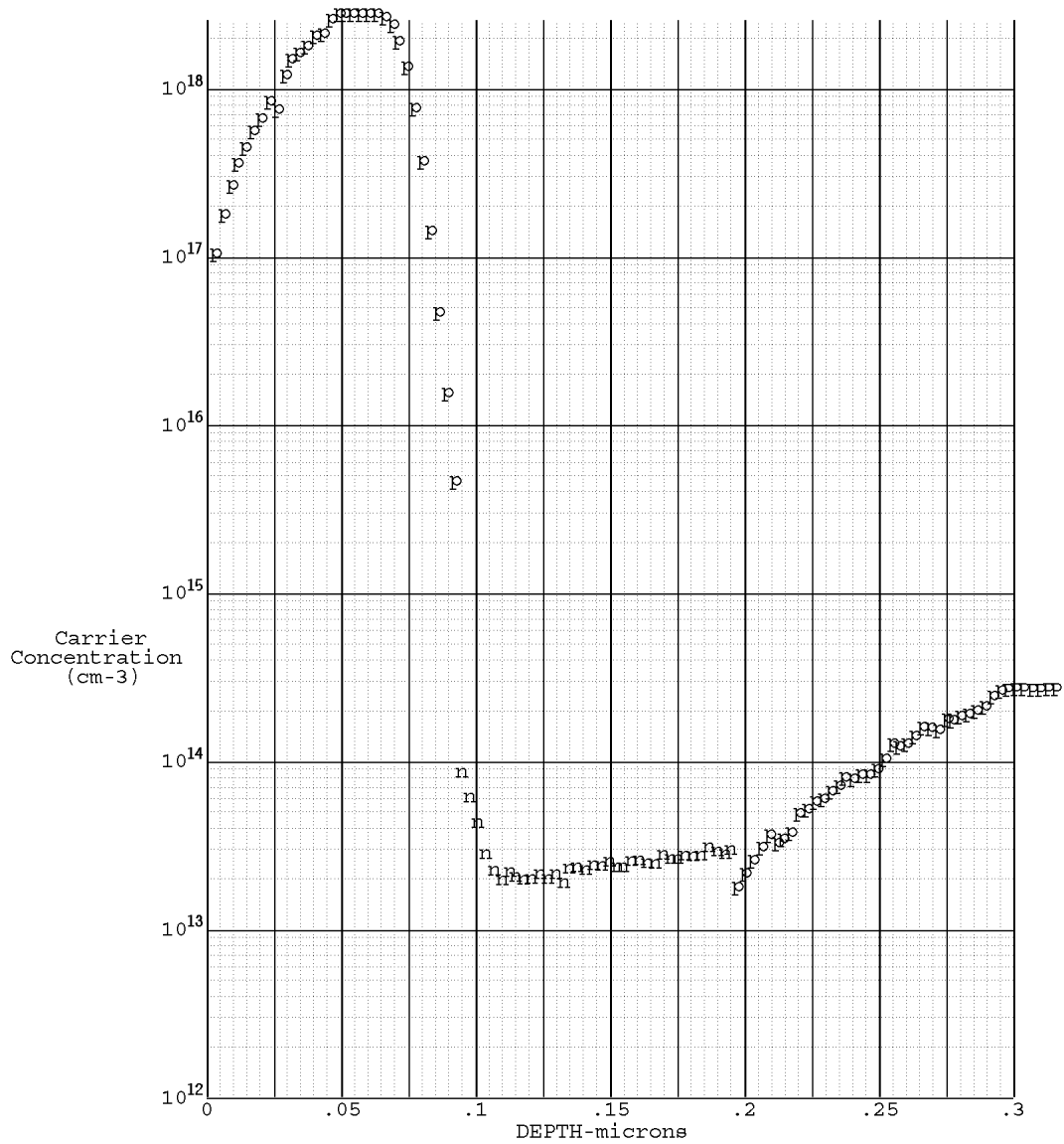


| | | | | | |
|------------|----------|-------------|-----------|-------------|----------------------------------|
| Date | 12/08/05 | Probe Load | 2.5 grams | Orientation | <100> Si |
| File # | RNEM1793 | Bevel Angle | .00264 | Step Increm | 2 um |
| Source | RIT | | | Sample # | P39 A |
| Job # | 511128 | | | 1-P Dose= | 1.7E+12 cm-2 Sheet= 15 Kohms/sq |
| Profile by | Martins | | | 2-N Dose= | 3.3E+08 cm-2 Sheet= 13000 Kohms/ |

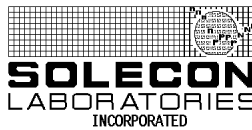


770 Trademark Drive Reno, NV 89521-5926 (775) 853-5900 www.solecon.com

sq

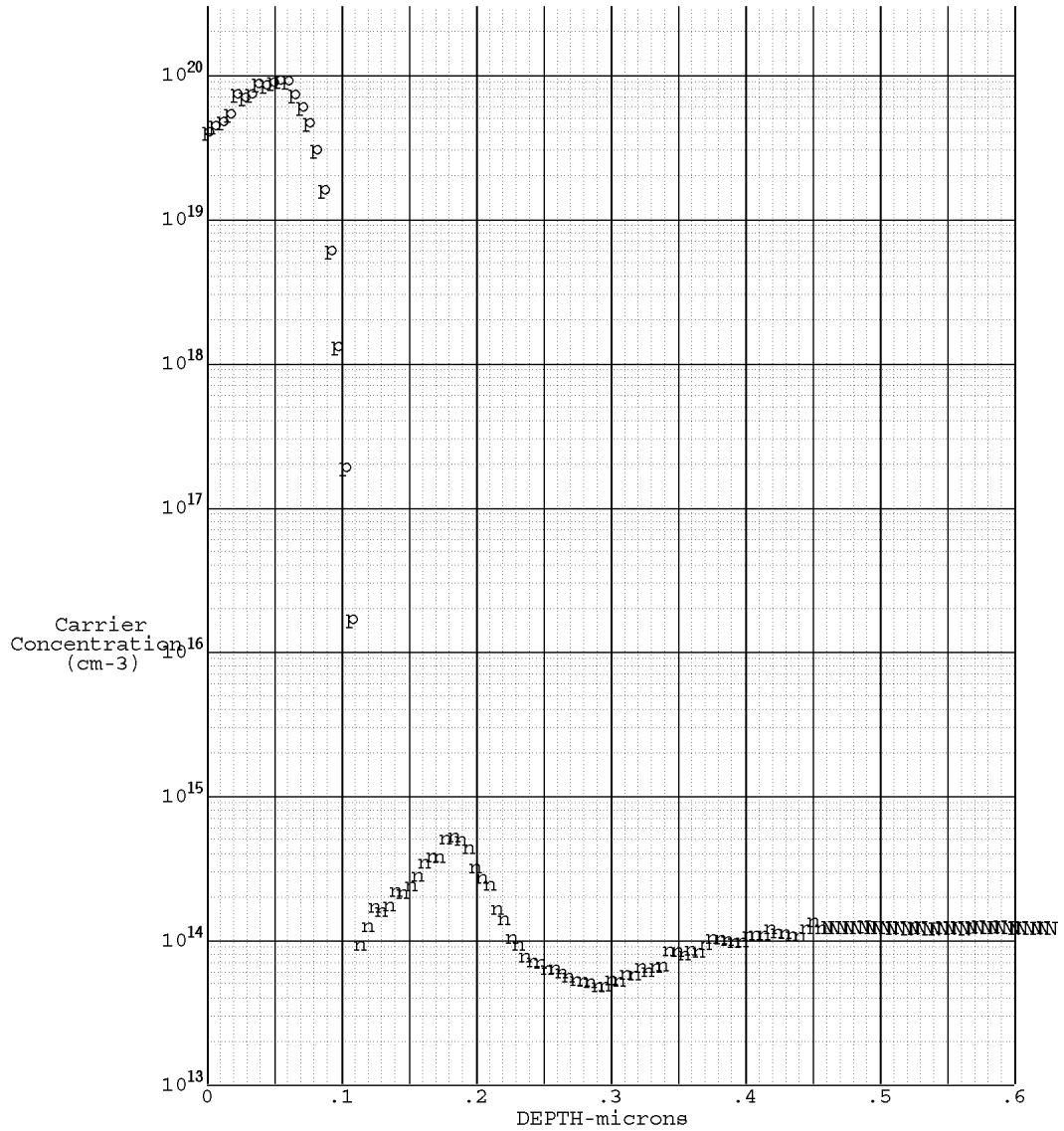


| | | | | | |
|--------------|--------------|-------------|-----------|-------------|------------------------------------|
| Date | 12/08/05 | Probe Load | 2.5 grams | Orientation | <100> Si |
| File # | RNBEM1797 | Bevel Angle | .00143 | Step Increm | 2 um |
| Source | RIT | | | Sample # | P40 A |
| Job # | 511128 | | | 1-P Dose= | 1.3E+13 cm-2 Sheet= 3.6 Kohms/sq |
| Profile by | Martins | | | 2-N Dose= | 2.9E+08 cm-2 Sheet= 15000 Kohms/sq |
| 4-pp sheet = | 3.2 Kohms/sq | | | | |

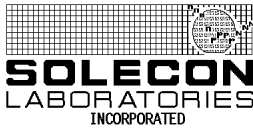


770 Trademark Drive Reno, NV 89521-5926 (775) 853-5900 www.solecon.com

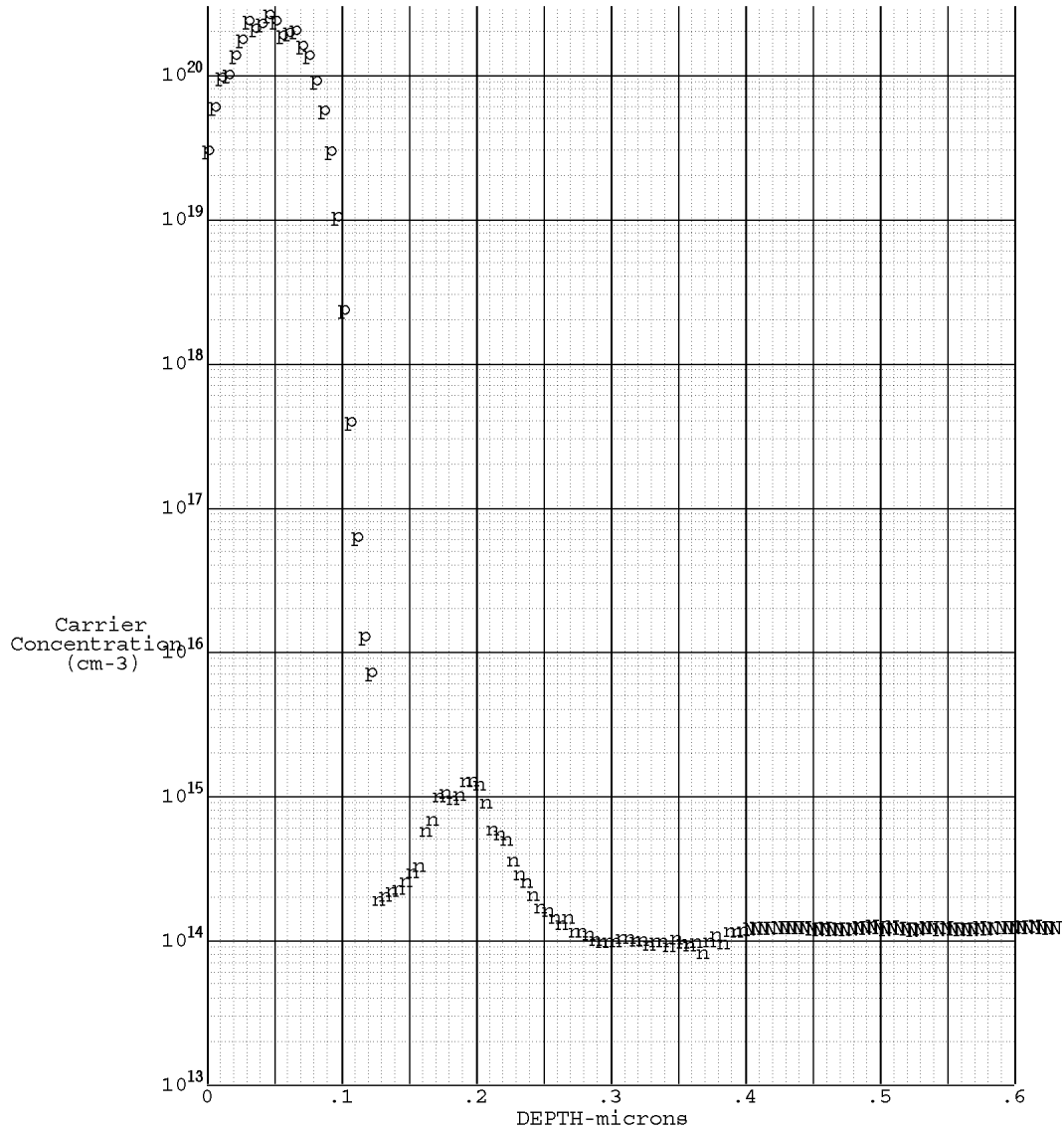
sq



| | | | | | |
|--------------|---------------|-------------|-----------|-------------|---------------------------------|
| Date | 12/08/05 | Probe Load | 2.5 grams | Orientation | <100> Si |
| File # | RNB0001 | Bevel Angle | .00267 | Step Increm | 2 um |
| Source | RIT | | | Sample # | #58 A |
| Job # | 511128 | | | 1-P Dose= | 5.9E+14 cm-2 Sheet= 190 ohms/sq |
| Profile by | Martins | | | 2-N Dose= | 5.2E+09 cm-2 |
| 4-pp sheet = | 176.5 ohms/sq | | | | |



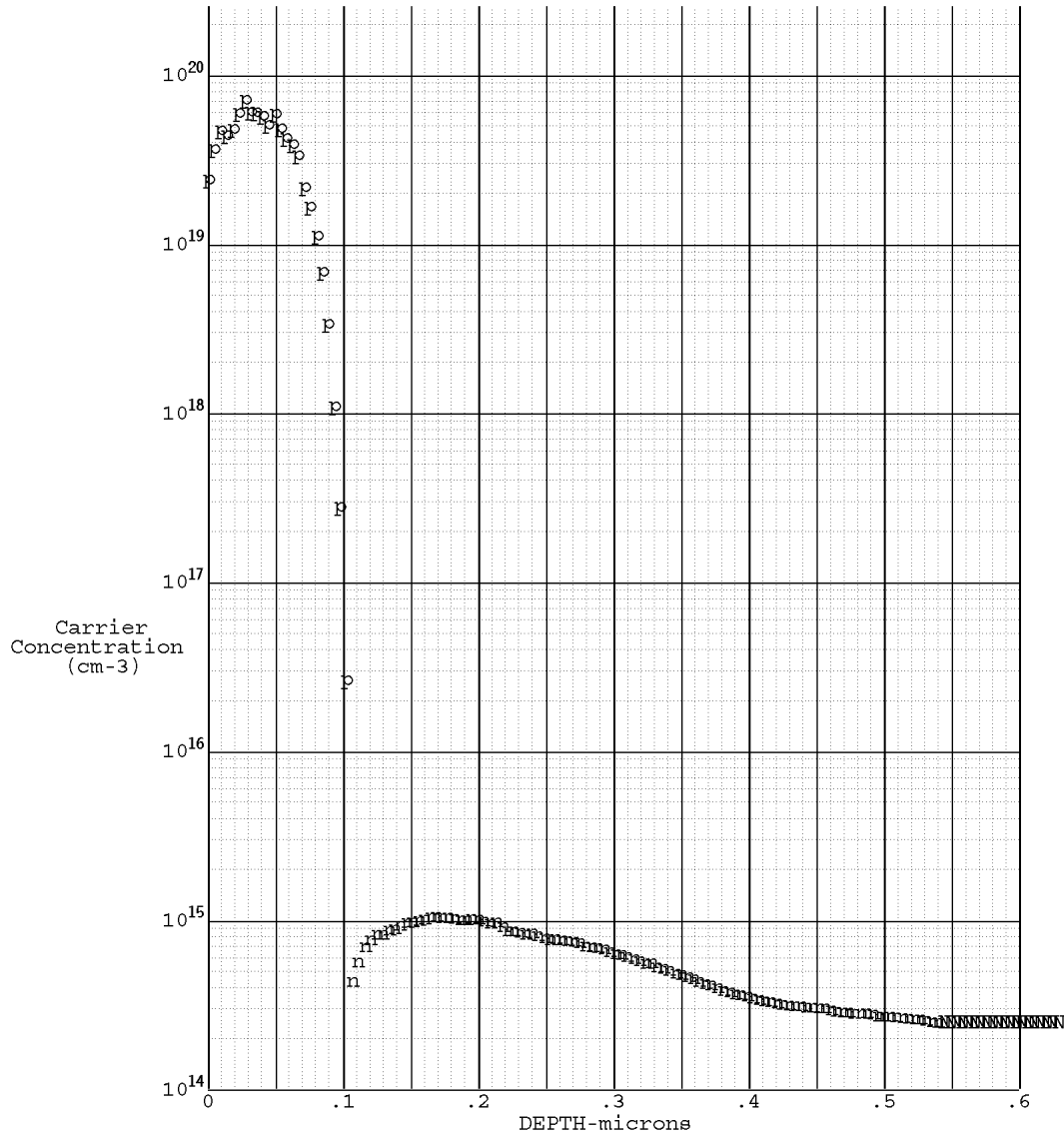
770 Trademark Drive Reno, NV 89521-5926 (775) 853-5900 www.solecon.com



| | | | | | |
|--------------|--------------|-------------|-----------|-------------|--------------------------------|
| Date | 12/08/05 | Probe Load | 2.5 grams | Orientation | <100> Si |
| File # | RNBNO003 | Bevel Angle | .00252 | Step Increm | 2 um |
| Source | RIT | | | Sample # | #N60 A |
| Job # | 511128 | | | 1-P Dose= | 1.5E+15 cm-2 Sheet= 78 ohms/sq |
| Profile by | Martins | | | 2-N Dose= | 8.999999E+09 cm-2 |
| 4-pp sheet = | 95.3 ohms/sq | | | | |



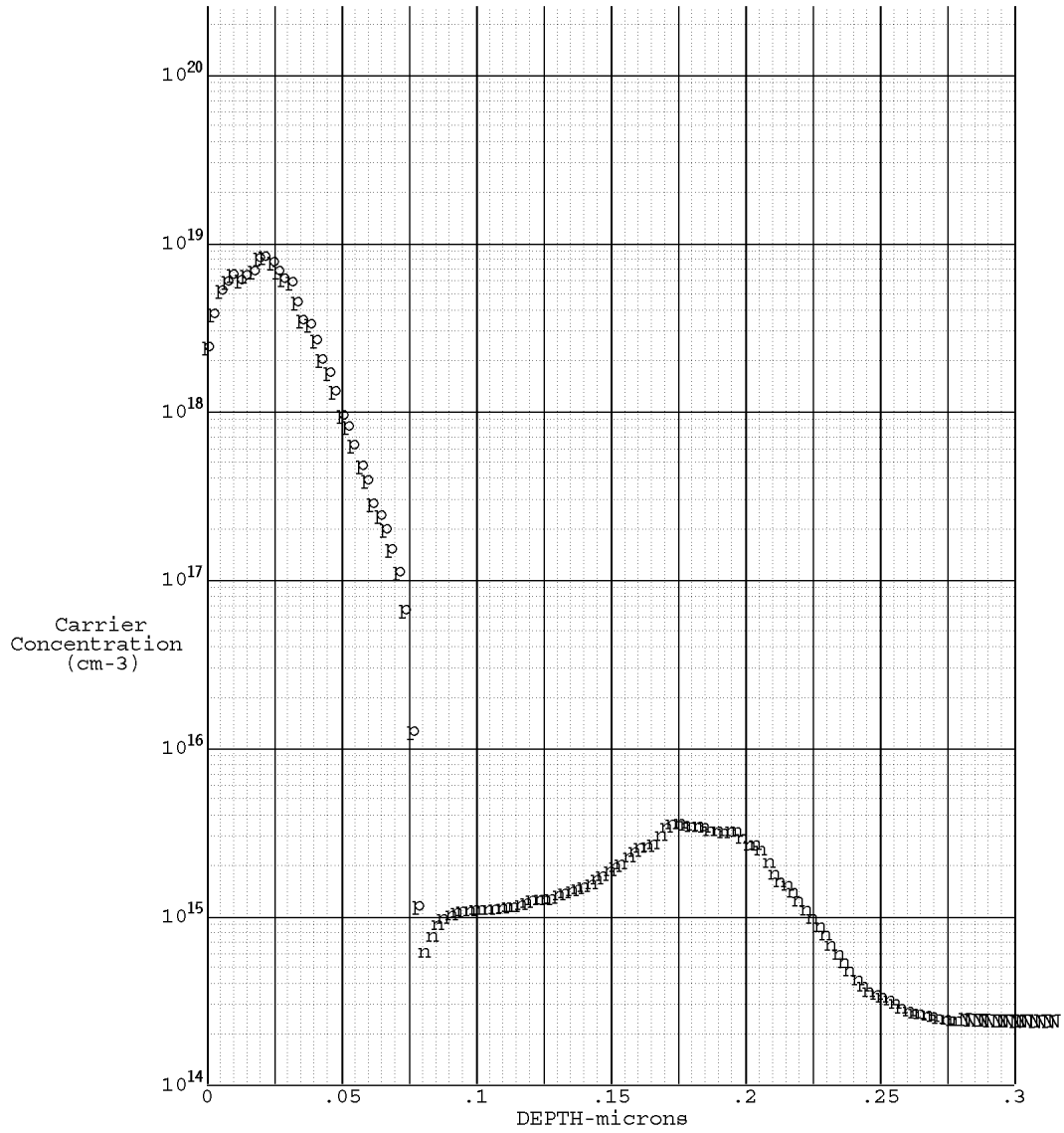
770 Trademark Drive Reno, NV 89521-5926 (775) 853-5900 www.solecon.com



| | | | | | |
|------------|----------|-------------|-----------|------------------------|--------------------|
| Date | 03/23/06 | Probe Load | 2.6 grams | Orientation | <100> Si |
| File # | RNEy0352 | Bevel Angle | .00221 | Step Increm | 2 um |
| Source | R.I.T. | | | Sample #N78 #1 | |
| Job # | 603078 | | | 1-P Dose= 3.8E+14 cm-2 | Sheet= 290 ohms/sq |
| Profile by | CHELSEA | | | 2-N Dose= 2.6E+10 cm-2 | |



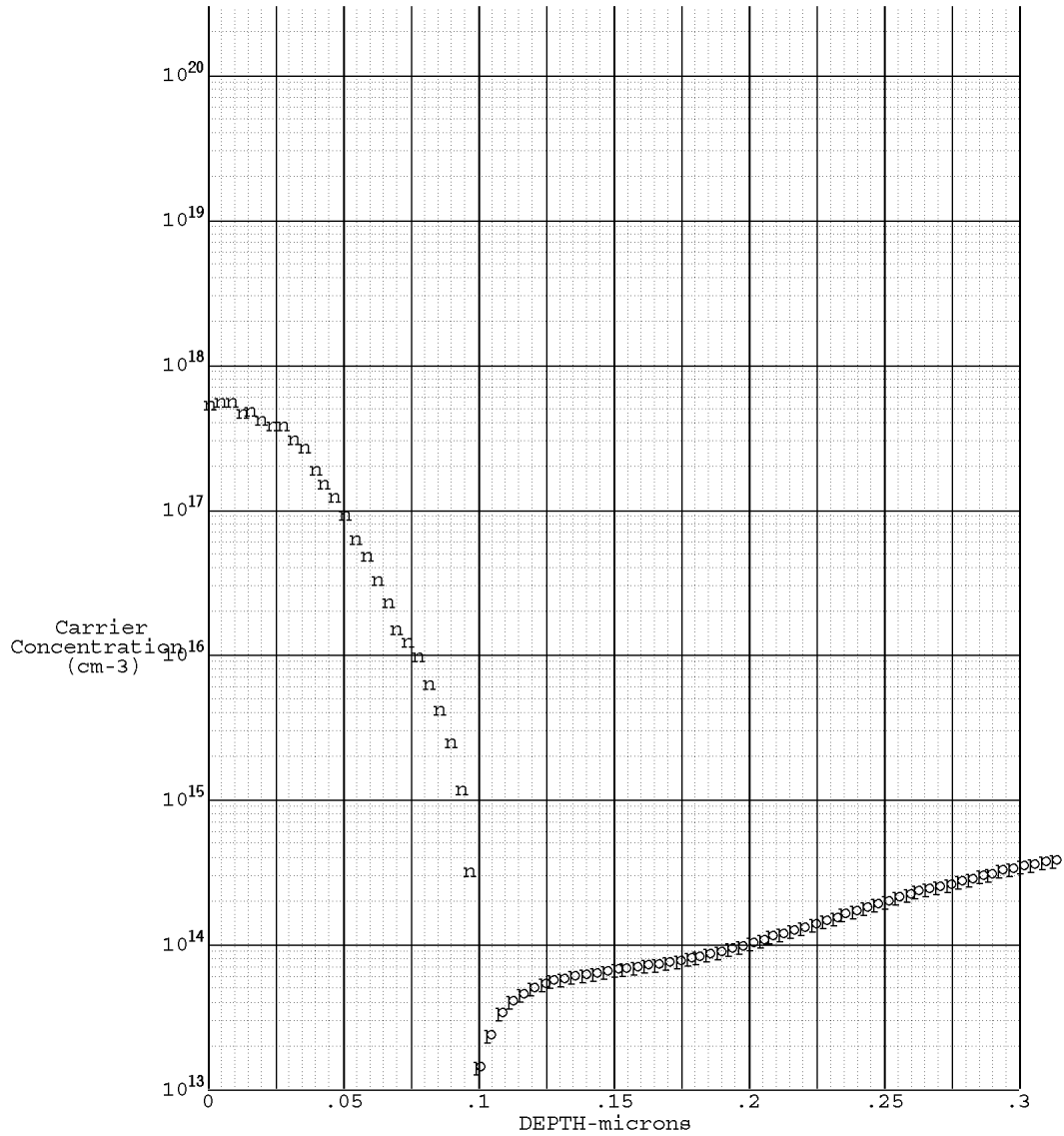
770 Trademark Drive Reno, NV 89521-5926 (775) 853-5900 www.solecon.com



| | | | | | |
|------------|----------|-------------|-----------|------------------------|---------------------|
| Date | 03/23/06 | Probe Load | 2.6 grams | Orientation | <100> Si |
| File # | RNEy0354 | Bevel Angle | .00118 | Step Increm | 2 um |
| Source | R.I.T. | | | Sample #N87 #2 | |
| Job # | 603078 | | | 1-P Dose= 2.7E+13 cm-2 | Sheet= 2.5 Kohms/sq |
| Profile by | CHELSEA | | | 2-N Dose= 3.1E+10 cm-2 | |



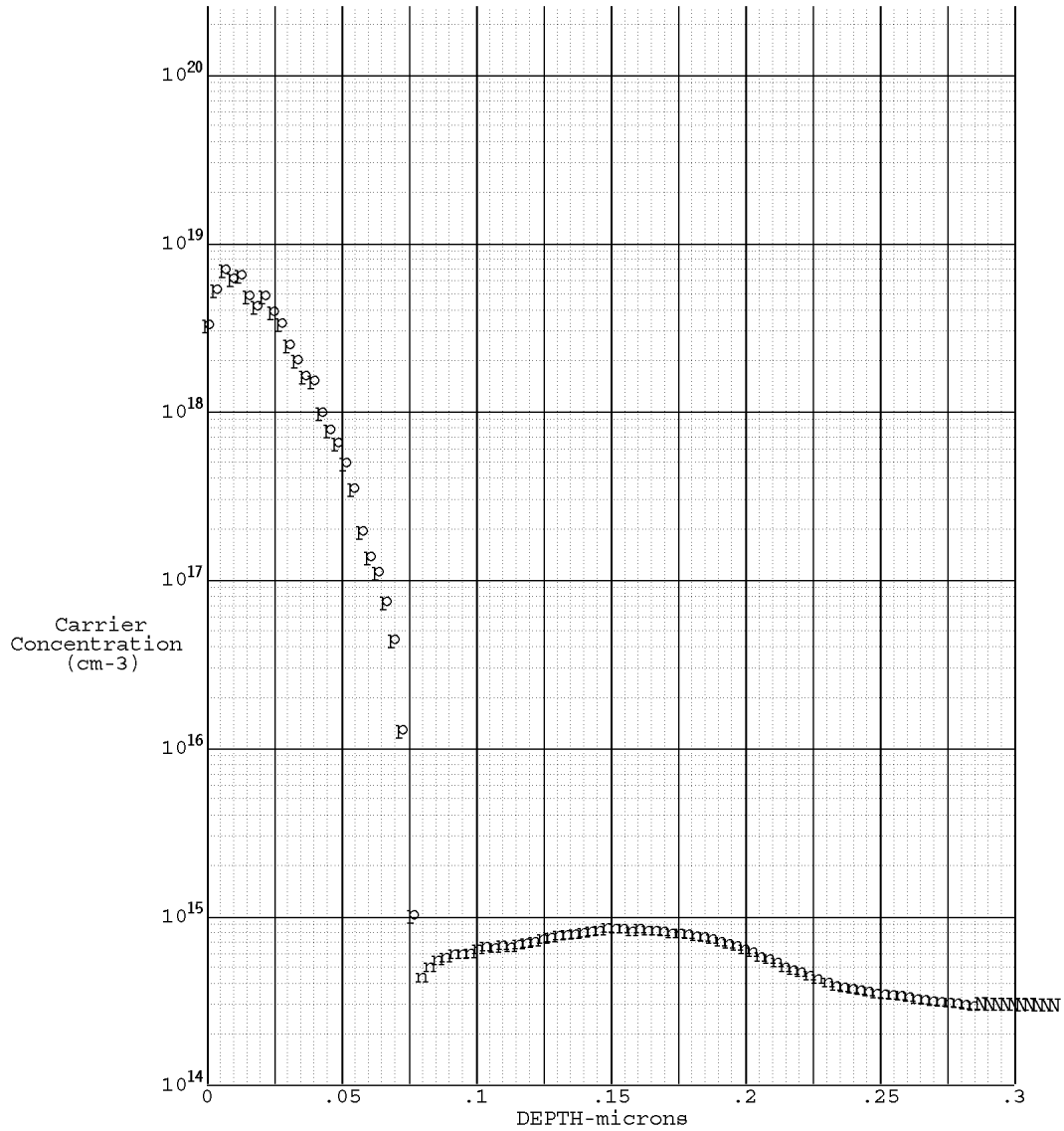
770 Trademark Drive Reno, NV 89521-5926 (775) 853-5900 www.solecon.com



| | | | | | |
|------------|----------|-------------|-----------|-------------|--------------------------------|
| Date | 03/23/06 | Probe Load | 2.6 grams | Orientation | <100> Si |
| File # | RNEy0356 | Bevel Angle | .00193 | Step Increm | 2 um |
| Source | R.I.T. | | | Sample # | SP1 #3 |
| Job # | 603078 | | | 1-N Dose= | 2E+12 cm-2 Sheet= 6.8 Kohms/sq |
| Profile by | CHELSEA | | | | |



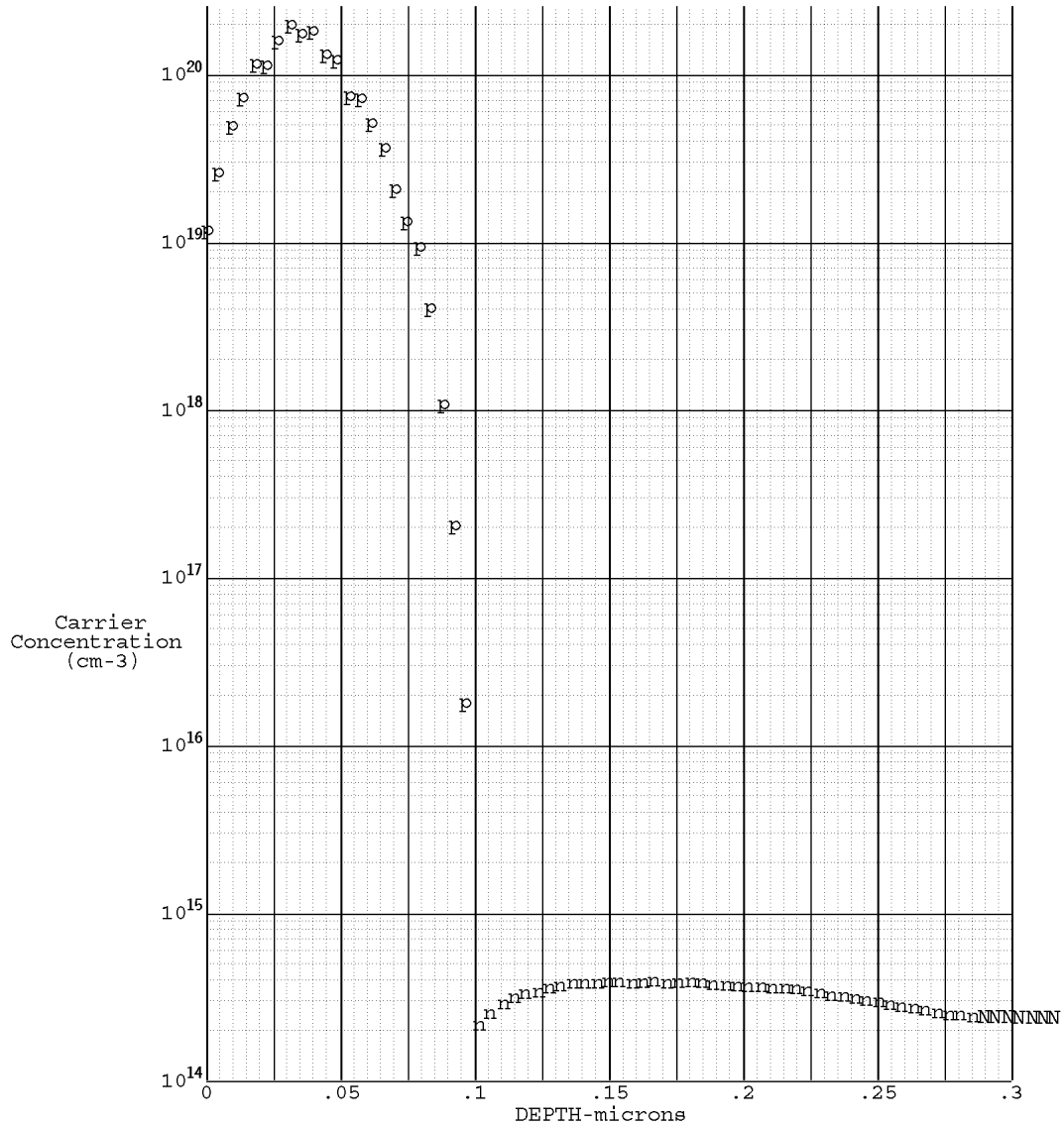
770 Trademark Drive Reno, NV 89521-5926 (775) 853-5900 www.solecon.com



| | | | | | |
|------------|----------|-------------|-----------|-------------|--------------|
| Date | 03/23/06 | Probe Load | 2.6 grams | Orientation | <100> Si |
| File # | RNEy0358 | Bevel Angle | .00151 | Step Increm | 2 um |
| Source | R.I.T. | | | Sample # | SN1 #4 |
| Job # | 603078 | | | 1-P Dose= | 1.9E+13 cm-2 |
| Profile by | CHELSEA | | | 2-N Dose= | 1.3E+10 cm-2 |



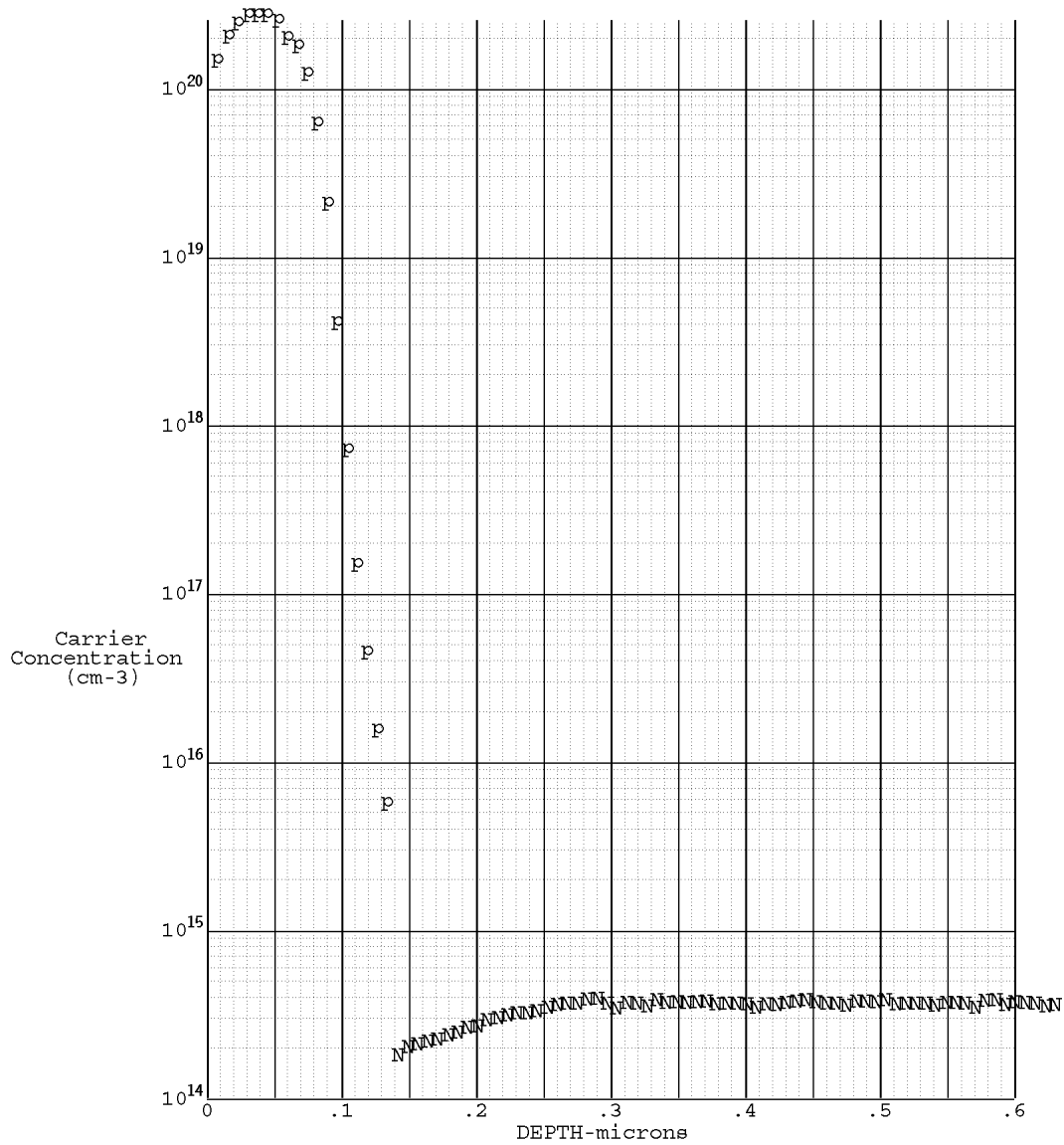
770 Trademark Drive Reno, NV 89521-5926 (775) 853-5900 www.solecon.com



| | | | | | |
|------------|----------|-------------|-----------|-------------|---------------------------------|
| Date | 03/23/06 | Probe Load | 2.6 grams | Orientation | <100> Si |
| File # | RNEy0360 | Bevel Angle | .00219 | Step Increm | 2 um |
| Source | R.I.T. | | | Sample # | SN7 #5 |
| Job # | 603078 | | | 1-P Dose= | 7.4E+14 cm-2 Sheet= 150 ohms/sq |
| Profile by | CHELSEA | | | 2-N Dose= | 6.4E+09 cm-2 |



770 Trademark Drive Reno, NV 89521-5926 (775) 853-5900 www.solecon.com



| | | | | | |
|--------------|--------------|-------------|-----------|-------------|--------------------------------|
| Date | 03/01/06 | Probe Load | 2.5 grams | Orientation | <100> Si |
| File # | RNB0919 | Bevel Angle | .0037 | Step Increm | 2 um |
| Source | R.I.T. | | | Sample # | SN8 #6 |
| Job # | 602106 | | | 1-P Dose= | 1.9E+15 cm-2 Sheet= 62 ohms/sq |
| Profile by | CHELSEA | | | | |
| 4-pp sheet = | 91.5 ohms/sq | | | | |



770 Trademark Drive Reno, NV 89521-5926 (775) 853-5900 www.solecon.com

Appendix E Model Equations

Mobility Equations [11]:

$$\mu_n = \mu_0 + \frac{(\mu_{\max} - \mu_0)}{\left[1 + \left(\frac{n}{C_r}\right)^a\right]} \frac{\mu_1}{\left[1 + \left(\frac{C_s}{n}\right)^b\right]}$$

$$\mu_p = \mu_0 e^{-p_c/p} + \frac{\mu_{\max}}{\left[1 + \left(\frac{p}{C_r}\right)^a\right]} \frac{\mu_1}{\left[1 + \left(\frac{C_s}{p}\right)^b\right]}$$

Table E-1

Fitting parameters for mobility equations [11]

| Parameter | Arsenic | Phosphorus | Boron |
|-------------------------------------|-----------------------|-----------------------|-----------------------|
| μ_0 (cm ² /V s) | 52.2 | 68.5 | 44.9 |
| μ_{\max} (cm ² /V s) | 1417 | 1414 | 470.5 |
| μ_1 (cm ² /V s) | 43.4 | 56.1 | 29.0 |
| C_r (cm ⁻³) | 9.68x10 ¹⁶ | 9.20x10 ¹⁶ | 2.23x10 ¹⁷ |
| C_s (cm ⁻³) | 3.43x10 ²⁰ | 3.41x10 ²⁰ | 6.10x10 ²⁰ |
| a | 0.680 | 0.711 | 0.719 |
| b | 2.00 | 1.98 | 2.00 |
| p_c (cm ⁻³) | - | - | 9.23x10 ¹⁶ |

SUPREM Implant Model Equations [25]:

Single Pearson IV model:

$$f(x) = K \left[b_0 + b_1(x - R_p) + b_2(x - R_p)^2 \right]^{\frac{1}{2b_2}} \exp \left[-\frac{\frac{b_1}{b_2} + 2a}{\sqrt{4b_1b_2 - b_1^2}} \operatorname{atan} \left(\frac{2b_2(x - R_p) + b_1}{\sqrt{4b_1b_2 - b_1^2}} \right) \right]$$

where:

$$a = \frac{\Delta R_p \gamma (\beta + 3)}{A}$$

$$K = \int_{-\infty}^{\infty} f(x) dx = 1 \quad b_0 = \frac{\Delta R_p^2 (4\beta - 3\gamma^2)}{A} \quad b_2 = \frac{2\beta - \gamma^2 - 6}{A}$$

$$b_1 = a$$

$$A = 10\beta - 12\gamma^2 - 18, \gamma$$

$$R_p = \mu_1 \quad \Delta R_p = \sqrt{\mu_2} \quad \gamma = \frac{\mu_3}{R_p^3} \quad \beta = \frac{\mu_4}{R_p^4} \quad \mu_1 = \int_{-\infty}^{\infty} xf(x)dx$$

$$\mu_i = \int_{-\infty}^{\infty} (x - R_p)^i f(x) dx \quad i = 2, 3, 4$$

$$\beta = \frac{39\gamma^2 + 48 + 6(\gamma^2 + 4)^{3/2}}{32 - \gamma^2} \quad \text{and} \quad 0 < \gamma^2 < 32$$

The Dual Pearson IV model uses a weighted average of two Single Pearson models as shown here:

$$C(x) = \phi[\mathfrak{R}f_1(x) + (1 - \mathfrak{R})f_2(x)]$$

where $\phi = \phi_1 + \phi_2$ is the total implantation dose and $\mathfrak{R} = \phi_1/\phi$.